Ultrafast Dynamics of Barrier Crossing : Step-wise Solvation Effect on Isomerization of *trans*-Stilbene in Alkane Clusters

Thesis by

Sing Hwa Chong

In Partial Fulfillment of the Requirements for the Degree of Doctor of Philosophy

California Institute of Technology

Pasadena, California

2001

(Defended August 09, 1999)

To my wife Ee Ching,

who has always put my interests before hers.

Acknowledgments

It has been a wonderful experience being a graduate student at Caltech for the past six years. I am very fortunate to have witnessed some great scientific achievements first hand, and to have interacted with many extremely talented scientists on a personal level. I am also very grateful to have been given the opportunity to be part of the Zewail group, in which not only was I taught a great deal about science, but was frequently assisted, encouraged and cheered during the "darkest evenings" of my graduate life — many of which were bitter to endure, but I am sure will be sweet to remember.

Many people deserve to be acknowledged for carrying me through my graduate studies, and I would like to take this opportunity to express my appreciation. First and foremost, I wish to thank my research advisor Prof. Ahmed Zewail, for his support, his encouragement, his scientific input, and above all, his willingness to allow me to take all the time I needed to understand and solve the problems at hand. The passion Prof. Zewail has for science is unparalleled, and the drive and hard work ethic he exhibits are both inspiring and admirable. Leading by example, he sets a very high standard of scientific professionalism for his students and postdocs to emulate. Among many things I will remember about Prof. Zewail is the advice he gave his group members on a Thanksgiving gathering a few years ago: "you don't work for your advisor, you work for yourself." These words shall resonate within me for many years to come, and they are worth passing on to my own graduate students in the future.

Many other members of the Zewail group also deserve special recognition for making "the top secret labs at the basement of the basement" (a layman description of Femtolands by a news reporter) such an exciting place to work. I wish to express my gratitude in particular to Spencer Baskin, who has been a good friend and a great teacher of mine for the past four years. Without his insightful critique, and without his insistence on science being done in finest detail and of highest quality, some of the crucial information may never have been extracted from the mound of experimental data collected. Dr. Baskin is not only among the brightest persons I know, but also possesses the utmost integrity. The countless hours we spent discussing and arguing science, politics, economics and poetry will be genuinely missed.

I would like to extend my appreciation to Ahmed Heikal, for showing me the nuts and bolts of the picosecond laser systems and the molecular beam chambers, and for interaction in and out of the lab. Also, I am thankful to Osama Abou-Zied for being accommodating during the brief period we spent together on experiments. Dongping Zhong and Hyotcherl Ihee merit special thanks for lending their ears during my ups and downs. As for the rest of the Femtolands crew, past and present, with whom I have had close contact: Chaozhi Wan, Juen-Kai Wang, Po-Yuan Cheng, Jim Cao, Mirianas Chachisvilis, Torsten Fiebig, Qianli Liu, Eric Diau, Søren Pederson and Chuck Williamson, it has been my pleasure to know them and I wish them the best of luck. Since it is impractical to make an exhaustive list, to those colleagues and friends whose name are not mentioned here, be assured that your support and help were greatly appreciated.

Many Caltech staff members were instrumental in the successful operation of my laboratory, especially Tom Dunn from the Chemistry Electronic Shop, and Guy Duremberg from the Chemistry Instrument Shop. Tom has visited Femtoland II so frequently to help me fix broken down equipment that he has almost become a lab partner. I wish to thank him for his assistance and generosity.

Finally, I could not have made it this far in my academic career without the support and love of my family. I wish to express my deepest gratitude to my parents, who worked so hard their entire lives to make sure their four children could receive first rate educations in a developed country. As for my wife, words do not suffice to describe the deep and profound love she has given me. She has been the inspiration and guiding light in my life since fate brought us together almost a decade ago.

Last but not least, I would like to thank the late Dr. Isaac Asimov, without whose writings to stir my curious young mind, my journey into the universe of science would never have begun.

Financial support for this research was provided by National Science Foundation and Air Force Office of Scientific Research.

Abstract

The ultrafast spectroscopic study of molecular clusters in supersonic beams can provide valuable information on the structure, energetics and dynamics of molecular aggregates in gas phase and in solution. This information will shed light on important issues such as how molecules interact, how energy flows in solvated systems, and how chemical reactions progress.

Although microscopic friction and solvation in barrier crossing reactions is of fundamental importance in molecular dynamics, their roles are not well understood. This is mainly due to the fact that few comprehensive investigations of this subject have been performed. In this thesis, the detail studies of a prototypical barrier crossing reaction — the photoisomerization of jet-cooled *trans*-stilbene — in size-selected *n*-alkane clusters, using the picosecond pump-probe ionization TOF mass spectrometry and transient technique, are reported. The microcanonical nonradiative decay rate constants at the S_1 manifold for *trans*-stilbene-hexane$_n$ and *trans*-stilbene-octane$_n$ (n = 1, 2) complexes, including certain deuterated variants, were measured as a function of excitation energy, with the energy range defined by tuning the pump wavelength from the 0-0 transition of *trans*-stilbene to ~ 3200 cm^{-1} higher in energy. The experimental results were modeled with standard RRKM theory, nonadiabatic RRKM theory and Kramers-type theory for microcanonical systems. It was found that the excess energy dependence results could be accounted for very well by the nonadiabatic RRKM theory, from which analysis the barriers to isomerization for all of the *trans*-stilbene *n*-alkane clusters were found to be

lower than that of the parent molecule by ~ 50%. The analysis revealed that not only can the differences in the rates among the four *trans*-stilbene-hexane$_1$ isotopic species studied (combinations of *trans*-stilbene-h_{12} and -d_{12} with *n*-hexane-h_{14} and -d_{14}) be attributed to *energy friction*, a term describing how energy is "drained away" from the reaction coordinate as a result of the change in the vibrational density of states, but the reduction in the nonradiative rates of the 1:2 complexes, relative to that of the 1:1 complexes, can also be attributed to the same *energy friction*.

Finally, in the same studies, the cluster binding energies of *trans*-stilbene-hexane$_n$ and *trans*-stilbene-octane$_n$ were also determined.

Table of Contents

Acknowledgments.....iv

Abstract.....vii

Table of Contents.....ix

Chapter 1. Introduction.....1

1.1. References.....7

1.2. Figure Captions.....9

Chapter 2. Experimental Methodology.....11

2.1. Picosecond Laser Systems.....12

2.2. Molecular Beam Apparatus.....13

2.3. Data Acquisition.....15

2.4. Sample Handling.....16

2.5. Calculation of Vibrational Frequencies.....18

2.6. References.....19

2.7. Figure Captions.....20

Chapter 3. Results.....23

3.1. Mass Spectra and Transients.....24

3.2. Excess Energy Dependent Studies.....26

3.3. References.....30

3.4. Figure Captions.....31

Chapter 4. Discussion.....62

4.1. Preliminaries.....63

4.2. Kinetic Scheme.....64

4.3. Isomerization vs. Evaporation.....74

4.4. Isomerization Rates: Experiment vs. Theory.....81

4.5. References.....93

4.6. Figure Captions.....95

Chapter 5. Conclusions.....113

5.1. References.....117

Appendix I.....118

Appendix II.....133

Appendix III.....136

AIII.1. Figure Captions.....139

Chapter 1

Introduction

The photoisomerization of *trans*-stilbene (tS) has generated wide theoretical and experimental interests for well over three decades (for reviews, see Refs. 1 and 2). Aside from being used extensively as a testing ground for Kramers-type models [3-7], this prototypical barrier crossing reaction has also served to examine the applicability of various modified RRKM theories (in the gas phase) [8-15]. Due to the fact that intramolecular vibrational energy redistribution (IVR) is dissipative and complete above the isomerization barrier [8], statistical theories can be applied to model the reaction rates. Since reporting the first experimental result on jet-cooled tS [16], this group has investigated a range of issues related to tS isomerization dynamics. This includes the nature of the transition state [17], the adiabaticity of the reaction [9], the nature of IVR in the isolated molecule [8] and in clusters [18,19], and the effect of microscopic friction on the reaction [20]. Independently, various research groups have also pursued similar objectives [1,2]. However, despite extensive studies, many questions remain unanswered regarding the dynamics of the tS photoisomerization reaction, in particular, the effect of solvent friction on the microcanonical and canonical rates, and on activation barrier crossing. One of the most intriguing outcomes in the study of tS photoisomerization is the observation that the thermal rate measured in low viscosity liquids [4,6] is much higher than the canonical rate, $k(T)$, predicted from the isolated molecule microcanonical rate, $k(E)$, obtained from measurement of isolated molecules in supersonic beam [8,10,16,23].

Numerous attempts were made to reconcile the differences in the calculated and the observed thermal rates in low viscosity liquids. Two widely discussed statistical

approaches were proposed, one developed by Troe [12] and the other by Felker and Zewail [9]. Troe assumed the isomerization reaction to be adiabatic and utilized a method of scaling certain transition-state frequencies. In the Felker and Zewail model, nonadiabatic effects — a natural consequence if the isomerization barrier is formed by avoided crossing between two potentials (as supported by most theoretical calculations [24-26]) — were taken into account. In order to avoid biases in vibrational frequency selection, Negri and Orlandi [13] subsequently reexamined the above modified RRKM theories with only vibrational frequencies that were calculated using quantum chemical methods. Their analysis revealed that although both Troe and Felker and Zewail models could reproduce the experimental *k(E)* fairly well with their sets of frequencies, only the Felker and Zewail model could successfully explain the discrepancy between calculated *k(T)* and the measured thermal rate in low viscosity liquids. Recently, Gershinsky and Pollak [15] revisited the tS isomerization problem and were reasonably successful in predicting *k(E)* and *k(T)* in liquids with statistical calculations based on *empirical* potential energy surfaces developed by Vachev *et al.* [27]. However, in order to bridge the differences in rate observed in the low viscosity liquids and the vapor phase experiments, Gershinsky and Pollak invoked the idea of "laser cooling of the excited state" [15], wherein it was argued that the temperature of gaseous tS at the S_1 state ought to be lower than that at the S_0 state when tS was excited with a laser frequency corresponding to the 0-0 transition of tS.

In order to provide further insight into the nature of the transition state, the adiabaticity of the reaction and the microscopic interaction between solute and solvent,

we investigated the photoisomerization of tS in *n*-hexane and *n*-octane clusters in a molecular beam. An example of such a cluster — a calculated structure of tS-hexane$_3$ — is shown in Fig. 1. The preliminary results of our investigations were published earlier [20], where we reported our first study of the isomerization of isolated tS-hexane$_n$ clusters (n = 1-5) in a molecular beam. In that publication, we reported a sharp decrease in the rates measured as a function of increasing n, while one might have expected the opposite, given that isomerization rates are faster in low viscosity solutions than in the isolated molecule. A lowering of the energy threshold for isomerization in tS-hexane$_1$ was also reported. Three factors affecting microcanical rates within the context of standard RRKM theory were discussed: (1) changes in the reaction potential, (2) changes in the effective inertia for motion in the isomerization coordinate, and (3) "energy friction," whereby solvent vibrational modes and the low frequency intermolecular cluster modes inhibit vibrational energy deposited into the system from reaching the reaction coordinate by adding a large energy bath to the system.

Since the publication of our initial report, Marcus [28] and Gershinsky and Pollak [29] proposed separate models to explain the observed phenomena. In his paper, Marcus modified the standard RRKM rate equation by including Kramers-type descriptions which take into account the frictional effects arising from the motions of the solvent molecules, i.e., "motional friction" as distinct from "energy friction." A relevant outcome of his work is a rate equation which scales with the standard RRKM rate. Gershinsky and Pollak calculated RRKM rates for tS hexane clusters based on the empirical tS potentials developed by Vachev *et al.*, and hexane potentials developed by

Dillen [30]. Recently, Lienau *et al.* [31] observed multiexponential decays in fluorescence from a mixed composition of tS and tS-hexane$_1$ in supersonic expansion with the time-correlated single-photon counting technique. They interpreted their data to indicate that the isomerization barrier for the 1:1 complex was at ~ 950 cm^{-1}. However, no comparison with theory of the isomerization rate of tS-hexane$_1$ as a function of excitation energy was given.

In this thesis, new and detailed experimental results for tS-hexane$_n$ and tS-octane$_n$ (n = 1, 2), and a number of deuterated variants are reported, and an extensive analysis of the data is given. In the earlier work [20], we mentioned our results could be influenced by ineffective cooling and vibrational predissociation (vp) of larger clusters. To remedy these problems, in all the experimental results reported here, we have chosen to allow greater gas flow while limiting the amount of larger clusters generated during measurements by carefully controlling the temperature of the solvent samples. The tS-hexane$_n$ results reported in Ref. 20 were obtained with solvent left at room temperature.

This thesis is organized as follows: In chapter 2, experimental details such as the picosecond laser systems, the molecular beam apparatus, sample handling technique, data acquisition, and method for computation of vibrational frequencies are outlined. The experimental results, including tS-*hexane*$_n$ and tS-*octane*$_n$ (n = 1, 2) results obtained under better controlled conditions, are reported in chapter 3. Previously [20], we mentioned our results could be affected by ineffective cooling and vibrational predissociation (vp) of larger clusters. To remedy these problems, in all the experimental

results reported here, we have chosen to allow greater gas flow while limiting the amount of larger clusters generated during measurements by carefully controlling the temperature of the solvent samples. The tS-*hexane*$_n$ results reported in Ref. 20 were obtained with solvent left at room temperature. In chapter 4, a kinetic scheme is developed to help us identify the ion signals originated from either direct ionization or fragmentation, so correct interpretation of the measured rates can be made. A detailed analysis of the results with various treatments, such as the Gershinsky and Pollak harmonic RRKM model, the nonadiabatic RRKM model, and the Kramers-type model follows to elucidate the nature of microscopic friction and the effects of solvation on the isomerization barrier. The conclusion of our analysis is given in chapter 5.

1.1. References

1. Waldeck, D. H. *Chem. Rev.* **1991**, *91*, 415.

2. Saltiel, J.; Sun, Y.-P. *Photochroism-Molecules and Systems*; Dürr, H., Bouas-Laurent, H., Eds.; Elsevier: Amsterdam, 1990; p 64.

3. Mohrschladt, R.; Troe, J.; Vohringer P. *J. Chem. Phys.* **1994**, *101*, 7566, *and references therein.*

4. Schroeder, J.; Schwarzer, D.; Troe, J.; Voss, F. *J. Chem. Phys.* **1990**, *93*, 2393.

5. Lee, M.; Holtom, G. R.; Hochstrasser, R. M. *Chem. Phys. Lett.* **1985**, *118*, 359.

6. Courtney, S. H.; Fleming, G. R. *J. Chem. Phys.* **1985**, *83*, 215.

7. Courtney, S. H.; Fleming, G. R. *Chem. Phys. Lett.* **1984**, *103*, 443.

8. Syage, J. A.; Felker, P. M.; Zewail, A. H. *J. Chem. Phys.* **1984**, *81*, 4706.

9. Felker, P. M.; Zewail, A. H. *J. Phys. Chem.* **1985**, *89*, 5402.

10. Courtney, S. H.; Balk, M. W.; Phillips, L. A.; Webb, S. P.; Yang, D.; Levy, D. H.; Fleming, G. R. *J. Chem. Phys.* **1988**, *89*, 6697.

11. Khundkar, L. R.; Marcus, R. A.; Zewail, A. H. *J. Phys. Chem.* **1983**, *87*, 2473.

12. Troe, J. *Chem. Phys. Lett.* **1985**, *114*, 241.

13. Negri, F.; Orlandi, G. *J. Phys. Chem.* **1991**, *95*, 748.

14. Baskin, J. S.; Bañares, L.; Pedersen, S.; Zewail, A. H. *J. Phys. Chem.* **1996**, *100*, 11920.

15. Gershinsky, G.; Pollak, E. *J. Chem. Phys.* **1997**, *107*, 812.

16. Syage, J. A.; Lambert, Wm. R.; Felker, P. M.; Zewail, A. H.; Hochstrasser, R. M. *Chem. Phys. Lett.* **1982**, *88*, 266.

17. Heikal, A. A.; Baskin, J. S.; Bañares, L.; Zewail, A. H. *J. Phys. Chem. A* **1997**, *101*, 572.

18. Lienau, Ch.; Heikal, A. A.; Zewail, A. H. *Chem. Phys.* **1993**, *175*, 171.

19. Semmes, D. H.; Baskin, J. S.; Zewail, A. H. *J. Chem. Phys.* **1990**, *92*, 3359.

20. Heikal, A. A.; Chong, S. H.; Baskin, J. S.; Zewail, A. H. *Chem. Phys. Lett.* **1995**, *242*, 380.

21. Perry, J. W.; Scherer, N. F.; Zewail, A. H. *Chem. Phys. Lett.* **1983**, *103*, 1.

22. Balk, M. W.; Fleming, G. R. *J. Phys. Chem.* **1986**, *90*, 3975.

23. Amirav, A.; Jortner, J. *Chem. Phys. Lett.* **1983**, *95*, 295.

24. Orlandi, G.; Siebrand,W. *Chem. Phys. Lett.* **1975**, *30*, 352.

25. Tavan, P.; Schulten, K. *Chem. Phys. Lett.* **1978**, *56*, 200.

26. Orlandi, G.; Palmieri, P.; Poggi, G. *J. Am. Chem. Soc.* **1979**, *101*, 3492.

27. Vachev, V. D.; Frederick J. H.; Grishanin, B. A.; Zadkov, V. N.; Koroteev, N. I. *J. Phys. Chem.* **1995**, *99*, 5247.

28. Marcus, R. A. *Chem. Phys. Lett.* **1995**, *244*, 10.

29. Gershinsky, G.; Pollak, E. *J. Chem. Phys.* **1997**, *107*, 10532.

30. Dillen, J. L. *J. Comput. Chem.* **1995**, *16*, 595.

31. Lienau, Ch.; Schroeder, J.; Troe, J.; Wack, K. *Ber. Bunsenges. Phys. Chem.* **1997**, *101*, 614.

1.2. Figure Captions

Figure 1. Adapted from Ref. 20, this figure shows two different views of a minimum energy structure of tS-hexane$_3$, obtained with Lennard-Jones atom-atom potential energy calculations. The structure without the single hexane above tS, and the structure without the two below, corresponds closely to the minimum energy structures of tS-hexane$_2$ and tS-hexane$_1$, respectively.

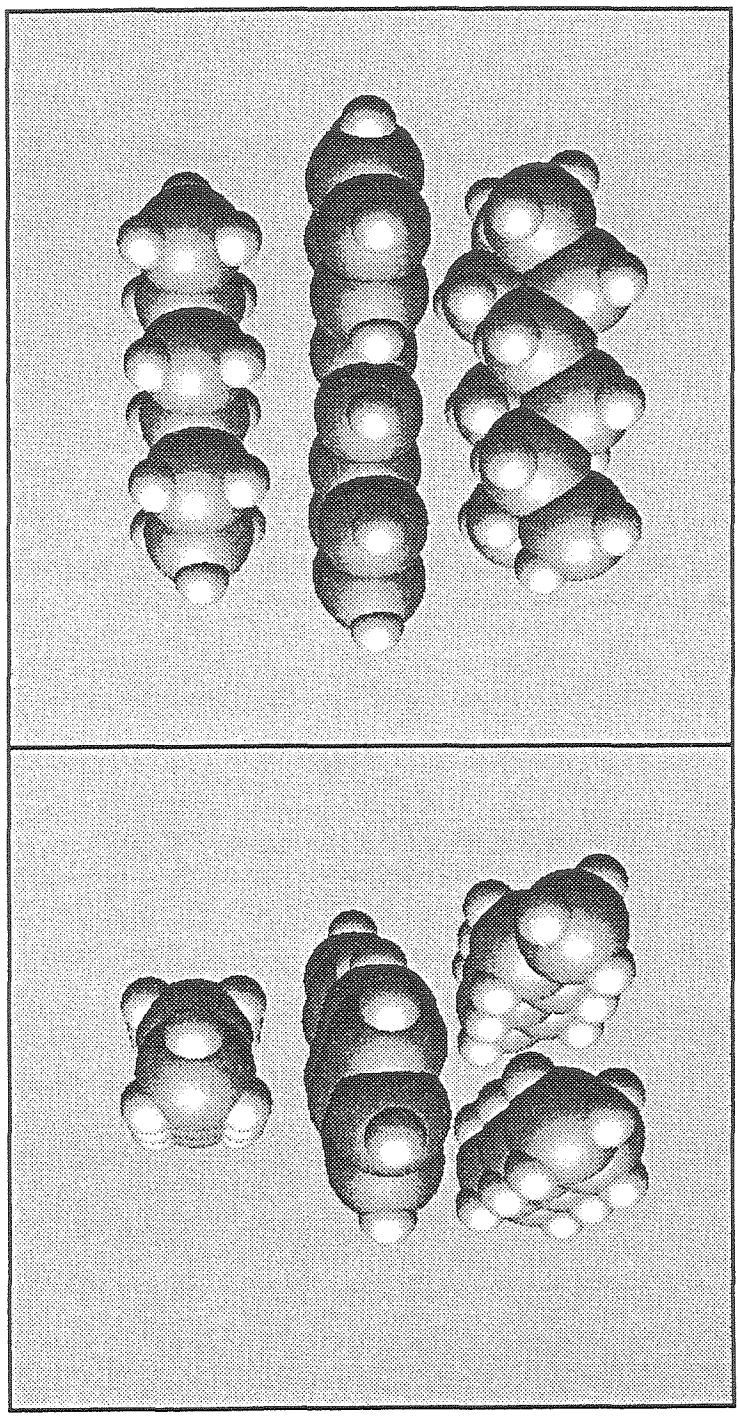

Figure 1

Chapter 2

Experimental Methodology

The experiments described in this thesis involved the use of supersonic expansion [1] and picosecond pump-probe techniques [2]. The picosecond laser system and molecular beam have been described in detail elsewhere [3,4]. Hence, only a brief description with relevant details will be given here. A full description of the sample handling techniques essential to producing well-characterized *trans*-stilbene *n*-alkane complexes is given here for the first time.

2.1. Picosecond Laser Systems. Fig. 1 is a schematic representation of the picosecond laser system. Briefly, the picosecond laser system consists of two home-built cavity-dumped dye lasers, synchronously pumped by the second harmonic (532 nm) of a mode-locked Q-switched Nd:YAG laser. The Nd:YAG laser is also home built, based on the design of a Quantronix model 416 laser. The second harmonic of the Nd:YAG laser was generated with a KTP crystal. The Nd:YAG laser was mode-locked at 76 MHz, and could operate at a Q-switch repetition rate as high as 800 Hz. However, the Q-switch repetition rate was limited to 70 Hz by the frequency of the pulsed gas nozzle. The Q-switch repetition rate in turn determines the repetition rate of the dye lasers.

The duration of the visible pump and probe pulses were around 30-50 ps based on autocorrelation measurement of the pulses with the assumption that they were Gaussian. The spectral width of the pulses was ~ 18 cm^{-1}. The pump and probe laser pulses were frequency-doubled using a KDP crystal and a $LiIO_3$ crystal respectively, and passed through UG-11 filters to remove the fundamental. The

cross-correlation between these UV pulses was 70 ps or less during normal operation, based on the measurement of the rise time of transients. Typically, UV pulse energies were ~ 0.2 μJ, depending on the wavelength selected.

The pump-laser dyes used in the experiments were Rhodamine 590 (R6G), Rhodamine 610, Rhodamine 640, and Sulforhodamine 640 in methanol, which covered the wavelength range of 570-630 nm. For the probe laser, only DCM dye in methanol was used, covering around 620-650 nm. All dyes were purchased from Exciton. The dye laser wavelength was tuned by an intracavity etalon.

The pump-probe delay was achieved with a variable and a static optical delay line. The pump laser, after frequency doubling, was directed to the variable delay line which has a translation stage (Aerotech ATS224) driven by a stepper motor. The translation stage had a spatial resolution of 1 μm/step and a total range of 60 cm, which corresponds to 6.6 fs/step and 4 ns (accounting for round-trip travel) respectively. The probe laser was allowed to pass through a constant delay line before frequency doubling. After frequency doubling, both lasers were directed through UG-11 filters to remove unwanted wavelengths. In order to reduce background signal due to two pump photon ionization, care was taken to reduce the pump laser intensity as much as possible with neutral density filters. Typical background signal for all transient measurements was less than 5% of the total peak signal.

2.2. Molecular Beam Apparatus. Fig. 2 is a schematic representation of the molecular beam apparatus. As can be seen, the beam apparatus consists of three chambers: the expansion chamber, the buffer chamber and the time-of-flight (TOF)

chamber. The expansion chamber was pumped by a Varian VHS-10 diffusion pump, which was backed by a Leybold-Heraeus D90A mechanical pump. The other two chambers were each pumped by a Varian VHS-6 diffusion pump, which were backed jointly by a single Leybold-Heraeus D60A mechanical pump. Typically, when no gas flows from the nozzle, the three chambers can be pumped down to moderately high vacuum, which is ~ 3×10^{-7} Torr for the expansion and buffer chambers, and ~ 1×10^{-7} Torr for the TOF chamber. However, under normal experimental condition where ~ 300 μs gas pulses were introduced into the chambers at a rate of 70 Hz and a backing pressure of 2 atm, the pressure in the expansion and the buffer chambers would increase to ~ 1×10^{-5} Torr while the pressure in the TOF chamber would remain relatively low at ~ 4×10^{-7} Torr.

When satisfactory vacuum had been achieved, tS and its cluster samples were introduced into the expansion chamber through a pulsed nozzle (General Valve, Series 9), which had a pinhole diameter of 150 μm and a conical (30^0) cross section to achieve maximum cluster formation [34]. The pulsed nozzle was mounted on a movable carriage which allowed for the adjustment of x/d ratio (x is the distance between the nozzle and the intersection point of the laser and the gas pulse; d is the nozzle pinhole diameter). The pulse nozzle repetition rate was set at 70 Hz in order to maintain a low vacuum pressure inside the molecular beam chambers. In addition, 70 Hz was chosen because it is approximately the upper limit for stable cluster population generation. The nozzle frequency was the limiting rate at which the data could be collected.

After the initial free expansion in the expansion chamber, the gas pulses containing a mixture of clusters would pass through two skimmers to enter the ionizer cube mounted inside the buffer chamber. In the ionizer cube, tS and its clusters were excited and then ionized by the laser pulses, which were focused onto the samples via a UV lens (f = 30 cm). The ions generated were deflected 90^0 and accelerated by a two-stage electric field into a transition tube where ion optics known as an einzel lens are held. The einzel lens collimates the ions and directs them into a ~ 1.0 m long TOF drift tube, where they were eventually detected by a microchannel plate (Galileo 1396-0050). The detected ion signal was amplified by a factor of 25 with a 300 MHz preamplifier (Stanford Research System, model SR440).

2.3. Data Acquisition. The TOF mass spectra were recorded using a fast waveform analyzer consisting of a 100 MHz transient digitizer (LeCroy 8818A), a memory module (LeCroy MM8103A) and a controller unit (LeCroy 6010 Interface Controller Unit). The analyzer was triggered by a digital delay generator (Stanford Research Systems, model DG535). The digitized TOF mass spectrum was transferred to a microcomputer via a computer interface board (National Instruments, model NB-DMA-8-G GPIB). The mass resolution achieved was $m/\Delta m$ ~ 300 (in the range of the cluster mass we studied).

To obtain the transient of a particular species, a boxcar integrator (Stanford Research Systems, model SR250) was used to gate and collect the signal from that species. The boxcar gate width was normally set at 30-50 ns. The gated signal was averaged with the boxcar integrator prior to being sent to the microcomputer for analysis

via an A/D board (National Instruments, model NB-MIO-16H-9). The decay rates were determined by fitting the transients to a single (or multiple) exponential decay function including convolution with the system response function. The rising edge of the transients was well fitted by a system response of ~ 70 ps.

To verify whether good experimental conditions had been attained (i.e., the pump laser was properly aligned and the cooling of the molecular beam was satisfactory), the lifetime of tS at various excitation energies was measured (as control) after the lifetime of the clusters was determined. The lifetime of bare trans-stilbene at its vibrationless S_1 state was measured to be 2.6 ± 0.2 ns, in good agreement with other measurements in supersonic jet [9,10,11,12]. In general, a transient of bare *trans*-stilbene with reasonably good signal-to-noise can be obtained in less than one hour of scan time. The necessary scan time for clusters was normally around 2-5 hours.

2.4. Sample Handling. Chemicals, including *trans*-stilbene-h_{12} (Aldrich, 97.5% purity), *trans*-stilbene-d_{12} (CDN isotopes, 99.7% D), *n*-hexane-h_{14} (Fluka, 98.6% purity), *n*-hexane-d_{14} (Aldrich, 99% D) and *n*-octane-h_{18} (Aldrich, 99+% purity) were all used without further purification. The tS sample was placed in a 2.5 inch long (0.5 inch diameter) stainless steel compartment attached to the back of the nozzle assembly. The tS sample was heated up to ~ 90 ^{0}C during normal operation with a heating tape that wrapped around the stainless steel compartment. The nozzle temperature, which was controlled by a home-built heating assembly, was set ~ 15 ^{0}C higher at ~ 105 ^{0}C to prevent clogging.

The cluster solvent samples were placed in a 12 in. long (1.5 in. diameter) stainless steel cylinder outside the molecular beam chambers, with the carrier gas passing over the surface of the liquid. The cylinder was designed so it could be immersed into a liquid temperature bath if necessary. When *n*-hexane was used as the cluster sample, a methanol/liquid N_2 bath was adopted to bring the temperature down to maximize the population of the cluster of interest while minimizing the population of the larger clusters to prevent interference from possible fragmentation. The tS-*hexane*$_1$ experiments were generally carried out at solvent temperature between – 60 ^{0}C to – 50 ^{0}C, whilst the tS-*hexane*$_2$ experiments were generally done at – 50 ^{0}C to – 40 ^{0}C. At – 60 ^{0}C, the vapor pressure of hexane is < 1 Torr, and at normal backing pressure of 2 atm, the partial pressure of hexane amounted to less than 0.07% of the total pressure. At – 40 ^{0}C, the vapor pressure of hexane was ~ 5 Torr, which equaled to ~ 0.3% of the total pressure.

When *n*-octane-h_{18} was used as the cluster sample, the solvent sample temperature was set in the range of ~ 5 to 22 ^{0}C for the tS-*octane*$_1$ experiments, and ~ 22 to 50 ^{0}C for the tS-*octane*$_2$ experiments. Octane had relatively lower vapor pressure than hexane, and had to be set at higher temperature for an appreciable amount of n = 1 and 2 clusters to be produced. It was found that tS-*octane*$_n$ (tS-O_n) populations were more difficult to control than those of tS-*hexane*$_n$ (tS-H_n), and the temperature needed for experiments with a given cluster was less well-defined. To achieve the condition where the population of the cluster of interest was adequately produced, but not that of the larger cluster, required a wider range of temperature adjustment. Octane had a vapor pressure ~ 6 Torr at 5 ^{0}C, which amounted to ~ 0.4% of the total backing pressure. At 22 ^{0}C, the vapor pressure of

n-octane was ~ 10 Torr, equivalent to ~ 0.7% of the total backing pressure. At 50 ^{0}C, the vapor pressure of *n*-octane was ~ 54 Torr, equivalent to ~ 3.6% of the total backing pressure.

2.5. Calculation of the Vibrational Frequencies. For computation of the microcanonical isomerization rates, the vibrational frequencies of tS at the S_1 and the transition state were obtained from Ref. 5. Those frequencies were calculated with quantum chemical methods. For tS *n*-alkane complexes, the frequencies of the parent molecule were assumed to remain unchanged. The frequencies of the solvent molecules were computed with DFT method using the Jaguar program [6], employing B3LYP density functionals and 6-31G** basis sets. The intermolecular vibrational frequencies (cluster mode frequencies) of the complexes were obtained with molecular mechanics methods, using the Cerius^2 software package [7] employing the DREIDING forcefield [8]. The solvent and the cluster mode frequencies were assumed to be the same in the S_1 and the transition state.

2.6. References

1. Miller, D. R. In *Atomic and Molecular Beam Methods*; Scoles, G., Ed.; Oxford University Press: Oxford, 1988; Vol. 1, Chapter 2, p 14.

2. Khundkar, L. R.; Zewail, A. H. *Ann. Rev. Phys. Chem.* **1990**, *41*, 15.

3. (a) Willberg, D. M. *Ph.D. Thesis, California Institute of Technology* **1993**. (b) Peng, L. W. *Ph.D. Thesis, California Institute of Technology* **1991**.

4. (a) Kim, S. K.; Breen, J. J.; Willberg, D. M.; Peng, L. W.; Heikal, A.; Syage, J. A.; Zewail, A. H. *J. Phys. Chem.* **1995**, *99*, 7421. (b) Willberg, D. M. ; Gutmann, M.; Breen, J. J.; Zewail, A. H. *J. Chem. Phys.* **1992**, *96*, 198.

5. Negri, F.; Orlandi, G. *J. Phys. Chem.* **1991**, *95*, 748.

6. *Jaguar 3.0*; Schrodinger, Inc.: Portland, OR, 1997.

7. *Cerius*^{2} *3.5*; Molecular Simulations, Inc.: San Diego, CA, 1997.

8. Mayo, S. L.; Olafson, B. D.; Goddard III, W. A. *J. Phys. Chem.* **1990**, *94*, 8897.

9. Syage, J. A.; Felker, P. M.; Zewail, A. H. *J. Chem. Phys.* **1984**, *81*, 4706.

10. Courtney, S. H.; Balk, M. W.; Phillips, L. A.; Webb, S. P.; Yang, D.; Levy, D. H.; Fleming, G. R. *J. Chem. Phys.* **1988**, *89*, 6697.

11. Syage, J. A.; Lambert, Wm. R.; Felker, P. M.; Zewail, A. H.; Hochstrasser, R. M. *Chem. Phys. Lett.* **1982**, *88*, 266.

12. Amirav, A.; Jortner, J. *Chem. Phys. Lett.* **1983**, *95*, 295.

2.7. Figure Captions

Figure 1. Schematic diagram of the picosecond laser system. M: mirror, QS: Q-Switch, LH: laser head, I: iris, P: polarizer, ML: modelocker, OC: output coupler, SHG: crystal for single harmonic generation, $\lambda/2$: half-waveplate, L: lens, BS: beam splitter, PC: pockel cell, GEW: Glan escape window, E: etalon, DC: dye cell, CC: corner cube, VDL: variable delay line.

Figure 2. Schematic diagram of the molecular beam apparatus with the expansion, the buffer and the time-of-flight (TOF) chambers. Each of these chambers was pumped by a separate diffusion pump. The laser pulses, the gas pulses and the TOF chamber were orthogonal to one another. MCP: microchannel plate.

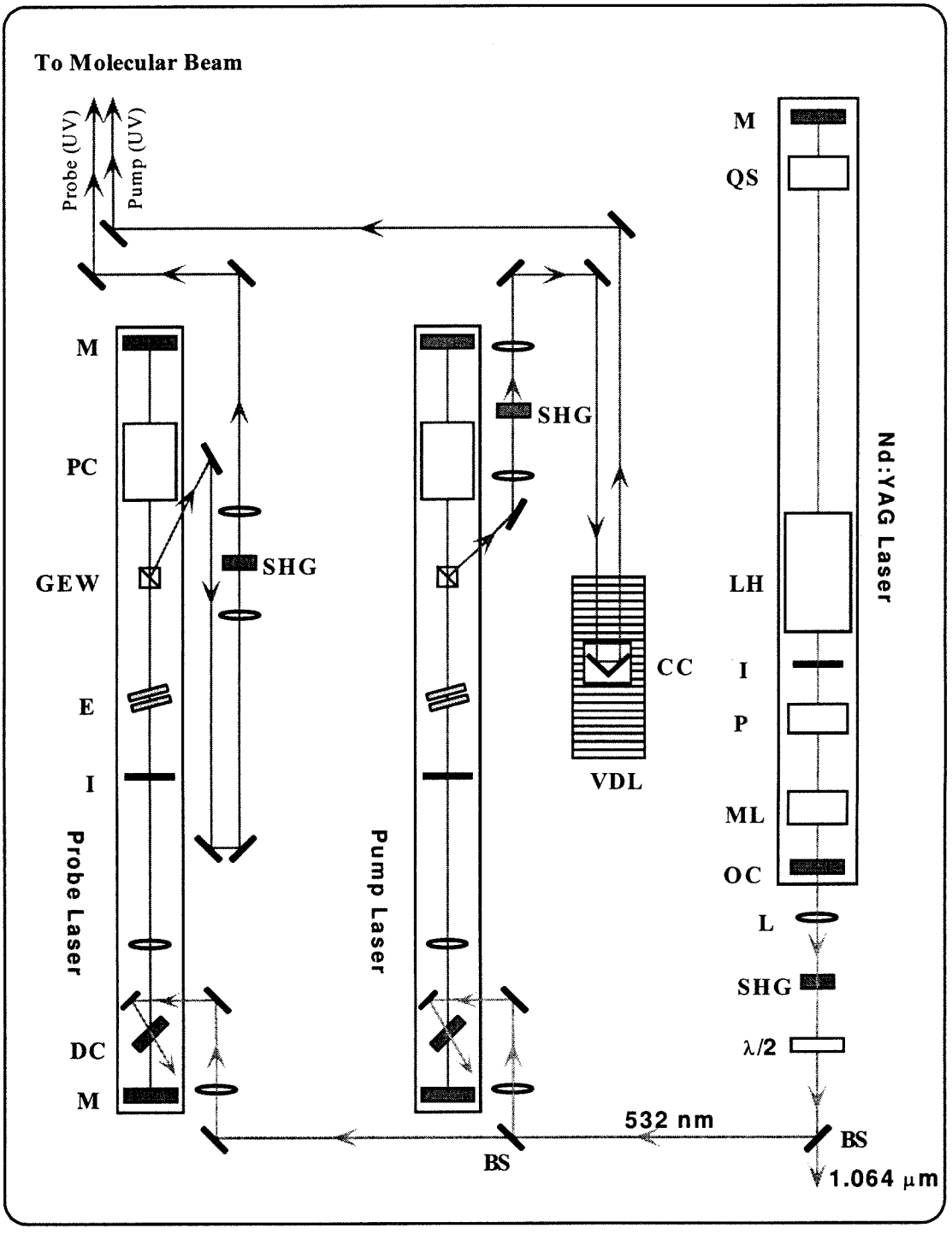
To Molecular Beam
Probe (UV)
Pump (UV)
M
PC
GEW
SHG
E
I
Probe Laser
DC
M
SHG
Pump Laser
BS
CC
VDL
M
QS
LH
I
P
ML
OC
L
SHG
λ/2
Nd:YAG Laser
532 nm
BS
1.064 μm

Figure 1

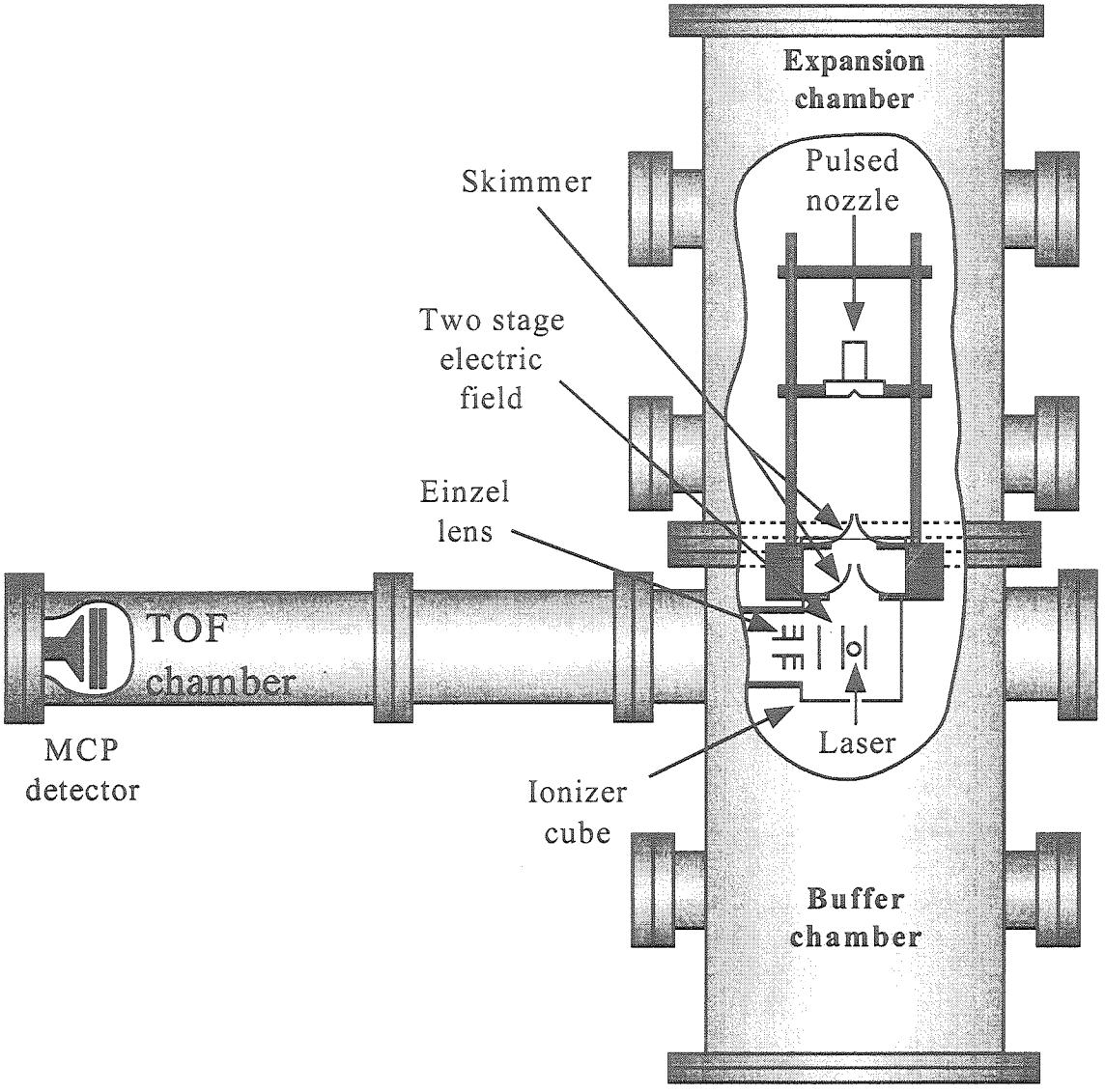
Expansion chamber
Pulsed nozzle
Skimmer
Two stage electric field
Einzel lens
TOF chamber
MCP detector
Laser
Ionizer cube
Buffer chamber

Figure 2

Chapter 3

Results

3.1. Mass Spectra and Transients. Typical TOF mass spectra of tS-h_{12}-(hexane-h_{14})$_n$ (henceforth referred to simply as tS-H$_n$), n = 0-4, are shown in Fig. 1 to illustrate the general distribution of cluster population at four different solvent temperatures. Pump excitation was at the tS-h_{12} S_1 origin, and the total pump + probe energy was ~ 1330 cm^{-1} above the tS-h_{12} ionization continuum, based on the ionization potential determined by Takahashi and Kimura (61748 cm^{-1}) [1] and by Suzuki *et al.* (61750 cm^{-1}) [2]. Note that when the pump and the probe pulses intersect with the molecular beam, cluster species of all sizes may be excited and ionized, provided they have favorable excitation and ionization cross-sections, and fragmentation of larger clusters may introduce complications in interpretation of a measurement at a given mass. Thus, it was desirable to generate the cluster of interest without producing significant amounts of larger clusters. As shown in Fig. 1, this could be done for tS-H$_1$ (at – 60 ^{0}C) and tS-H$_2$ (at – 50 ^{0}C). However, for clusters with n = 3 or greater, the ratio of higher cluster populations to the population of tS-H$_n$ could not be reduced to an insignificant level at any temperature, despite numerous attempts.

Although cluster size as high as n = 6 can be observed with the solvent temperature at ~ 22 ^{0}C [3], we will only focus on results for clusters with n = 1 and 2 in this thesis. For the excitation range employed in the present experiments, changes in the lifetimes of clusters with n > 2 are simply too small to be resolved accurately. The range of the pump excitation energy used was from the origin of tS-h_{12} $S_1 \leftarrow S_0$ excitation to ~ 3200 cm^{-1} higher in energy.

Even when the tS-A_n mass (A representing any alkane) appears in the TOF mass spectrum without noticeable presence of tS-A_{n+1}, there is no guarantee that the observed TOF signal at the mass of tS-A_n is only coming from the intact tS-A_n population. Aside from being produced via the excitation and then ionization of the primary tS-A_n population, tS-A_n^+ can be formed from vibrational predissociation (vp) of tS-A_{n+1}^+ at the ion state. In addition, if the excited tS-A_{n+1}^* predissociates at the S_1 state to form tS-A_n^* + A before the probe pulse arrives, the *nascent* tS-A_n^* can also be ionized to form tS-A_n^+. As a result, during transient measurements, even though a boxcar gate was placed at a position equal to the TOF mass of tS-A_n, the kinetics being measured may have multiple origins. Therefore, a kinetic scheme will be developed later in this thesis (chapter 4) to examine the effect of vp on the overall kinetics of the transient being measured and properly attribute the measured rates. In the following, we will first present the data and rates directly as measured at given ion cluster mass.

As mentioned earlier, the transients of the cluster species of interest were measured with the time-resolved pump-probe ionization technique. Sample transients recorded gating at the time-of-flight peak of the mass of several different species, including that of perprotio tS (tS-h_{12}) and several of its *n*-alkane complexes, and that of tS-d_{12}-(H-d_{14})$_1$, are shown in Fig. 2 to Fig. 6. Note that it is possible a few of the transients shown in these figures might appear to have better signal-to-noise ratios than they actually do because they might have been "physically smoothed" (see appendix III). The excess energy, E_{ex}, the difference between the energy of the pump photon and that of the $S_1(v' = 0) \leftarrow S_0(v'' = 0)$ transition of the specified cluster, is indicated for each

transient. Also, note that for a red shift of the tS $S_1(v' = 0) \leftarrow S_0(v'' = 0)$ transition in the clusters, the excess internal vibrational energy attained at a given fixed pump wavelength by tS-A_n is higher than that acquired by bare tS.

Since only the red shift in the 0-0 excitation of tS-H_1 was measured experimentally [4], the red shift of other cluster species were estimated based on the assumption that the red shift of a chromophore increases almost linearly as a function of increasing solvent number [6] and solvent chain length [7]. We use here the value of 380 cm^{-1} for the red-shift of tS-H_1 relative to bare tS [4]. The red shift estimate for tS-O_1 (507 cm^{-1}) was obtained by scaling the red shift of tS-H_1 by the number of carbon atoms, while the estimates for each tS-A_2 was obtained by simply multiplying the estimate for tS-A_1 by two. The tS clusters with fully deuterated solvent species were all assumed to have the same red shift as their perprotio counterparts. All of the tS-d_{12} clusters, complexing with perprotio or perdeuterio *n*-alkanes, were assumed to have the same red shift as their tS-h_{12} clusters counterparts, with respect to the 0-0 excitation of tS-d_{12}. Note that the 0-0 transition of tS-d_{12} is 93 cm^{-1} higher in energy than that of tS-h_{12} [8].

3.2. Excess Energy Dependent Studies. The $k_{nr}(E_{ex})$ vs. E_{ex} data for tS and all the cluster species investigated are tabulated in Table 1 to 13. Fig. 7 presents the excess energy dependence of the nonradiative decay rates for tS-h_{12} and its *n*-hexane-h_{14} and *n*-octane-h_{18} complexes. Most of the transients obtained in our studies could be fitted very well to a single exponential decay function convoluted with the instrumental response. However, there were a few transients of tS-H_1 and many of tS-O_1 that exhibited biexponential decays. In those cases, both k_1 and k_2 are plotted in Fig. 10. The

origin of the long component in such transients, which accounts for ~ 30% or less of the total amplitude in most cases, will be discussed later.

In order to demonstrate that good vibrational cooling was attained under the expansion conditions we utilized, Fig. 8 shows a comparison of $k_{nr}(E_{ex})$ vs. E_{ex} measurements obtained from our experiments and that obtained from the literature [9], for both tS-h_{12} and tS-d_{12} species. In addition, the data for two sets of control experiments, one obtained under the same conditions as the experiments performed on tS-H_1 and the other collected under the same conditions as experiments on tS-O_1, are also included in Fig. 8. As can be seen, the tS lifetimes measured under those conditions did not vary much from that measured under pure He.

(a) Results for tS-H_1 and tS-H_2. For clearer illustration, a separate plot of the $k_{nr}(E_{ex})$ vs. E_{ex} results for tS-H_1 and tS-H_2 is shown in Fig. 9. As can be seen in the figure, the total nonradiative decay rate for tS-H_1 remains fairly constant from E_{ex} ~ 380 cm^{-1} to ~ 1000 cm^{-1} and then increases monotonically from E_{ex} ~ 1100 cm^{-1} to ~ 2580 cm^{-1}. The rate then drops off abruptly after E_{ex} ~ 2580 cm^{-1}, and rises slowly again at higher excess energy. However, note that the transients measured at E_{ex} ~ 2380 cm^{-1}, 2580 cm^{-1}, 2980 cm^{-1} and 3180 cm^{-1} have minor long components (the origin of these long components will be discussed in chapter 4). It can be seen that, unlike tS-H_1, the trend exhibited by the tS-H_2 data is not very dramatic or clear. Since the fluctuations in the data points for tS-H_2 are almost within experimental uncertainty, interpretation of the results will be given after the kinetic scheme is introduced later in chapter 4.

Nonetheless, it seems that the rate remains fairly constant from E_{ex} of ~ 700 cm^{-1} to ~ 1500 cm^{-1}. After that, in general, the total decay rate of tS-H_2 seems to be increasing slowly, albeit not monotonically, with increasing E_{ex}. Note that the tS-H_1 and tS-H_2 results reported here are different from those reported in Ref. 3, due to the more effective vibrational cooling achieved in the cluster forming expansions used in the present study, as clearly demonstrated by the respective control experiments.

(b) Results for tS-O_1 and tS-O_2. Excess energy dependent studies were performed on tS *n*-octane clusters in order to investigate the effects of increasing the solvent chain length on tS photoisomerization dynamics. It can be seen in Fig. 7 that the total decay rate for tS-O_1 remains fairly constant below E_{ex}~ 700 cm^{-1}, and then increases monotonically until 3510 cm^{-1}. At E_{ex} ~ 3710 cm^{-1}, the total decay rate registered a slight drop off. More so than the case of tS-H_2, the total decay rate of tS-O_2 does not show meaningful increase with increasing excess vibrational energy. Although $k_{nr}(E_{ex})$ does show a very small rise from E_{ex}~ 1400 cm^{-1} to ~ 4000 cm^{-1}, the small magnitude of the rise coupled with the low S/N ratio of the data does not allow one to make a precise analysis.

(c) Results for tS-h_{12}-(H-d_{14})$_1$, tS-d_{12}-(H-h_{14})$_1$ and tS-d_{12}-(H-d_{14})$_1$. Deuteration has a dramatic effect on the microcanonical isomerization rate of tS [9], and this effect provides a test of isomerization models. A similar test was undertaken here with studies of the effect of deuteration in tS-H_1 clusters, as shown in Fig. 10. As can be seen, deuteration of tS in the cluster does have a large effect on the rates, while substituting *n*-

hexane-h_{14} with *n*-hexane-d_{14} has little effect, except possibly above 2200 cm^{-1} in tS-h_{12}-H_1.

(d) Results from frequencies calculations. The S_1 and nonadiabatic transition state frequencies for tS-h_{12} and tS-d_{12} were obtained from Ref. 5, and they are listed in Tables 14 to 17. The vibrational frequencies of *n*-hexane-h_{14}, *n*-hexane-d_{14} and *n*-octane-h_{18} calculated with DFT methods are listed in Tables 18, 19 and 20. The intermolecular cluster mode frequencies obtained with molecular mechanics methods are listed in Table 21.

3.3. References

1. Takahashi, M.; Kimura, K. *J. Phys. Chem.* **1995**, *99*, 1628.

2. Suzuki, T.; Mikami, N.; Ito, M. *Chem. Phys. Lett.* **1985**, *120*, 333.

3. Heikal, A. A.; Chong, S. H.; Baskin, J. S.; Zewail, A. H. *Chem. Phys. Lett.* **1995**, *242*, 380.

4. Lienau, Ch.; Heikal, A. A.; Zewail, A. H. *Chem. Phys.* **1993**, *175*, 171.

5. Negri, F.; Orlandi, G. *J. Phys. Chem.* **1991**, *95*, 748.

6. Henke, W. E.; Yu, W.; Selzle, H. L.; Schlag, E. W.; Wutz, D.; Lin, S. H. *Chem. Phys.* **1985**, *92*, 187.

7. Sinha, H. K.; Abou-Zied, O. K.; Ludwiczak, M.; Maciejewski, A.; Steer, R. P. *Chem. Phys. Lett.* **1994**, *230*, 547.

8. Syage, J. A.; Felker, P. M.; Zewail, A. H. *J. Chem. Phys.* **1984**, *81*, 4685.

9. Felker, P. M.; Zewail, A. H. *J. Phys. Chem.* **1985**, *89*, 5402.

3.4. Figure Captions

Figure 1. The time-of-flight (TOF) mass spectra of tS and tS-hexane$_n$ (n = 0-4) clusters at three different hexane temperature. The He backing pressure was 2 atm. The pump and probe excitation wavelengths were 310.1 nm (tS 0-0 excitation) and 323.9 nm, respectively. The total pump + probe energy was ~ 1330 cm^{-1} above the tS ionization continuum.

Figure 2. Measured transients of bare tS-h_{12} in He at λ_{pump} = 310.1 nm (0-0 excitation), 302.6 nm, 295.5 nm, 288.6 nm and 283.7 nm; λ_{probe} was set constant at 324.1 nm in all cases. All the transients are well fitted with convoluted single exponential decay functions, as indicated by the solid lines. The decay lifetimes for all excitation energies are shown. Molecular beam conditions were: 2 atm pure He; ~ 300 μs gas pulse width.

Figure 3. Measured transients of tS-h_{12}-(H-h_{14})$_1$ cluster at λ_{pump} = 310.1 nm, 302.6 nm, 295.5 nm, 290.3 nm and 283.7 nm; λ_{probe} was set constant at 324.1 nm in all cases. All the transients are well fitted with convoluted single exponential decay functions, except at λ_{pump} = 290.3 nm, where a minor slow component was observed. The decay lifetimes for all excitation energies are shown. Molecular beam conditions were: 2 atm He flowing over the surface of approx. – 60 ^{0}C hexane solvent; 280-380 μs gas pulse width.

Figure 4. Measured transients of tS-h_{12}-(H-h_{14})$_2$ cluster at λ_{pump} = 310.1 nm, 304.5 nm, 299.0 nm, 293.7 nm and 287.0 nm; λ_{probe} was set constant at 324.1 nm in all cases. The decay lifetimes for all excitation energies are shown. Molecular beam conditions were: 2 atm He flowing over the surface of approx. – 50 ^{0}C hexane solvent; 280-380 μs gas pulse width.

Figure 5. Measured transients of tS-h_{12}-(O-h_{18})$_1$ cluster at λ_{pump} = 310.1 nm, 299.0 nm, 293.7 nm, 287.0 nm and 283.7 nm; λ_{probe} was set constant at 324.1 nm in all cases. The decay lifetimes for all excitation energies are shown. Molecular beam conditions were: 2 atm He flowing over the surface of approx. 5-22 ^{0}C octane solvent; 350-400 μs gas pulse width.

Figure 6. Measured transients of tS-d_{12}-(H-d_{14})$_1$ cluster at λ_{pump} = 310.1 nm, 302.6 nm, 295.5 nm, 290.3 nm and 283.7 nm; λ_{probe} was set constant at 324.1 nm in all cases. The decay lifetimes for all excitation energies are shown. Molecular beam conditions were: 2 atm He flowing over the surface of approx. – 60 ^{0}C hexane-d_{12} solvent; 320-380 μs gas pulse width.

Figure 7. Excess energy dependence of the nonradiative rate constant in the S_1 manifold of bare tS-h_{12}, and tS-h_{12}-(H-h_{14})$_n$ and tS-h_{12}-(O-h_{18})$_n$ clusters (n = 1,2). The data shown here for the hexane and octane clusters represents measurements made when the boxcar gate was placed at the TOF position corresponds to each species. No consideration was given as of this point to whether the signal was coming from direct ionization of the primary species or from fragmentation of larger clusters.

Figure 8. Comparison of the excess energy dependence results for tS from our experiments with that from Felker *et al.* [9]. As can be seen, the measurements obtained under pure He and under He/*n*-alkane mixture, with pump-probe TOF technique, all agreed well with that measured with the time-correlated single photon counting method.

Figure 9. Excess energy dependence of the nonradiative rate constant in the S_1 manifold of tS-h_{12}-(H-h_{14})$_1$ and tS-h_{12}-(H-h_{14})$_2$ clusters. The data shown here represent measurements made when the boxcar gate was placed at the TOF position corresponding to each species.

Figure 10. $k_{nr}(E_{ex})$ vs. E_{ex} results for tS-h_{12}-H_1 (-h_{14} and -d_{14}) and tS-d_{12}-H_1 (-h_{14} and -d_{14}). As can be seen, changing the solvent and intermolecular vibrational density of states did not alter the nonradiative rates in any meaningful way.

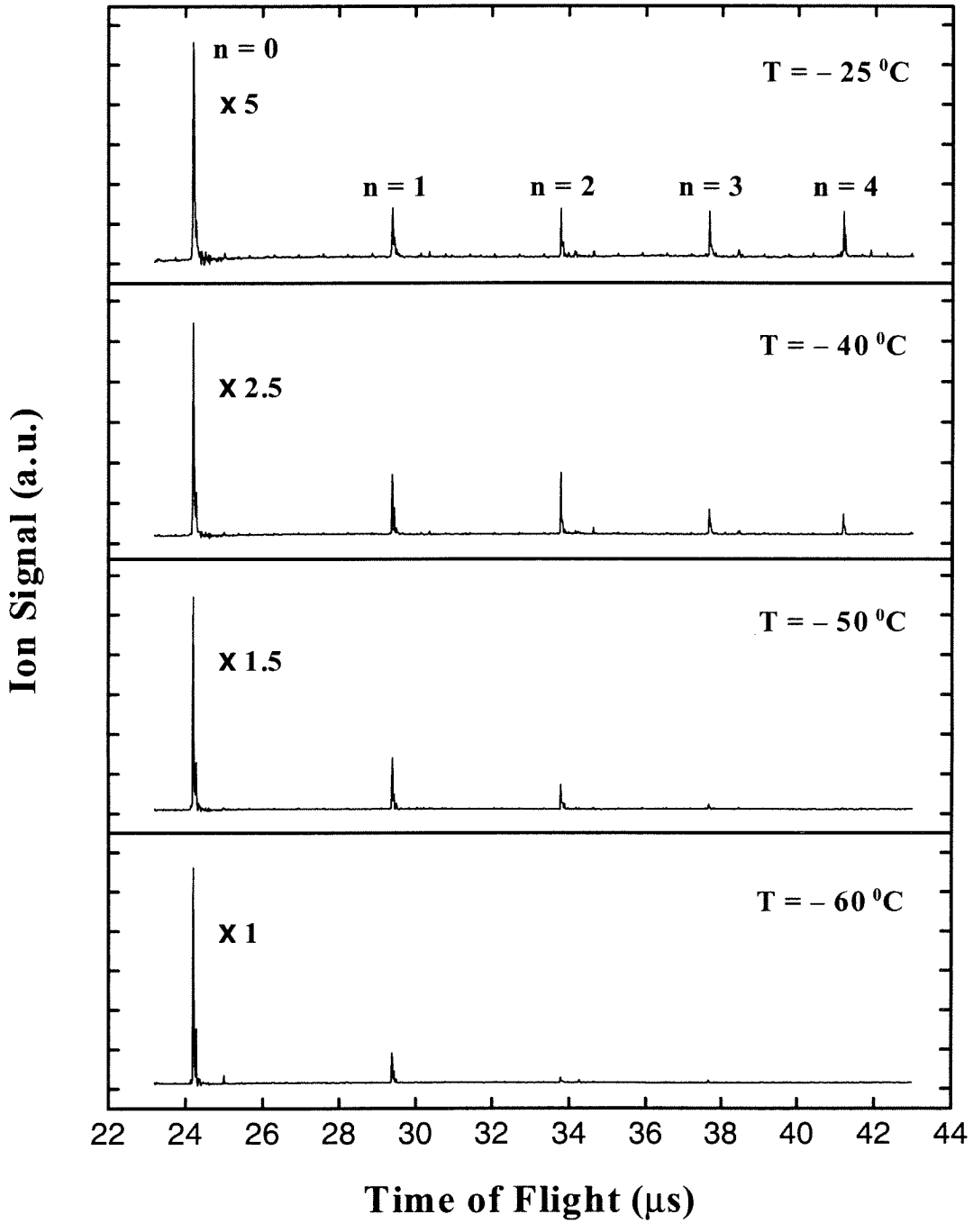
n = 0
x 5
n = 1
n = 2
n = 3
n = 4
T = – 25 °C
T = – 40 °C
x 2.5
T = – 50 °C
x 1.5
T = – 60 °C
x 1
Ion Signal (a.u.)
22
24
26
28
30
32
34
36
38
40
42
44
Time of Flight (μs)

Figure 1

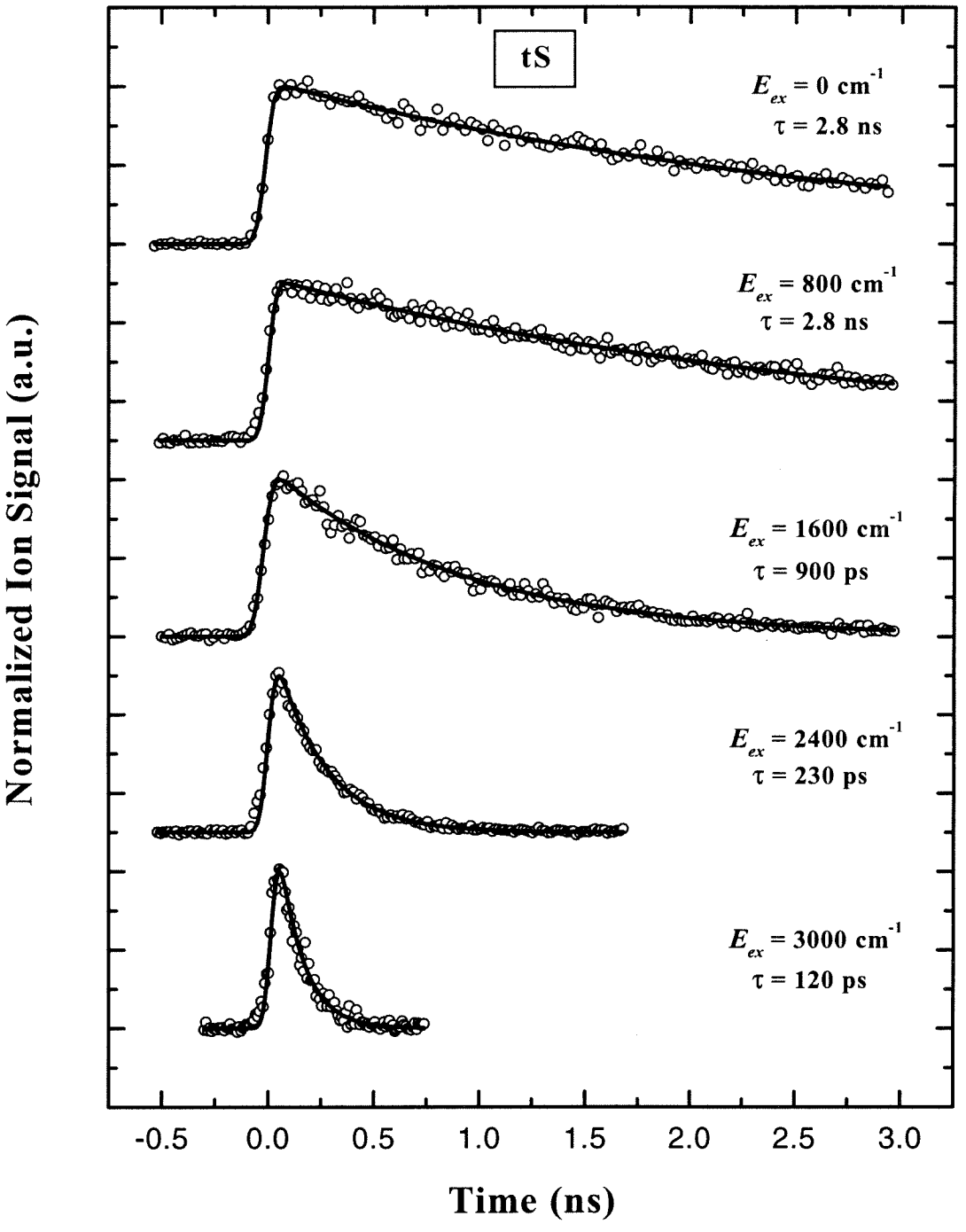
tS
E_{ex} = 0 cm^{-1}
τ = 2.8 ns
E_{ex} = 800 cm^{-1}
τ = 2.8 ns
E_{ex} = 1600 cm^{-1}
τ = 900 ps
E_{ex} = 2400 cm^{-1}
τ = 230 ps
E_{ex} = 3000 cm^{-1}
τ = 120 ps
Normalized Ion Signal (a.u.)
-0.5
0.0
0.5
1.0
1.5
2.0
2.5
3.0
Time (ns)

Figure 2

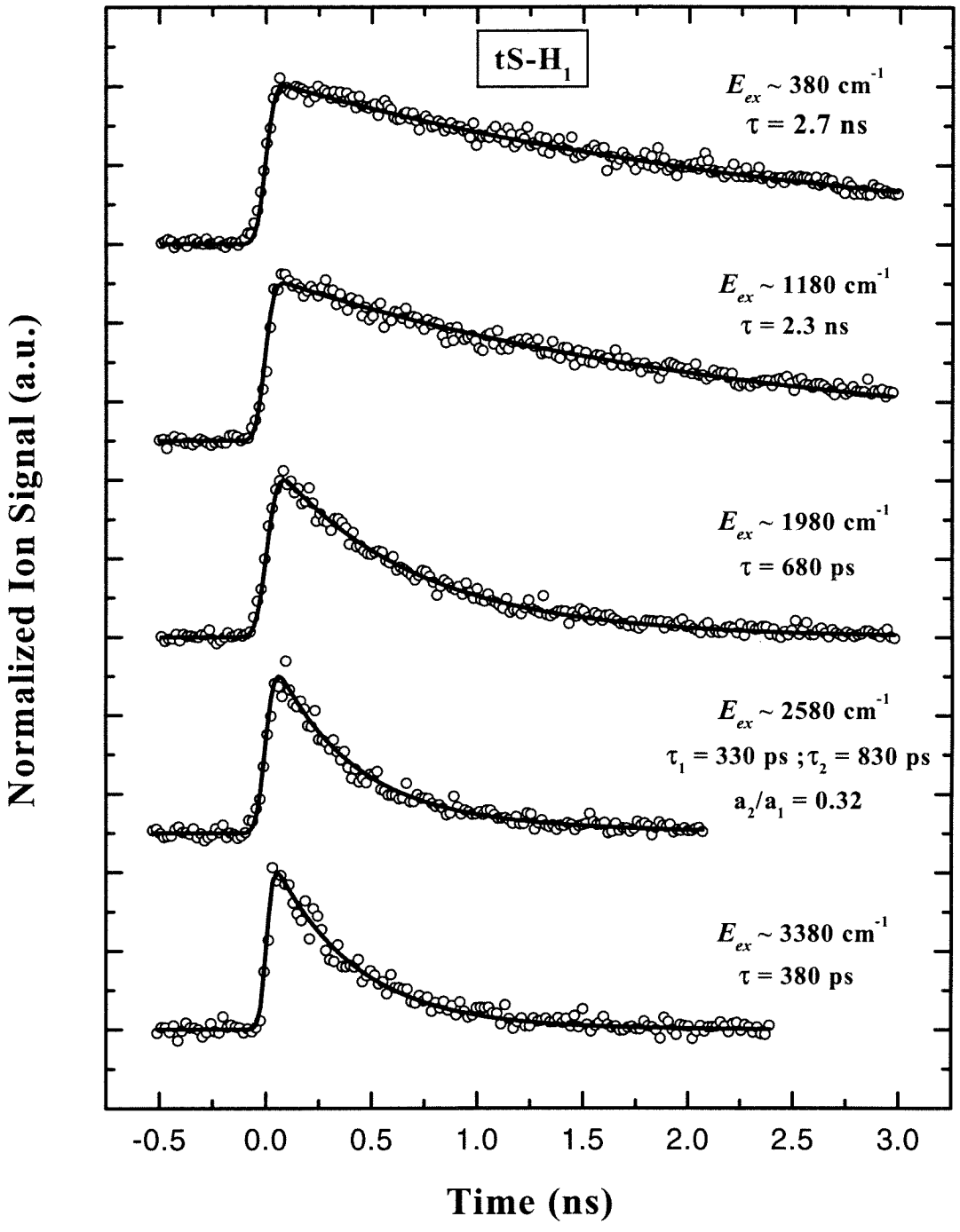
tS-H1
Eex ~ 380 cm-1
τ = 2.7 ns
Eex ~ 1180 cm-1
τ = 2.3 ns
Eex ~ 1980 cm-1
τ = 680 ps
Eex ~ 2580 cm-1
τ1 = 330 ps ;τ2 = 830 ps
a2/a1 = 0.32
Eex ~ 3380 cm-1
τ = 380 ps
Normalized Ion Signal (a.u.)
-0.5
0.0
0.5
1.0
1.5
2.0
2.5
3.0
Time (ns)

Figure 3

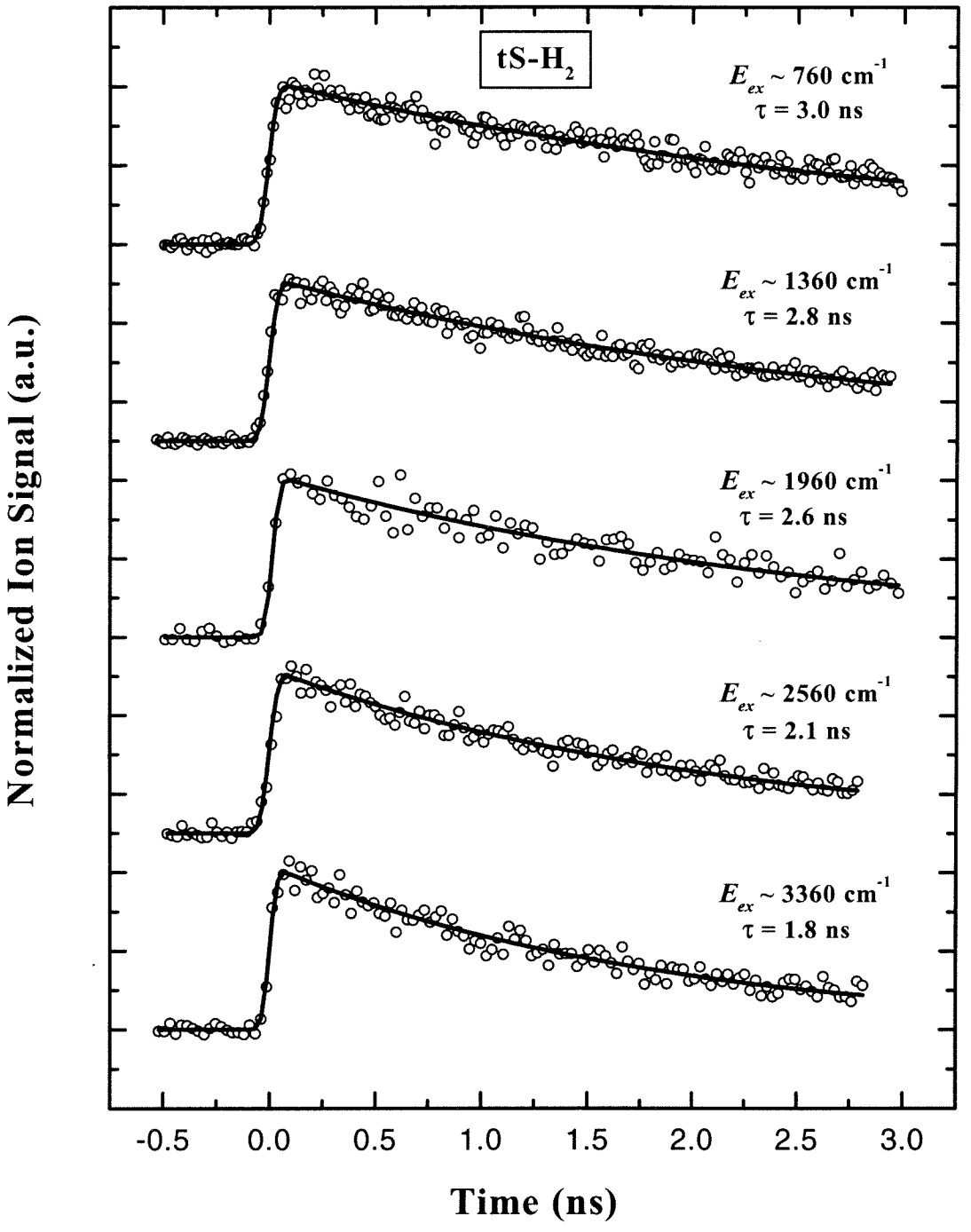
tS-H2
Eex ~ 760 cm-1
τ = 3.0 ns
Eex ~ 1360 cm-1
τ = 2.8 ns
Eex ~ 1960 cm-1
τ = 2.6 ns
Eex ~ 2560 cm-1
τ = 2.1 ns
Eex ~ 3360 cm-1
τ = 1.8 ns
Normalized Ion Signal (a.u.)
-0.5
0.0
0.5
1.0
1.5
2.0
2.5
3.0
Time (ns)

Figure 4

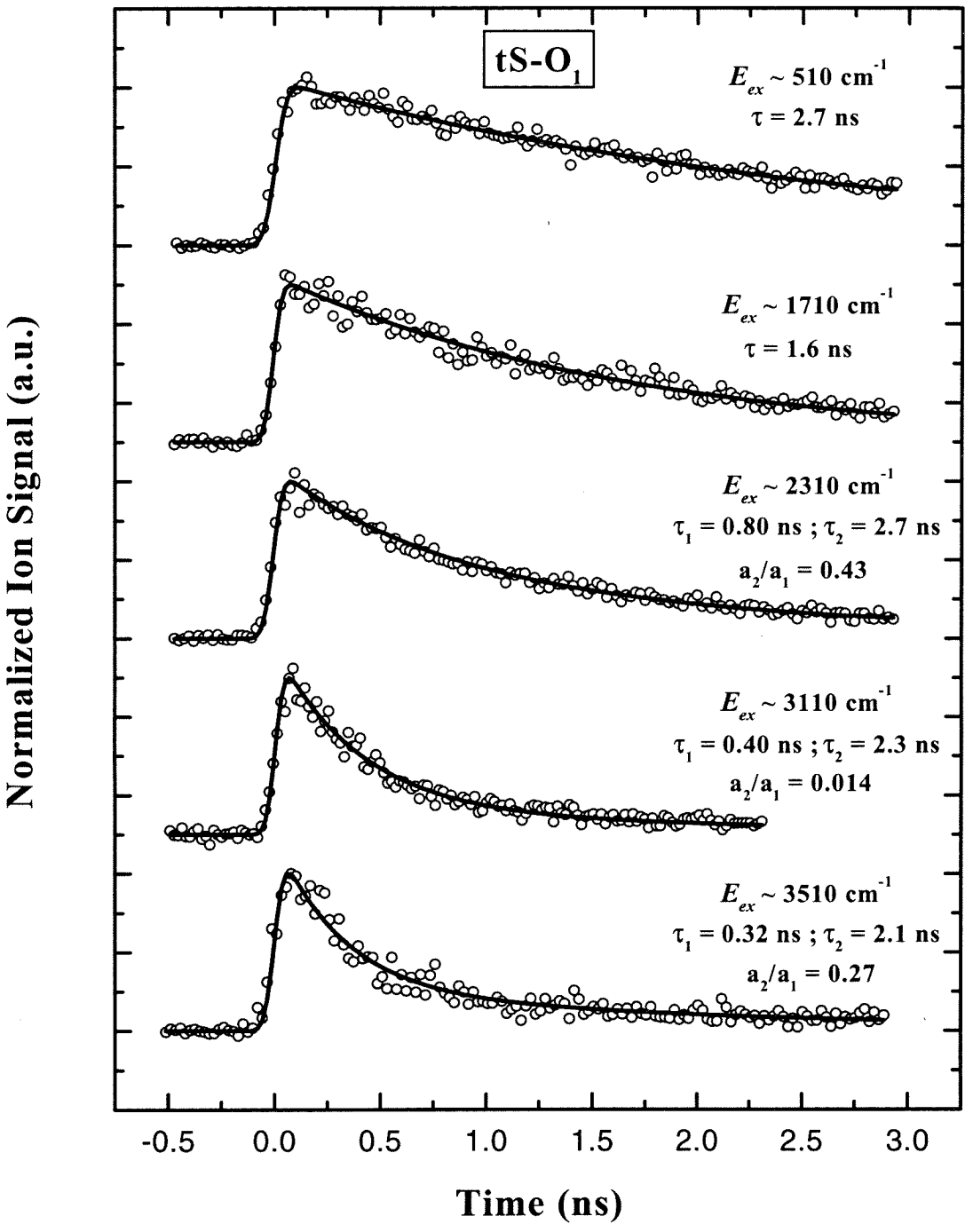
tS-O1
Eex ~ 510 cm-1
τ = 2.7 ns
Eex ~ 1710 cm-1
τ = 1.6 ns
Eex ~ 2310 cm-1
τ1 = 0.80 ns ; τ2 = 2.7 ns
a2/a1 = 0.43
Eex ~ 3110 cm-1
τ1 = 0.40 ns ; τ2 = 2.3 ns
a2/a1 = 0.014
Eex ~ 3510 cm-1
τ1 = 0.32 ns ; τ2 = 2.1 ns
a2/a1 = 0.27
Normalized Ion Signal (a.u.)
-0.5
0.0
0.5
1.0
1.5
2.0
2.5
3.0
Time (ns)

Figure 5

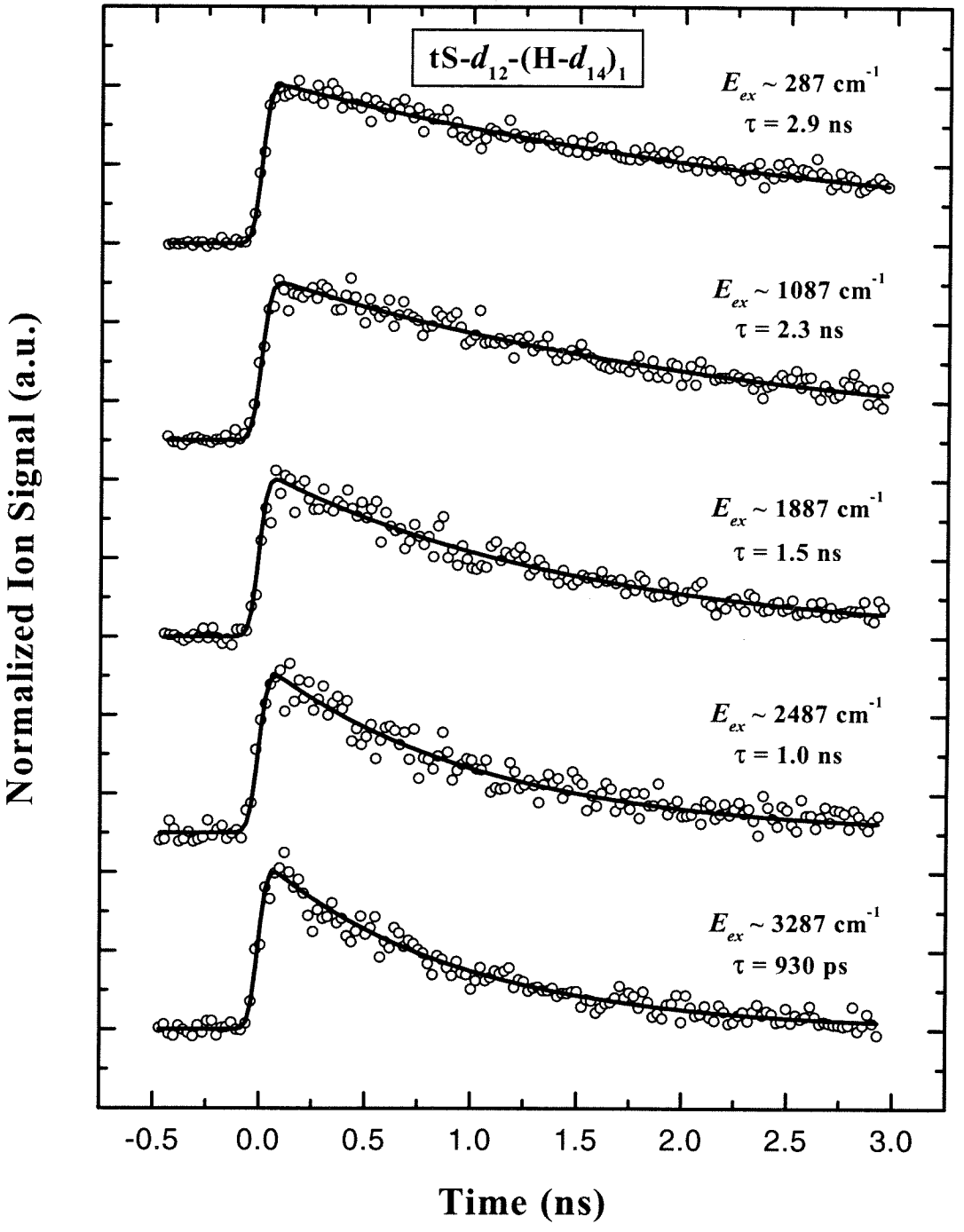
tS-d_{12}-(H-d_{14})$_1$
E_{ex} ~ 287 cm^{-1}
τ = 2.9 ns
E_{ex} ~ 1087 cm^{-1}
τ = 2.3 ns
E_{ex} ~ 1887 cm^{-1}
τ = 1.5 ns
E_{ex} ~ 2487 cm^{-1}
τ = 1.0 ns
E_{ex} ~ 3287 cm^{-1}
τ = 930 ps
Normalized Ion Signal (a.u.)
-0.5
0.0
0.5
1.0
1.5
2.0
2.5
3.0
Time (ns)

Figure 6

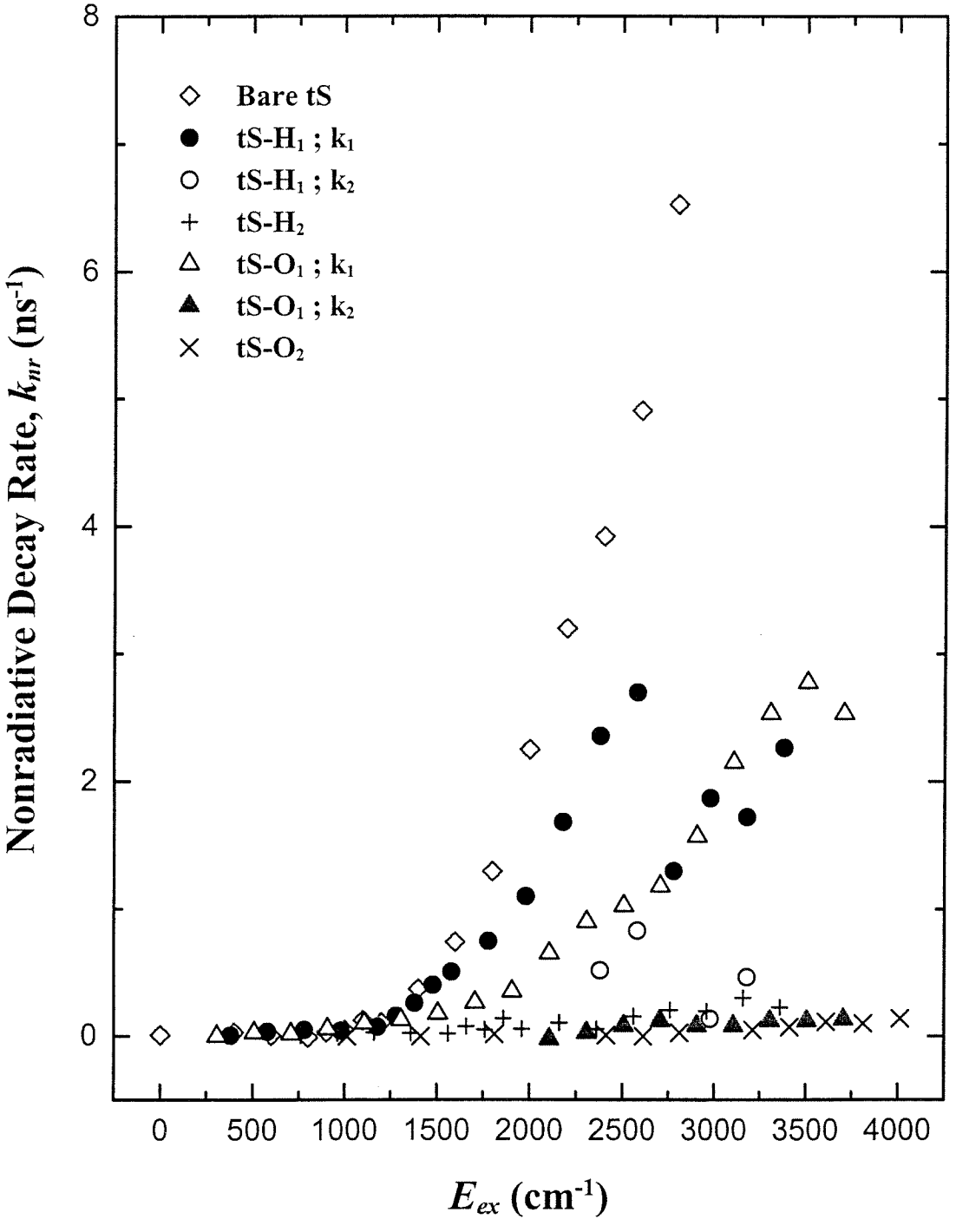
Bare tS
tS-H1 ; k1
tS-H1 ; k2
tS-H2
tS-O1 ; k1
tS-O1 ; k2
tS-O2
Nonradiative Decay Rate, knr (ns-1)
Eex (cm-1)
0
2
4
6
8
0
500
1000
1500
2000
2500
3000
3500
4000

Figure 7

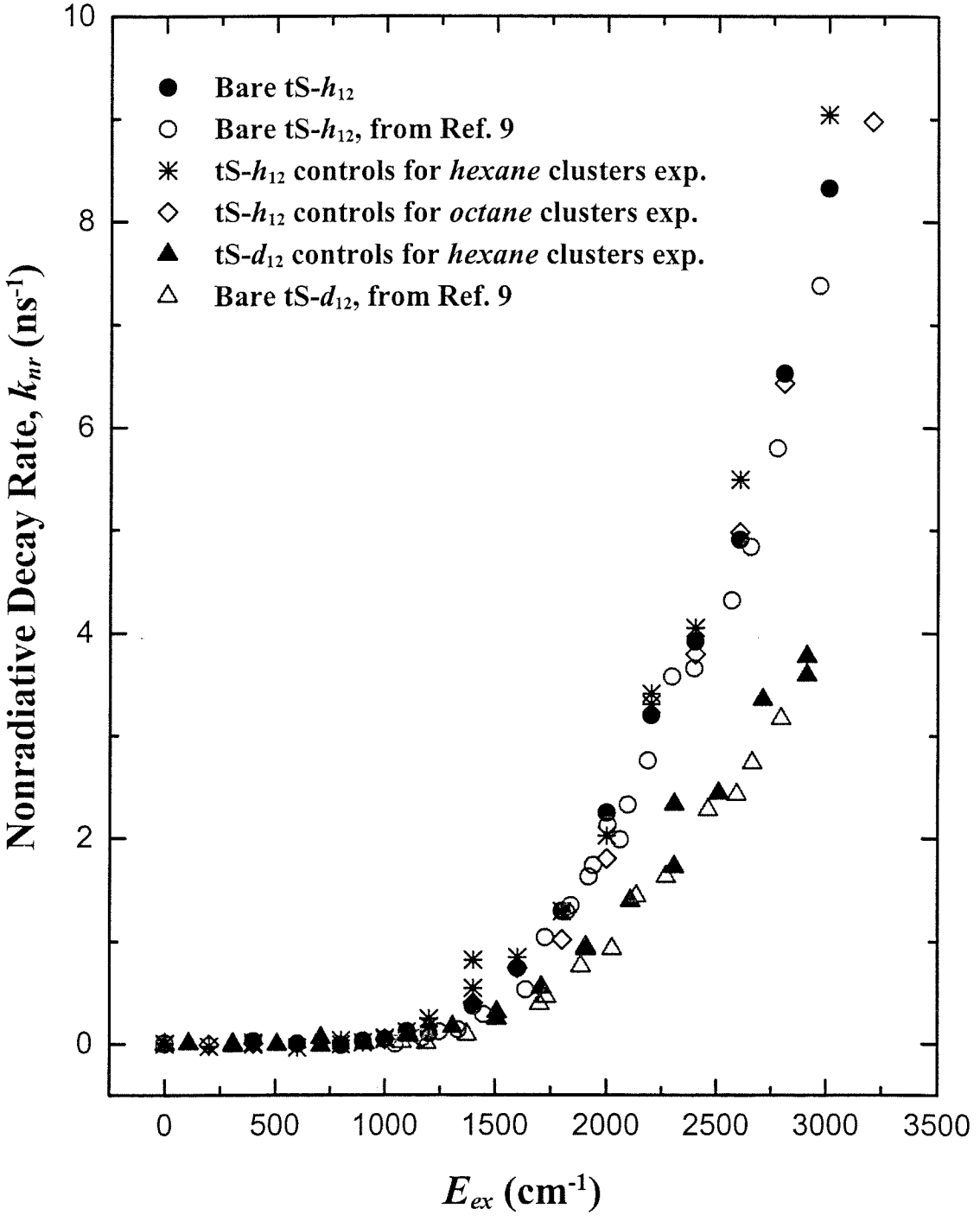
Bare tS-h_{12}
Bare tS-h_{12}, from Ref. 9
tS-h_{12} controls for *hexane* clusters exp.
tS-h_{12} controls for *octane* clusters exp.
tS-d_{12} controls for *hexane* clusters exp.
Bare tS-d_{12}, from Ref. 9
Nonradiative Decay Rate, k_{nr} (ns^{-1})
E_{ex} (cm^{-1})
0
2
4
6
8
10
0
500
1000
1500
2000
2500
3000
3500

Figure 8

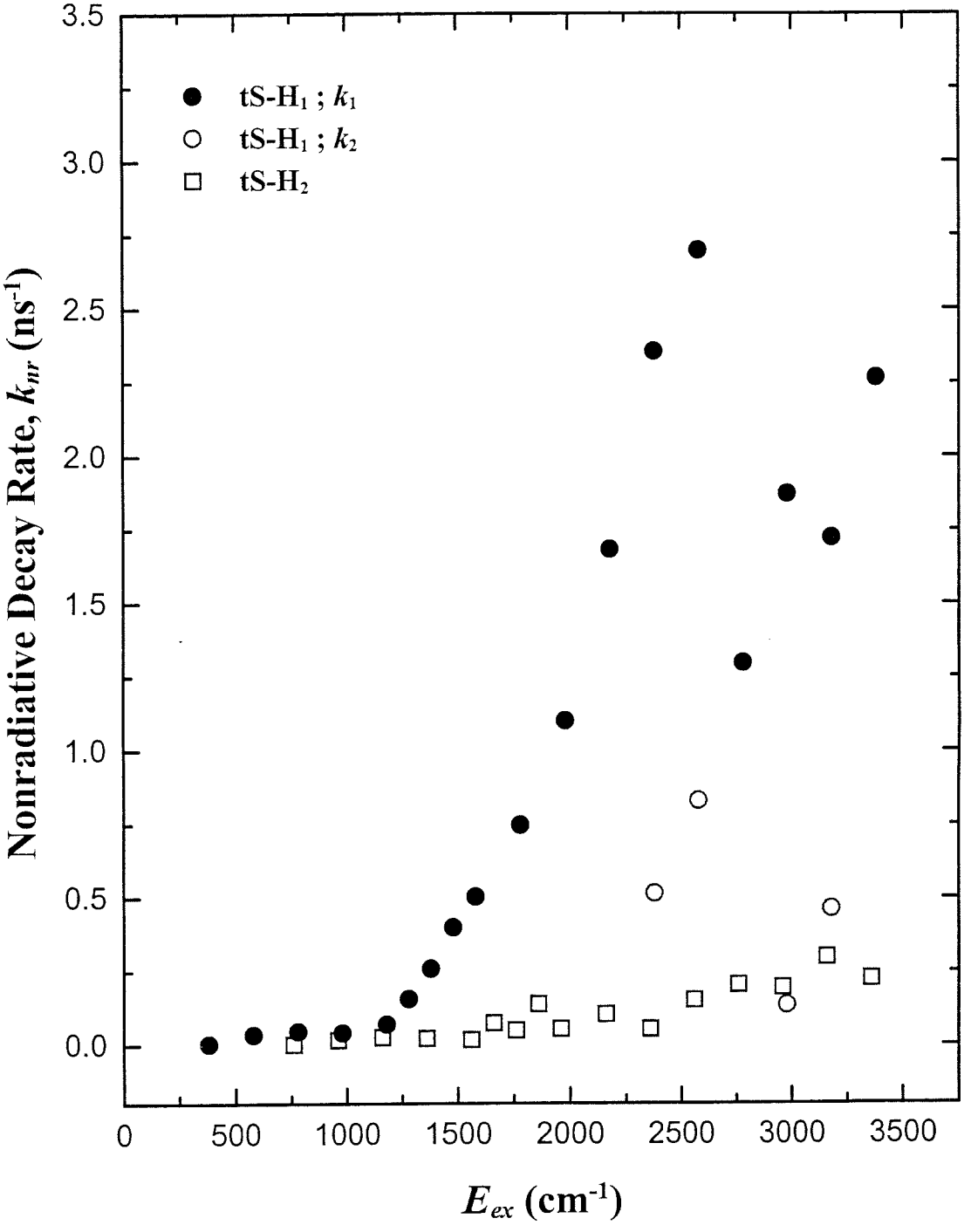
tS-H1 ; k1
tS-H1 ; k2
tS-H2
Nonradiative Decay Rate, knr (ns-1)
Eex (cm-1)
0.0
0.5
1.0
1.5
2.0
2.5
3.0
3.5
0
500
1000
1500
2000
2500
3000
3500

Figure 9

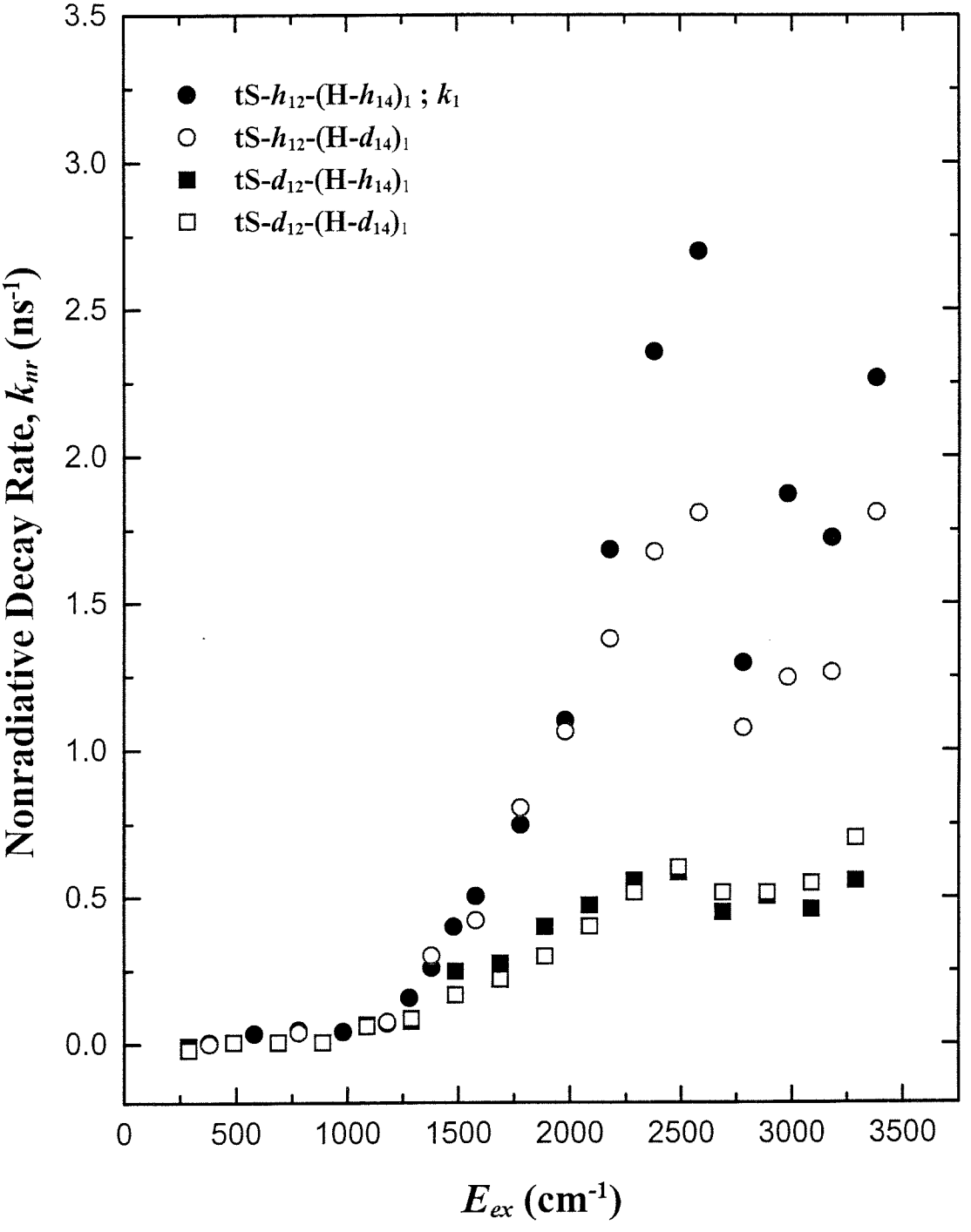
tS-h_{12}-(H-h_{14})$_1$; k_1
tS-h_{12}-(H-d_{14})$_1$
tS-d_{12}-(H-h_{14})$_1$
tS-d_{12}-(H-d_{14})$_1$
Nonradiative Decay Rate, k_{nr} (ns^{-1})
E_{ex} (cm^{-1})
0.0
0.5
1.0
1.5
2.0
2.5
3.0
3.5
0
500
1000
1500
2000
2500
3000
3500

Figure 10

Table 1: Excess Energy Dependent Results for Bare tS-h_{12}

E_{ex} (cm^{-1})	τ (ns)	k (ns^{-1})	Ave. k (ns^{-1})
0	2.73, 2.57	0.366, 0.389	0.378
400	2.47, 2.57	0.405, 0.389	0.397
600	2.67, 2.70	0.374, 0.370	0.372
800	2.80, 2.73, 3.00, 2.63	0.357, 0.366, 0.333, 0.380	0.359
900	2.50	0.400	0.400
1000	2.40	0.417	0.417
1100	2.03, 2.03	0.493, 0.493	0.493
1200	2.11	0.474	0.474
1400	1.35	0.741	0.741
1600	0.90	1.11	1.11
1800	0.60	1.67	1.67
2000	0.36, 0.41	2.78, 2.46	2.62
2200	0.280	3.57	3.57
2400	0.233	4.29	4.29
2600	0.187, 0.192	5.35, 5.21	5.28
2800	0.145	6.90	6.90
3000	0.115	8.70	8.70

Table 1

Table 2: Excess Energy Dependent Results for tS-h_{12}-(H-h_{14})$_1$

E_{ex} (cm^{-1})	τ_1 (ns)	k_1 (ns^{-1})	Ave. k_1 (ns^{-1})	τ_2 (ns)	k_2 (ns^{-1})	Ave. k_2 (ns^{-1})	$\frac{a_2}{a_1}$
380	2.63	0.380	0.374	—	—	—	—
	2.60	0.385		—	—		
	2.80	0.357		—	—		
580	2.47	0.405	0.405	—	—	—	—
780	2.40	0.417	0.417	—	—	—	—
980	2.43	0.412	0.412	—	—	—	—
1180	2.27	0.440	0.440	—	—	—	—
1280	1.90	0.526	0.526	—	—	—	—
1380	1.47	0.680	0.629	—	—	—	—
	1.73	0.578		—	—		
1480	1.30	0.769	0.769	—	—	—	—
1580	1.23	0.813	0.874	—	—	—	—
	1.07	0.935		—	—		
1780	0.967	1.03	1.12	—	—	—	—
	0.833	1.20		—	—		
1980	0.680	1.47	1.47	—	—	—	—
2180	0.487	2.05	2.05	—	—	—	—
2380	0.367	2.72	2.72	1.13	0.885	0.885	0.31
2580	0.340	2.94	3.07	0.800	1.25	1.20	0.25
	0.313	3.19		0.867	1.15		0.40
2780	0.587	1.70	1.67	—	—	—	
	0.613	1.63		—	—		
2980	0.427	2.34	2.24	2.20	0.455	0.505	0.35
	0.467	2.14		1.80	0.556		0.22

3180	0.433 0.533	2.31 1.88	2.09	1.20 —	0.833 —	0.833	0.18 —
3380	0.367 0.393	2.72 2.54	2.63	—	—	—	—

Table 2

Table 3: Excess Energy Dependent Results for tS-h_{12} Control (for tS-H_1)

E_{ex} (cm^{-1})	τ (ns)	k (ns^{-1})	Ave. k (ns^{-1})
0	2.53	0.395	0.395
200	2.73	0.366	0.366
400	2.47	0.405	0.405
600	2.80	0.357	0.357
800	2.60	0.385	0.385
900	2.47	0.405	0.405
1000	2.27 2.33	0.441 0.429	0.435
1100	1.97	0.508	0.508
1200	1.57	0.637	0.637
1400	1.07	0.935	0.935
2200	0.263	3.80	3.80
2600	0.170	5.88	5.88
3000	0.106	9.434	9.43

Table 3

Table 4: Excess Energy Dependent Results for tS-h_{12}-(H-h_{14})$_2$

E_{ex} (cm^{-1})	τ (ns)	k (ns^{-1})	Ave. k (ns^{-1})
760	2.87 3.13	0.348 0.319	0.334
960	2.87 2.87	0.348 0.348	0.348
1160	2.80	0.357	0.357
1360	2.83	0.353	0.353
1560	2.87	0.348	0.348
1660	2.47	0.405	0.405
1760	2.63	0.380	0.380
1860	2.13	0.469	0.469
1960	2.60	0.385	0.385
2160	2.30	0.435	0.435
2360	2.60	0.385	0.385
2560	2.07	0.483	0.483
2760	1.87	0.535	0.535
2960	1.90	0.526	0.526
3160	1.59	0.629	0.629
3360	1.80	0.556	0.556

Table 4

Table 5: Excess Energy Dependent Results for tS-O_1

E_{ex} (cm^{-1})	τ_1 (ns)	k_1 (ns^{-1})	τ_2 (ns)	k_2 (ns^{-1})	$\frac{a_2}{a_1}$
307	2.87	0.348	—	—	—
507	2.67	0.375	—	—	—
707	2.73	0.366	—	—	—
907	2.47	0.405	—	—	—
1107	2.23	0.448	—	—	—
1307	2.10	0.476	—	—	—
1507	1.90	0.526	—	—	—
1707	1.63	0.613	—	—	—
1907	1.43	0.699	—	—	—
2107	1.00	1.00	3.07	0.326	0.40
2307	0.800	1.25	2.67	0.375	0.43
2507	0.727	1.38	2.33	0.429	0.13
2707	0.653	1.53	2.13	0.469	0.05
2907	0.520	1.92	2.33	0.429	0.035
3107	0.400	2.50	2.33	0.429	0.014
3307	0.347	2.88	2.13	0.469	0.018
3507	0.320	3.12	2.13	0.469	0.26
3707	0.347	2.88	2.07	0.483	0.29

Table 5

Table 6: Excess Energy Dependent Results of tS-h_{12} Control (for tS-O_2)

E_{ex} (cm^{-1})	τ_1 (ns)	k_1 (ns^{-1})	τ_2 (ns)	k_2 (ns^{-1})	$\frac{a_2}{a_1}$
200	2.73	0.366	—	—	—
400	2.67	0.375	—	—	—
1000	2.40	0.417	—	—	—
1400	1.30	0.769	—	—	—
1600	0.900	1.11	—	—	—
1800	0.720	1.39	—	—	—
2000	0.460	2.17	—	—	—
2400	0.24	4.17	2.67	0.375	0.08
2600	0.187	5.348	2.67	0.375	0.06
2800	0.147	6.803	—	—	—
3200	0.107	9.346	—	—	—

Table 6

Table 7: Excess Energy Dependent Results of tS-O_2

E_{ex} (cm^{-1})	τ (ns)	k (ns^{-1})
1013	2.73	0.366
1413	2.73	0.366
1813	2.60	0.385
2413	2.67	0.375
2613	2.73	0.366
2813	2.53	0.395
3213	2.40	0.417
3413	2.27	0.441
3613	2.07	0.483
3813	2.13	0.469
4013	1.97	0.508

Table 7

Table 8: Excess Energy Dependent Results for tS-h_{12}-(H-d_{14})$_1$

E_{ex} (cm^{-1})	τ_1 (ns)	k_1 (ns^{-1})	Ave. k_1 (ns^{-1})	τ_2 (ns)	k_2 (ns^{-1})	Ave. k_2 (ns^{-1})	$\frac{a_2}{a_1}$
380	2.73	0.366	0.366	—	—	—	—
780	2.47	0.405	0.405	—	—	—	—
1180	2.27	0.441	0.441	—	—	—	—
1380	1.50	0.667	0.667	—	—	—	—
1580	1.27	0.787	0.787	—	—	—	—
1780	0.853	1.17	1.17	—	—	—	—
1980	0.700	1.43	1.43	—	—	—	—
2180	0.573	1.75	1.75	—	—	—	—
2380	0.533, 0.453	1.88, 2.21	2.04	— 2.53	— 0.395	0.395	0.12
2580	0.460	2.17	2.17	2.20	0.455	0.455	0.13
2780	0.700, 0.687	1.43, 1.46	1.44	—	—	—	—
2980	0.620	1.61	1.61	—	—	—	—
3180	0.613	1.63	1.63	—	—	—	—
3380	0.460	2.17	2.17	—	—	—	—

Table 8

Table 9: Excess Energy Dependent Results for tS-h_{12} Control (for tS-h_{12}-(H-d_{14})$_1$)

E_{ex} (cm^{-1})	τ (ns)	k (ns^{-1})
0	2.83	0.353
400	2.87	0.348
800	2.57	0.389
1000	2.43	0.412
1200	1.90	0.526
1400	0.853	1.17
1600	0.833	1.20
1800	0.607	1.65
2000	0.420	2.38
2200	0.273	3.663
2400	0.227	4.40

Table 9

Table 10: Excess Energy Dependent Results for tS-d_{12}-(H-h_{14})$_1$

E_{ex} (cm^{-1})	τ (ns)	k (ns^{-1})
287	2.90	0.345
687	2.80	0.357
1087	2.40	0.417
1287	2.33	0.429
1487	1.67	0.599
1687	1.60	0.625
1887	1.33	0.752
2087	1.21	0.824
2287	1.10	0.909
2487	1.07	0.937
2687	1.25	0.802
2887	1.17	0.857
3087	1.23	0.811
3287	1.10	0.909

Table 11: Excess Energy Dependent Results for tS-d_{12} Control (for tS-d_{12}-(H-h_{14})$_1$)

E_{ex} (cm^{-1})	τ (ns)	k (ns^{-1})
307	2.80	0.357
707	2.40	0.417
1107	2.20	0.454
1507	1.50	0.667
1907	0.767	1.30
2307	0.480	2.08
2907	0.253	3.95

Table 11

Table 12: Excess Energy Dependent Results for tS-d_{12}-(H-d_{14})$_1$

E_{ex} (cm^{-1})	τ (ns)	k (ns^{-1})
287	2.87	0.348
487	2.67	0.374
687	2.67	0.374
887	2.67	0.374
1087	2.33	0.429
1287	2.20	0.454
1487	1.87	0.535
1687	1.70	0.588
1887	1.50	0.667
2087	1.30	0.769
2287	1.13	0.885
2487	1.03	0.971
2687	1.13	0.885
2887	1.13	0.885
3087	1.09	0.917
3287	0.933	1.072

Table 12

Table 13: Excess Energy Dependent Results for tS-d_{12} Control (for tS-d_{12}-(H-d_{14})$_1$)

E_{ex} (cm^{-1})	τ (ns)	k (ns^{-1})
107	2.53	0.395
307	2.67	0.374
507	2.60	0.385
707	2.67	0.374
907	2.50	0.400
1107	2.13	0.470
1307	1.80	0.556
1507	1.57	0.637
1707	1.06	0.943
1907	0.76	1.32
2107	0.56	1.79
2307	0.367, 0.333 (bare)	2.72, 3.00 (bare)
2507	0.353	2.83
2707	0.267	3.75
2907	0.240	4.17

Table 13

Table 14: *trans*-Stilbene-h_{12} S_1 State Vibrational Frequencies (in cm^{-1}), Adapted from Ref. 5, Used in the RRKM Calculations

41	54	97	132	229	239	284	305
403	407	454	475	542	583	619	629
646	662	698	716	735	757	814	818
832	843	903	910	910	1018	1021	1024
1025	1025	1033	1034	1034	1082	1086	1151
1152	1166	1171	1217	1270	1294	1334	1335
1349	1396	1397	1452	1483	1488	1494	1519
1521	1545	1562	1632	3077	3085	3087	3088
3088	3088	3089	3090	3091	3092	3093	3095

Table 15: *trans*-Stilbene-h_{12} Non-Adiabatic Transition State Frequencies (in cm^{-1}), Adapted from Ref. 5, Used in the RRKM Calculations

53	67	84	168	187	305	316	383
396	416	473	535	563	620	621	640
656	665	692	737	749	810	821	841
854	867	911	939	1013	1017	1022	1027
1030	1035	1047	1064	1077	1089	1144	1155
1161	1164	1170	1238	1244	1314	1322	1361
1383	1396	1429	1481	1491	1502	1506	1517
1528	1546	1553	3080	3086	3087	3088	3088
3089	3089	3090	3090	3090	3092	3092	i552

Table 14 and 15

Table 16: *trans*-Stilbene-d_{12} S_1 State Vibrational Frequencies (in cm^{-1}), Adapted from Ref. 5, Used in the RRKM Calculations

38	50	90	123	219	220	243	287
361	365	401	427	501	521	521	567
575	600	620	634	638	639	647	656
670	735	737	759	775	811	811	821
821	821	822	829	829	844	845	860
870	983	989	996	1033	1075	1087	1180
1261	1309	1312	1324	1375	1395	1413	1467
1476	1490	1527	1605	2272	2274	2277	2277
2278	2279	2282	2283	2285	2286	2291	2292

Table 17: *trans*-Stilbene-d_{12} Non-Adiabatic Transition State Frequencies (in cm^{-1}), Adapted from Ref. 5, Used in the RRKM Calculations

49	62	77	157	174	279	286	354
360	373	420	485	514	522	537	561
602	612	630	640	641	657	666	708
735	758	763	776	801	816	822	822
828	829	830	834	843	846	853	858
942	971	986	1005	1067	1087	1163	1269
1297	1304	1318	1379	1392	1427	1451	1473
1487	1507	1517	2269	2273	2276	2277	2278
2278	2282	2283	2285	2286	2291	2291	i418

Table 18: *n-Hexane-h_{14}* Normal Mode Frequencies Calculated with DFT Methods

78	99	130	147	239	249	286	353
449	706	719	780	859	875	875	977
978	1015	1032	1039	1118	1165	1208	1226
1262	1282	1287	1293	1343	1358	1370	1371
1437	1438	1445	1453	1454	1454	1462	1466
2889	2893	2903	2908	2914	2917	2918	2925
2942	2956	2987	2988	2992	2992		

Table 19: *n-Hexane-d_{14}* Normal Mode Frequencies Calculated with DFT Methods

66	80	113	122	174	184	249	317
386	512	528	580	650	690	699	709
816	835	850	869	916	944	955	967
969	986	1001	1034	1049	1050	1052	1052
1061	1076	1082	1102	1109	1136	1194	1225
2103	2104	2111	2111	2121	2123	2169	2177
2190	2199	2219	2220	2224	2224		

Table 20: *n-Octane-h_{18}* Normal Mode Frequencies Calculated with DFT Methods

55	76	103	122	142	166	191	254
256	265	328	453	456	703	707	726
776	848	861	876	928	972	980	1000
1018	1029	1031	1063	1116	1163	1192	1205
1236	1256	1272	1280	1291	1292	1304	1341
1361	1361	1369	1370	1435	1436	1439	1443
1450	1455	1455	1457	1463	1467	2889	2889
2892	2899	2906	2909	2913	2916	2919	2919
2925	2937	2947	2957	2984	2984	2991	2991

Table 21: Intermolecular Cluster Mode Frequencies (in cm^{-1}) Calculated with Molecular Mechanics Employing DREIDING Forcefield

tS-h_{12}-H_1-h_{14}	14	20	35	65	77	95
tS-h_{12}-H_2-h_{14}	11	18	26	40	45	51
	56	65	70	77	84	101
tS-h_{12}-H_1-d_{14}	13	19	35	61	75	80
tS-h_{12}-H_2-d_{14}	10	17	25	37	42	47
	51	59	67	72	77	87
tS-h_{12}-O_1-h_{18}	12	20	33	67	72	82
tS-h_{12}-O_2-h_{18}	11	19	24	39	44	46
	56	63	69	74	76	80
tS-d_{12}-H_1-h_{14}	14	20	33	63	74	91
tS-d_{12}-H_2-h_{14}	10	18	26	38	45	51
	54	63	68	74	83	95
tS-d_{12}-H_1-d_{14}	13	19	32	59	72	79
tS-d_{12}-H_2-d_{14}	10	17	24	36	41	47
	50	57	65	70	75	85

Chapter 4

Discussion

4.1. Preliminaries. Fig. 1 of chapter 1, reproduced from Ref. 20, shows a representative minimum energy structure of tS-H_3 calculated by Lennard-Jones atom-atom potentials. The lowest energy structures of tS-H_2 and of tS-H_1 calculated by this method are represented, respectively, by the pictured structure without the single hexane above the tS plane and without the two hexanes below the plane. For tS-H_1, the most stable conformation in the ground state has a binding energy based on molecular mechanics calculation of ~ 2300 cm^{-1}. The binding energies will be higher in the excited states, however, as indicated by the red shift of the cluster excitation spectrum. For the lowest energy isomer of tS-H_2, the first dissociation energy is calculated to be ~ 2400 cm^{-1}. No estimates of the binding energies of the cluster ions are available.

The calculated geometry shown in Fig. 1 reveals a strong *wetting* of the solute surface by the solvent molecules, which suggests a strong coupling between the solvent vibrational and intermolecular cluster modes with the stilbene modes. This strong coupling was confirmed experimentally in a previous study [1], which found that dissipative IVR in tS-H_1 occurred at an excess vibrational energy of ~ 300 cm^{-1} in the S_1 state, much lower than the corresponding value of ~ 1200 cm^{-1} in tS. Based on this low energy for dissipative IVR in tS-H_1, IVR is not expected to limit the isomerization rate for any of the tS alkane clusters we investigated, since isomerization barriers are at least a few hundred wavenumbers above the start of dissipative IVR. Thus, as for tS, one may apply statistical theories to model the isomerization rate for tS alkane clusters.

The main challenge to interpreting our data is to understand the role of vibrational predissociation (vp) of the clusters. As indicated by the calculated binding energies, we expect the clusters at some point in the excess energy range shown in Fig. 7 of chapter 3 to be sufficiently energized that they fragment. The opening up of a vp channel has a possible consequence that the vp rate itself contributes to the measured rate and/or that a transient measured at the TOF position corresponding to the mass of one cluster reflects dynamics of a cluster of a larger mass. To understand how different ion sources affect the rates measured in the $k_{nr}(E_{ex})$ vs. E_{ex} studies, a kinetic scheme will be presented in Sec. 4.2 to examine the effects of various possible kinetic processes taking place at the S_1 and the ion state.

4.2. Kinetic Scheme. In order to understand the experimental results presented in the last section, it is necessary to develop a kinetic scheme which details the kinetics of the prominent processes taking place at the excited and the ion states of tS alkane clusters. The three processes that are considered most likely to affect the time evolution of the population of a cluster after the pump, and subsequently the probe excitations, are: fluorescence, isomerization and vibrational predissociation. The functional form of the measured transient, such as the total decay rate and the amplitude, depends greatly on the contributions of each of these three processes.

Fig. 1 is a diagram depicting how, in our pump-probe TOF mass detection measurements, the three different processes could contribute to the signal from the detection of a generic ion cluster A-B_n^+. In this scheme, k_r, k_{iso} and k_{vp} are the rate constants for fluorescence, isomerization and vibrational predissociation respectively,

while $k_{vp,ion}$ is the rate constant corresponding to the vibrational predissociation at the ion state. The terms E_{ex} and $E_{ex,ion}$ represent the excess energy above the vibrationless level in S_1 and the ion state, while D_{0,S_1} and $D_{0,ion}$ denote the first dissociation energy of a cluster at the first excited state and the ion state. A superscript is placed on all rates and energies to indicate the number of solvent molecules in the cluster to which they correspond. In all applications in this paper, k_r is assumed to be independent of excess energy.

(a) General Description. Judging by the calculated binding energies and considering the range of excess energies studied, we restrict consideration in this section to loss of at most one solvent molecule through vp. Under this condition, in the most general case, when A-B_n^+ is detected, the ion signal could have arisen from three sources. The first, and the most obvious, is ionization of A-$B_n^*(E_{ex}^n)$, which is formed directly from the pump excitation of ground state A-B_n. The second is ionization of A-$B_n^*(E_{ex}^{n+1} - D_{0,S_1}^{n+1})$, which is produced from the predissociation of A-$B_{n+1}^*(E_{ex}^{n+1})$ at the S_1 state. Since in our studies, the difference between E_{ex}^n and E_{ex}^{n+1} is much smaller (~ 500 cm^{-1} or less) than D_{0,S_1}^{n+1} (~ 2300 cm^{-1} or higher), the internal vibrational energy of A-$B_n^*(E_{ex}^{n+1} - D_{0,S_1}^{n+1})$ is lower than that of A-$B_n^*(E_{ex}^n)$ by the positive quantity $\Delta E_{ex}^n = E_{ex}^n - (E_{ex}^{n+1} - D_{0,S_1}^{n+1})$. Hence, A-$B_n^*(E_{ex}^{n+1} - D_{0,S_1}^{n+1})$ can also be denoted as A-$B_n^*(E_{ex}^n - \Delta E_{ex}^n)$. The third source is predissociation of A-$B_{n+1}^+(E_{ex,ion}^{n+1})$ at the ion state,

producing an ion with internal energy equal to $E_{ex,ion}^{n+1} - D_{0,ion}^{n+1}$. As shown in Fig. 1, these three sources will be termed source #1, source #2 and source #3.

(b) Vibrational Predissociation (vp) at the Ion State. A crucial aspect in the interpretation of our data is to understand how, for a given cluster, the kinetics of vp at the ion state manifests itself through the time distribution of its fragments in the TOF mass spectra. When a population of a specific cluster ion, for example A-B_{n+1}^+, is created by a pump-probe sequence, the initial size of this population is a direct sampling of the A-B_{n+1}^* population, which in turn reflects the excited state dynamics which precede the probe pulse. However, if these ions have significant vibrational energy, they may undergo vp before they can be accelerated, mass selected, and detected. The effect of this vp will result in the initial A-B_{n+1}^+ population producing a TOF distribution of A-B_n^+ ions spread out between the TOF positions of intact A-B_{n+1}^+ and A-B_n^+, a distribution which depends on the relation between $1/k_{vp,ion}^{n+1}$ and the flight time of the ion in the potential field region of the TOF tube (acceleration time) [2]. $k_{vp,ion}^{n+1}$ will depend on the internal energy of the A-B_{n+1}^+ ions and the acceleration time is fixed by the mass and TOF assembly design.

To see how the TOF signal of the A-$B_n^+(E_{ex,ion}^{n+1} - D_{0,ion}^{n+1})$ fragments produced from vp of A-$B_{n+1}^+(E_{ex,ion}^{n+1})$ (ion source #3) would distribute, let us examine several scenarios. Firstly, if the vp lifetime of A-$B_{n+1}^+(E_{ex,ion}^{n+1})$, $\tau_{vp,ion}^{n+1} = 1/\ k_{vp,ion}^{n+1}$, is very long compared to the acceleration time, then almost all of the A-$B_{n+1}^+(E_{ex,ion}^{n+1})$ population would still remain

intact upon entering the field-free region. Fragments produced thereafter (assuming small translational kinetic energy release in the vp) would continue at the same speed as, and arrive at the detector at the same time as, intact A-B_{n+1}^+ ions. Secondly, if the lifetime of the predissociation is very short, then virtually all A-$B_{n+1}^+(E_{ex.ion}^{n+1})$ ions would predissociate to form A-$B_n^+(E_{ex.ion}^{n+1} - D_{0.ion}^{n+1})$ before they had acquired any velocity in the accelerating field, and virtually all ion signals would appear at the TOF position of A-B_n. Thus, in each of the above two cases, one detection-response limited TOF peak would be registered, at the TOF position of A-B_{n+1} in the first case and A-B_n in the second. Thirdly, if the lifetime of the vp is of the same order as the acceleration time, which is typically around 1 μs, then a time distribution of fragment population spanning the TOF positions of A-B_n and A-B_{n+1} will be observed. The characteristics of the fragment distribution, however, is dependent on Δt, which is the TOF difference between A-B_n and A-B_{n+1}. Δt can be calculated from the design parameters of the TOF apparatus. For a nascent A-B_n^+ cluster which is produced from the vp of A-B_{n+1}^+ at time t_{diss} after ionization, the time of flight difference between the nascent and the intact A-B_n^+ cluster can be approximated by the following equation for small t_{diss}:

$$\Delta t \cong \left[1 - \left(\frac{M_1}{M_2}\right)\right] \cdot t_{diss} + \frac{1}{2} \cdot \left(\frac{M_1^{\,2} - M_1 \cdot M_2}{M_2^{\,2}}\right) \cdot \left(\frac{q \cdot V_{OC}}{2 \cdot M_1 \cdot S_{OC}^{\,2}}\right)^{\frac{1}{2}} \cdot \left[1 - \left(\frac{1}{2} \cdot \frac{S_{CM}}{S_{OC}}\right)\right] \cdot t_{diss}^{\,2} \qquad (4.1)$$

where M_1 and M_2 are the mass of A-B_n^+ and A-B_{n+1}^+ respectively. The definition of terms, and the detail expression of Δt, can be found in appendix I.

In order to illustrate the time distribution of the nascent cluster population in the third scenario mentioned above, simulations for tS-H_2^+ vp based on the design of our TOF assembly were performed. By assuming the $\tau_{vp,ion}^{n=2}$ of tS-H_2 to be equal to the calculated flight time of the ion cluster in the potential field region (1.28 μs), and that no tS-H_1 was present initially, a time distribution profile of the intact tS-H_2 and the nascent tS-H_1 was obtained. The result is shown in Fig. 2, and it can be seen that a tail extending from the TOF position of tS-H_1 is clearly visible. Those tS-H_2 ions that have not dissociated before exiting the accelerating field (in this case, a fraction $1/e$ = 0.368 of the whole population) are all detected at the TOF position of tS-H_2. For shorter $\tau_{vp,ion}^{n=2}$, the distribution contracts toward the tS-H_1 peak. The TOF assembly parameters used in the simulation are given in part (d) of appendix I.

In the TOF mass spectra of our experiments, which have a detection response of ~ 20-40 ns (FWHM), no clear broadening of any mass spectral peak was observed for any clusters at any excess energy. This fact indicates that $\tau_{vp,ion}$ is in either the long or the short limit for each cluster measurement. As we have seen, if $\tau_{vp,ion}$ is always much longer than ~ 1 μs, the S_1 population dynamics of a given cluster could always be monitored at its original mass (ion source #1), and the measured rate of that contribution should increase monotonically with energy, in clear contradiction to the observed abrupt drop-off in the measured rate of tS-H_1. Therefore, source #1 must disappear at the drop-

off, which only happens for dissociation *of the ion*, tS-H_1^+, with $\tau_{vp,ion}^{n=1}$ much shorter than 1 μs at that pump-probe energy. Given that larger clusters are excited to higher S_1 energies at the same wavelength, and under reasonable assumptions (see Sec. 4.3), larger cluster ions must also dissociate at energies above the tS-H_1 drop-off, giving rise to source #3 ion signals at each TOF mass peak. In that case, the absence of detectable tails on the TOF peaks is only compatible with $\tau_{vp,ion}$ being much shorter than the t_{diss} which corresponds to a Δt of ~30 ns (the TOF peak width). This limiting value of the vp lifetime is calculated from Eq. 4.1 to be < ~75 ns, which is consistent with current knowledge of the time scales of van der Waals complex dissociation dynamics. Hence, we conclude that, at the higher energies studied, vp does occur in the ion state of each A-B_{n+1}, and when it does, all of the ion signal, reflecting A-B_{n+1}^* dynamics, is detected at the intact A-B_n^+ TOF position.

The drop-off for tS-H_1 seen in Fig. 9 of chapter 3 at E_{ex} ~ 2580 cm^{-1} allows one to estimate the value of $D_{0,S_1}^{n=1}$ for tS-H_1. Since it has been explained that the drop-off has to come from vp of tS-H_1^+, we can deduce that at E_{ex} ~ 2580 cm^{-1}, the probe pulse has promoted tS-H_1^+ into the ionization potential of tS, as indicated in Fig. 3. As shown in Fig. 3, the same pump pulse which excited tS-H_1 (S_0) into tS-H_1^* (S_1) with E_{ex} ~ 2580 cm^{-1}, would excite tS (S_0) into tS * (S_1) with E_{ex} ~ 2200 cm^{-1}. The same probe pulse which subsequently promoted tS-H_1^* (S_1) into the ion state and caused vp of tS-H_1^+, would carry tS * (S_1) into the ion state, ~ 3530 cm^{-1} above the ionization threshold (when pump pulse with energy equal to the 0-0 transition of tS was used, the probe pulse, which

energy was fixed at all time, would promote the vibrationless tS * (S_1) into the ion state, ~ 1330 cm^{-1} above the ionization threshold). Hence, from Fig. 3, the following relationship is apparent: E_{probe} + 2580 cm^{-1} = E_{probe} – (2200 cm^{-1} + 1330 cm^{-1}) + 2200 cm^{-1} + $D_{0,S_1}^{n=1}$, and $D_{0,S_1}^{n=1}$, the cluster binding energy of tS-H_1 at the S_1 state, is easily determined to be ~ 3910 cm^{-1}. Along the same line of reasoning, the binding energy of tS-O_1 at the S_1 state is determined to be ~ 4840 cm^{-1}, assuming that the drop-off occurred at E_{ex} ~ 3510 cm^{-1}. The binding energies of tS-H_1 and tS-O_1 at the ground state are simply equal to ($D_{0,S_1}^{n=1}$ – red shift), which are ~ 3530 cm^{-1} and ~ 4330 cm^{-1} respectively. Based on molecular mechanics calculations, the first dissociation energies of tS-H_2 and tS-O_2 were found to be about the same as that of their 1:1 counterparts. Hence, in the absence of experimental values, we assumed the first dissociation energies of tS-H_2 and tS-O_2 at the S_1 state to be ~ 3910 cm^{-1} and ~ 4840 cm^{-1} respectively.

(c) Contributions to the Transient Signal. In the following, explicit equations for ion sources #1, #2, and #3 are given. For generality, we will allow for any value of $\tau_{vp,ion}$, although in our experiments only the two limits apply: either no vp in the ion or "fast" vp in the ion.

The signal due to source #1, $I_1(t)$, can be written as follows:

$$\begin{aligned} I_1(t) &= [\mathrm{A}\text{-}\mathrm{B}_n^{+}(E_{ex,ion}^{n})]_{t'=0} \cdot [1-\beta(E_{ex,ion}^{n})] \\ &= \sigma_{probe} \cdot [\mathrm{A}\text{-}\mathrm{B}_n^{*}(E_{ex}^{n})] \cdot [1-\beta(E_{ex,ion}^{n})] \end{aligned} \qquad (4.2)$$

where the term σ_{probe} is the ionization probability, and the bracketed expressions are populations which are implicitly dependent on the pump-probe time delay, t, when not labeled with a subscript indicating evaluation at a specific value of t. The term $[\text{A-B}_n^{+}(E^n_{ex,ion})]_{t'=0}$ represents the initial population of ions at the point of ionization, and $\beta(E^n_{ex,ion})$, which is excess energy dependant, denotes the fraction of $\text{A-B}_n^{+}(E^n_{ex,ion})$ population that undergoes vp to form $\text{A-B}_{n-1}^{+}(E^n_{ex,ion} - D^n_{0,ion})$ before the ions exit the potential field. This is simply given by $\beta = (\tau_{vp,ion})^{-1} \int_0^{t_{OC}} e^{-\frac{t_{OC}}{\tau_{vp,ion}}} dt = (1 - e^{-\frac{t_{OC}}{\tau_{vp,ion}}})$. Note that vp in the ion state only affects the amplitude but not the kinetics of the transient measured.

The explicit time dependence of source #1 can be derived trivially from the rate equation for $[\text{A-B}_n^{*}(E^n_{ex})]$:

$$\frac{d[\text{A-B}_n^{*}(E^n_{ex})]}{dt} = -[k^n_r + k^n_{iso}(E^n_{ex}) + k^n_{vp}(E^n_{ex})] \cdot [\text{A-B}_n^{*}(E^n_{ex})] \qquad (4.3)$$

giving

$$I_1(t) = \sigma_{probe} \cdot [\text{A-B}_n^{*}(E^n_{ex})]_0 \cdot \exp[-k^n_{Total}(E^n_{ex})t] \cdot [1-\beta(E^n_{ex,ion})] \qquad (4.4)$$

where $k^n_{Total}(E^n_{ex}) = k^n_r + k^n_{iso}(E^n_{ex}) + k^n_{vp}(E^n_{ex})$.

Whenever A-$B_{n+1}^{*}(E_{ex}^{n+1})$ is present, source #2 must be taken into account. In this case an A-B_n^{+} signal may come from ionization of A-$B_n^{*}(E_{ex}^{n}-\Delta E_{ex}^{n})$. The signal due to source #2, $I_2(t)$, can be written as follows (see appendix II for complete derivation):

$$\begin{aligned} I_2(t) &= [\text{A-B}_n^{+}(E_{ex,ion}^{n}-\Delta E_{ex}^{n})]_{t'=0}\cdot[1-\beta(E_{ex,ion}^{n}-\Delta E_{ex}^{n})] \\ &= \sigma'_{probe}\cdot[\text{A-B}_n^{*}(E_{ex}^{n}-\Delta E_{ex}^{n})]\cdot[1-\beta(E_{ex,ion}^{n}-\Delta E_{ex}^{n})] \end{aligned} \tag{4.5}$$

$$\begin{aligned} I_2(t) = \sigma'_{probe}\cdot\Bigg\{ & \frac{k_{vp}^{n+1}(E_{ex}^{n+1})[\text{A-B}_{n+1}^{*}(E_{ex}^{n+1})]_0}{k_{Total}^{n}(E_{ex}^{n}-\Delta E_{ex}^{n})-k_{Total}^{n+1}(E_{ex}^{n+1})} \\ & \cdot\{\exp[-k_{Total}^{n+1}(E_{ex}^{n+1})]t-\exp[-k_{Total}^{n}(E_{ex}^{n}-\Delta E_{ex}^{n})\,t]\}\Bigg\} \\ & \cdot[1-\beta(E_{ex,ion}^{n}-\Delta E_{ex}^{n})] \end{aligned} \tag{4.6}$$

where β is the same function as before and σ'_{probe} is the ionization probability of A-$B_n^{*}(E_{ex}^{n}-\Delta E_{ex}^{n})$. Note that this source first rises then decays with pump-probe delay.

If the signal from the vp of A-$B_{n+1}^{+}(E_{ex,ion}^{n+1})$ is also contributing (ion source #3), then another signal component which is related to the kinetics of A-$B_{n+1}^{*}(E_{ex}^{n+1})$ would also be observed. The signal derived from this source would depend on the fraction of A-$B_n^{+}(E_{ex,ion}^{n+1}-D_{0,ion}^{n+1})$ fragments, produced via the vp of A-$B_{n+1}^{+}(E_{ex,ion}^{n+1})$, that fall within the boxcar gate. Let $\alpha'(E_{ex,ion}^{n+1})$ be that fraction, which is always less than or equal to $\beta'(E_{ex,ion}^{n+1})$, where $\beta'(E_{ex,ion}^{n+1})$ is the fraction of A-$B_{n+1}^{+}(E_{ex,ion}^{n+1})$ population that undergoes vp before the ions exit the potential field. (The functions β and β' differ because the

acceleration time is mass dependent.) Then, the ion signal attributed to source #3 can be written as (see appendix for complete derivation)

$$\begin{aligned} I_3(t) &= [\text{A-B}_{n+1}{}^{+}(E_{ex,ion}^{n+1})]_{t'=0} \cdot \alpha'(E_{ex,ion}^{n+1}) \\ &= \sigma''_{probe} \cdot [\text{A-B}_{n+1}{}^{*}(E_{ex}^{n+1})] \cdot \alpha'(E_{ex,ion}^{n+1}) \end{aligned} \tag{4.7}$$

$$I_3(t) = \sigma''_{probe} \cdot [\text{A-B}_{n+1}{}^{*}(E_{ex}^{n+1})]_0 \cdot \exp[-k_{Total}^{n+1}(E_{ex}^{n+1})\,t] \cdot \alpha'(E_{ex,ion}^{n+1}) \tag{4.8}$$

where σ''_{probe} is the ionization probability of A-$B_{n+1}{}^{*}(E_{ex}^{n+1})$.

As already discussed, there is a strong evidence in our results to suggest that whenever A-$B_{n+1}{}^{+}(E_{ex,ion}^{n+1})$ acquires enough energy to undergo vp, i.e., for $E_{ex,ion}^{n+1} > D_{0,ion}^{n+1}$, all of its A-$B_n{}^{+}(E_{ex,ion}^{n+1} - D_{0,ion}^{n+1})$ fragments are detected during transient measurements at the TOF mass peak of A-$B_n{}^{+}$. As a result, we have α' (as well as β') is either 0 or 1, and the signal contribution from source #3 can simply be written as

$$I_3(t) = \sigma''_{probe} \cdot [\text{A-B}_{n+1}{}^{*}(E_{ex}^{n+1})]_0 \cdot \exp[-k_{Total}^{n+1}(E_{ex}^{n+1})\,t] \cdot \Theta(E_{ex,ion}^{n+1} - D_{0,ion}^{n+1}) \tag{4.9}$$

where $\Theta(x)$, the Heavyside step function, is equal to 0 for $x < 0$ and 1 for $x > 0$.

The characteristics of a transient at a given excess energy depends on the interplay between $I_1(t)$, $I_2(t)$ and $I_3(t)$, which, in the most general case, may contribute three possible rates to the signal: $k_{Total}^{n}(E_{ex}^{n})$, $k_{Total}^{n}(E_{ex}^{n} - \Delta E_{ex}^{n})$ and $k_{Total}^{n+1}(E_{ex}^{n+1})$. In order to correctly interpret the transients we measured, it is crucial to determine which of these

three signals are being collected in our measurements, and, just as importantly, which process, isomerization or vp, is actually dominant in k_{Total}.

4.3. Isomerization vs. Evaporation. As indicated in Fig. 1, the time dependent characteristics of the signals depend greatly on the kinetics of the numerous processes taking place after the pump and the probe excitations. To understand their influences and to determine which one has a greater effect on the signal measured, two cases can be distinguished. In each, we assume, as previously argued, that once the vp channel at the ion state opens, vp is "fast" (faster than ~ (1/75) ns^{-1}, see Sec. 4.2).

Case I: vp at the S_1 state is much slower than isomerization, $k_{vp} << k_{iso}$. Under this scenario, with k_r of the same order of magnitude as $k_{iso}(E_{ex})$, $k_{Total}(E_{ex})$ is simply equal to $k_r + k_{iso}(E_{ex})$. The amplitude of ion source #2, which has $k_{vp}^{n+1}(E_{ex}^{n+1})$ as a factor, will in general be negligible. Thus the measured rates reflect directly: (1) the isomerization of A-$B_n^*(E_{ex}^n)$ at excitation energies up to the point that the vp channel at the A-B_n ion is reached, i.e., for $E_{ex,ion}^n < D_{0,ion}^n$; and/or (2) the isomerization of A-$B_{n+1}^*(E_{ex}^{n+1})$ at energies above the point that the vp channel at the A-B_{n+1} ion is reached, or $E_{ex,ion}^{n+1} > D_{0,ion}^{n+1}$. These energy thresholds for disappearance of source #1 and appearance of source #3 need not be equal.

Case II: vp at the S_1 state is not much slower than isomerization. This condition can only apply for excitation energies above D_{0,S_1}, the first dissociation energy of the

cluster at the S_1 state. At lower excitation energies, k_{vp} is zero, so case I is in effect. The difference here is that, for energies above D_{0,S_1}: (1) $k_{Total}(E_{ex}) = k_r + k_{iso}(E_{ex}) + k_{vp}(E_{ex})$ and therefore $k_{iso}(E_{ex})$ cannot be trivially extracted from the measured rates; and (2) source #2 becomes important. Since sources #1 and #3, although with rates now influenced by vp, continue to contribute just as in case I, the addition of the much more slowly decaying contribution of source #2, with rate $k^n_{Total}(E^n_{ex} - \Delta E^n_{ex})$, is the key distinguishing characteristic of case II. This gives rise to the possibility of triexponential transients, simultaneously displaying rates of three different origins, and of biexponential decay persisting to high energies. This is because the source #2 ions are detected until much higher energy than is the case for source #1 ions, as manifested in the equations for $I_1(t)$ and $I_2(t)$ by the fact that $\beta(E^n_{ex,ion} - \Delta E^n_{ex})$ remains ~ 0 at energies for which $\beta(E^n_{ex,ion})$ has become 1.

Since the first cluster dissociation energies for tS-H_n and tS-O_n (n = 1, 2) at the S_1 state are determined to be ~ 3910 cm^{-1} and ~ 4840 cm^{-1} respectively, which are beyond the upper limits of the E_{ex} available to all the clusters being studied, therefore, under ideal cooling condition, Case I is operative and source #2 is not expected to be a factor in our measurements. In our study of tS-A_n, if there is any signal contribution from tS-A_{n+1}, it is most likely to arise from vp at the ion state (source #3), since the clusters always have ~ 1330 cm^{-1} more internal energy at the ion state than at the S_1 state. In the above

argument, we assumed that the cluster binding energies at the ion state are about the same as that at the S_1 state.

Hence, in the $k_{nr}(E_{ex})$ vs. E_{ex} result of tS-H_1, in addition to the drop-off, a fast vp at the ion state can also account for the minor slow rate component observed at E_{ex} ~ 2380 cm^{-1} and ~ 2580 cm^{-1}. The slow rate component can be attributed to the detection of ion source #3, which is nascent tS-H_1^+ produced via vp of tS-H_2^+ at the ion state, and the rate reflects the total decay rate of tS-$H_2^*(E_{ex}^{n=2})$ at the S_1 state. Since the first vp energy of tS-H_2 at the ground state was expected to be roughly equal to that of tS-H_1 (based on prediction by molecular mechanics calculation), coupled with the fact that tS-H_2 will have a lower $S_1(v' = 0) \leftarrow S_0(v'' = 0)$ excitation energy relative to that for tS-H_1 due to the red shift, it is reasonable to conclude that vp of tS-H_2 at the S_1 state would take place at a lower pump excitation energy compared to that of tS-H_1, possibly ~ 380 cm^{-1} lower. If we assumed that $D^n_{0,ion} = D^n_{0,S_1}$, then, vp of tS-$H_2^+$ would likely take place at energy ~ 380 cm^{-1} lower than that of tS-H_1^+. Hence, when E_{ex} ~ 2380 cm^{-1} for tS-H_1 at the S_1 state, tS-H_1^+ would have been generated by the probe pulse with internal energy up to ~ 3710 cm^{-1} at the ion state (~ 2380 cm^{-1} + 1330 cm^{-1}). The same pump and probe pulses, however, would have produced tS-H_2^+ with internal energy up to ~ 4090 cm^{-1} (assuming the 0-0 excitation of tS-H_2 is red-shifted by ~ 380 cm^{-1} relative to that of tS-H_1), which is higher than the expected first dissociation energy of ~ 3910 cm^{-1} for tS-H_2^+. Hence, when measuring transients of tS-H_1 at E_{ex} ~ 2380 cm^{-1} and 2580 cm^{-1}, we were able to detect nascent tS-H_1^+ from vp of tS-H_2^+, even though the tS-H_1^+ produced from

direct excitation of tS-H_1^* remained intact. Likewise, the rates measured at $E_{ex} > \sim 2580$ cm^{-1} can be attributed to the same nascent signal source, and again the rate is related to the kinetics of tS-$H_2^*(E_{ex}^{n=2})$ at the S_1 state. So, according to case I, at $E_{ex} > \sim 2580$ cm^{-1}, even though the signal at the TOF position corresponding to tS-H_1 was gated, we were actually measuring the kinetics of tS-$H_2^*(E_{ex}^{n=2})$, instead of that of tS-$H_1^*(E_{ex}^{n=1})$.

What about the second component observed at $E_{ex} \sim 2980$ cm^{-1} and 3180 cm^{-1} on the $k_{nr}(E_{ex})$ vs. E_{ex} plot of tS-H_1? There are two possible scenarios for the observation of this long component: the first is that it arose from ion source #2; and the second is that it originated from the concerted vp of two hexane molecules (i.e., as a hexane dimer) from tS-H_3^+, which is a remotely possible scenario which we have not discussed until now. The above two energies correspond to tS-H_2^* excess energies of $\sim$ 3360 cm^{-1} and $\sim$ 3560 cm^{-1}, which are $\sim$ 580 cm^{-1} and $\sim$ 380 cm^{-1} less than the expected energy required for vp at the S_1 state. Hence, under unsatisfactory vibrational cooling of tS-H_2, the first scenario is possible. However, if vp of tS-H_2^* took place at $E_{ex} \sim 3360$ cm^{-1} and $\sim$ 3560 cm^{-1} to produce tS-$H_1^*(E_{ex}^{n=2} - D_0^{n=2})$, the rates of the long component measured at $E_{ex} \sim$ 2980 cm^{-1} and 3180 cm^{-1} in the excess energy dependence study of tS-H_1 should be $\sim$ 0.37 ns^{-1}, because after tS-H_2 at the S_1 state predissociated, the tS-$H_1^*(E_{ex}^{n=2} - D_0^{n=2})$ fragments produced do not have enough internal energy to undergo isomerization. Under optimal fittings, the slow components measured at the above two energies have rates of 0.51 ns^{-1} and 0.83 ns^{-1} respectively. However, acceptable biexponential fits of the

transients measured at E_{ex} ~ 2980 cm^{-1} and 3180 cm^{-1} can be obtained with the slow component fixed at ~ 0.37 ns^{-1}, albeit with higher χ^2 values.

Now, let's examine the second scenario. Based on molecular mechanics calculations, the energy requires to predissociate two hexane molecules simultaneously (the hexane dimer) from tS-H_3 is about 1.57 times the energy needed to separate hexane from tS in tS-H_1. Hence, for tS-H_3 at the S_1 state, we would expect the binding energy between the hexane dimer and tS-H_1 to be ~ 6140 cm^{-1}. Assuming that $D^n_{0,ion} = D^n_{0,S_1}$, the binding energy would also be ~ 6140 cm^{-1} at the ion state. When tS-H_1^* acquired excess vibrational energy of ~ 2980 cm^{-1}, the E_{ex} attained by tS-H_3^* would be ~ 3740 cm^{-1} (adding ~ 760 cm^{-1} for assumed red-shift), and subsequently, tS-H_3^+ would acquire up to ~ 5070 cm^{-1} of internal energy (~ 3740 cm^{-1} + ~ 1330 cm^{-1}), which is not enough to overcome the expected ~ 6140 cm^{-1} of binding energy at the ion state. As a result, we concluded it is highly unlikely that the simultaneous vp of two hexane molecules from tS-H_3^+ can account for the appearance of the long component at E_{ex} ~ 2980 cm^{-1} and 3180 cm^{-1} on the $k_{nr}(E_{ex})$ vs. E_{ex} plot of tS-H_1.

The interpretation of the result for tS-O_1 is similar to that of tS-H_1. The rate measured below E_{ex} ~ 700 cm^{-1} can be attributed purely to radiative decay, and the rate measured thereafter until E_{ex} ~ 3500 cm^{-1} can be attributed to a combination of radiative and nonradiative decay, which is due to photoisomerization. Although it was not very definitive based on its magnitude, the slight drop off observed after E_{ex} ~ 3510 cm^{-1} is

believed to have the same nature as the drop off observed for tS-H_1 after E_{ex} ~ 2580 cm^{-1}, that is, it is related to the vp of tS-O_1 at the ion state, whereby tS-O_1^+ has undergone vp from that point on to form tS^+ and octane. Under such premise, as shown earlier, first cluster dissociation energies for tS-O_n (n = 1, 2) at the S_1 state can be estimated to be ~ 4840 cm^{-1}. Notice that in Fig. 10, the plot for tS-O_1 exhibits biexponentiality from E_{ex} ~ 2100 cm^{-1} onward. As in the case of tS-H_1, the occurrence of biexponentiality is best explained by the detection of nascent tS-O_1^+ resulted from the vp of tS-O_2^+. At E_{ex} ~ 2100 cm^{-1} for tS-O_1^*, tS-O_2^* would acquire ~ 2610 cm^{-1} of excess energy, and tS-O_2^+ would acquire internal energy up to ~ 3940 cm^{-1}, if we assume that $D^n_{0,ion} = D^n_{0,S_1}$. With internal energy only up to ~ 3940 cm^{-1}, tS-O_2^+ is ~ 900 cm^{-1} short in energy to overcome the first cluster binding energy. At the same excitation energy, the internal energy of tS-O_2^* is still ~ 2230 cm^{-1} shy of the expected first cluster dissociation energy, making the influence of ion source #2 very unlikely, at least until the highest excitation energies. In either case, the appearance of biexponential decays must be interpreted as demonstrating poor cooling of the tS-O_2 clusters. For this reason, we must consider the tS-O_2 results with caution.

In this section we have established that the measured rates can be assigned to isomerization, either of the cluster of the measured mass, or of the next larger cluster. The rates therefore can be associated with the proper species and proper excess vibrational energy to be compared to theory. This is done in the following section. Here, we have also established that the dissociation energy of tS-H_1 in the S_1 state is ~ 3910

cm^{-1}, and therefore that the corresponding value in S_0 is ~ 3530 cm^{-1}. Our data also give information about $D_{0,ion}^{n=1}$ and $D_{0,S_1}^{n=2}$, the first dissociation energy of tS-H_2 in the S_1 state, based on the appearance of source #3 of tS-H_1^+, but these are not independent and are also more uncertain. (For example, if source #3 first appears for a tS-H_1 excitation energy of 2380 cm^{-1} when $D_{0,S_1}^{n=1}$ = 2580 cm^{-1}, then it can be shown that $D_{0,S_1}^{n=2} = D_{0,ion}^{n=1} + (0\text{–}0_{n=1} - 0\text{–}0_{n=2}) - (2580 - 2380)$ cm^{-1}, or in this case $D_{0,S_1}^{n=2} = D_{0,ion}^{n=1} + 180$ cm^{-1}.) For tS-O_1, the dissociation energy at the S_1 and S_0 state are determined to be ~ 4840 cm^{-1} and ~ 4330 cm^{-1} respectively. All the binding energies mentioned above are ~ 50% higher than those calculated by molecular mechanics method, employing DREIDING forcefield. Nonetheless, note that one calculation performed on tS-H_1 with the Universal forcefield yielded a ground state cluster binding energy of ~ 4000 cm^{-1}, demonstrating that the experimental value falls within the range of variation in forcefield calculations. Even though these calculations are shown not to be very accurate in predicting the exact values of the dissociation energies, we believe that calculations are acceptable for estimating relative differences. Therefore, we use the calculated percentage difference as a guide in estimating the dissociation energy of the hexane dimer from tS-H_3.

Our measured rates of tS-H_1 isomerization up to ~ 2580 cm^{-1}, as shown in Fig. 9 of chapter 3, can be compared with the rates that were assigned to this process in Ref. 3, as extracted from multiexponential fluorescence decays. Those rates range in general between the values we have measured and about a factor of two faster, but show a great deal of scatter, particularly in the energy range 1000-1500 cm^{-1}.

4.4. Isomerization Rates: Experiment vs. Theory. Through kinetic scheme analysis, we have extracted from our measurements the excess energy dependence of the isomerization rates, $k_{iso}(E_{ex})$, for a number of tS-alkane$_n$ clusters (where n = 1 and 2). In this section, we will compare these results with several different theoretical treatments, from which analysis we hope to understand the nature of microscopic friction, and the effects of finite solvation on the isomerization reaction.

We have spoken earlier of two types of microscopic friction: *energy friction* and *motional friction*. Energy friction refers to the slowing of the isomerization rate due to the flow of energy from the reaction coordinate to the solvent heat bath. In the limit where microscopic friction is purely due to energy friction, a form of RRKM theory, such as the nonadiabatic RRKM model, should be able to predict the isomerization rate well. (The Kramers-type model for motional friction in clusters will be considered below.) Standard RRKM calculation of reaction rates utilizes the following expression [6]:

$$k(E_{ex}) = \sigma \cdot \frac{N^{\dagger}(E_{ex}-E_0)}{h\,\rho(E_{ex})} = \sigma \cdot \frac{\int_0^{E_{ex}-E_0} \rho^{\dagger}(E_v^{\dagger})\,dE_v^{\dagger}}{h\,\rho(E_{ex})} \qquad (4.10)$$

where E_{ex} is the excess vibrational energy at the reactant state, $E_v^{\dagger}$ is the excess vibrational energy at the transition state, E_0 is the reaction barrier, $\rho(E_{ex})$ and $\rho^{\dagger}(E_v^{\dagger})$ are the densities of vibrational states of the reactant state at E_{ex} and the transition state at $E_v^{\dagger}$, $N^{\dagger}(E_{ex}-E_0)$ is the sum of vibrational states in the transition state with energy less than or equal to $E_{ex}-E_0$, and h is Planck's constant. In the calculations, the clusters

were treated as a "macromolecule" and all of the vibrational modes, including the solvent vibrational modes, were assumed to have equal access for energy flow.

The term σ is included to take into account the degeneracy of the reaction [4,5,6], which in the case of tS equals to 2 because isomerization can proceed in either of the two equivalent directions of rotation about the central ethylene bond. In the case of tS-A_1, σ is assumed to be ~ 1 because the isomerization coordinate is no longer symmetric, due to the fact that isomerization in the direction facing the solvent molecule is hindered. For tS-A_2, however, since there are two prominent types of isomers — one with two alkanes on one side (2+0) of tS and the other with one alkane on each side (1+1) — there is no simple way to assign a σ value. In their analysis of tS-H_2, Gershinsky and Pollak [7] had argued that the formation of the 1+1 isomer is more favorable because of an entropic factor. As a result, σ should be 2 because the isomerization process is symmetric. However, their analysis assumed that tS-H_2 was produced via tS-H_1 + hexane only. The other highly probable reaction channel which would lead only to the formation of the 2+0 isomer, tS + $hexane_2$, was ignored. When both reaction channels are taken into consideration, it is difficult to argue whether one isomer would be produced in favor over the other. In our nonadiabatic RRKM analysis (Sec. 4.4 (b)), we analyzed our tS-A_2 results at both extreme cases, where we assumed that the cluster population consists of purely (2+0) or (1+1) isomer by setting σ = 1 or 2.

In the following, we will examine the theoretical rates predicted by the standard RRKM model as implemented by Gershinsky and Pollak, and by the nonadiabatic RRKM model of Felker and Zewail [10]. In both models, the clusters were treated as

"macromolecules" and all of the vibrational modes, including the solvent vibrational modes, are assumed to have equal access for energy flow.

(a) Gershinsky and Pollak (G&P) Treatment. Eq. (4.10) was utilized to calculate the microcanonical rate in the G&P treatment. The normal mode frequencies of tS were calculated from the empirical potential developed by Vachev *et al.* [8], and the hexane vibrational modes and the intermolecular cluster modes were calculated from exp-6 pair potentials of Dillen [9]. An aspect considered by Gershinsky and Pollak is that the degeneracy factor, σ, for tS isomerization is 2, not 1, as assumed by others in the past. And the degeneracy factor varies from cluster to cluster. In cases where the isomerization symmetry is broken, two inequivalent isomerization barriers were considered. The theoretical microcanonical RRKM rates of Gershinsky and Pollak [7] are shown in Fig. 4, plotted against our experimental results. As can be seen, even though their calculated rates agree qualitatively with the experimental data, the quantitative agreement is not satisfactory, especially for the case of tS-H_1. Note that in Fig. 8 of chapter 3, we have shown that our bare tS data matches very well quantitatively with that obtained from the literature [10]. This supports the conclusion that the standard RRKM method does not give a good quantitative account of the experimental microcanonical rate (*vide infra*). As a result, use of a modified RRKM model to explain the microcanonical rate of tS and tS *n*-alkane clusters is indicated.

(b) Felker and Zewail Nonadiabatic Model. In the nonadiabatic model [10], Eq. (4.10) is modified to take into account the Landau-Zener curve-crossing probability, P, giving the following expression:

$$k(E_{ex}) = \sigma \cdot \frac{\int_0^{E_{ex}-E_0} (1-P)\,\rho^{\dagger}(E_v^{\dagger})\,dE_v^{\dagger}}{h\,\rho(E_{ex})} \tag{4.11}$$

where

$$P = \exp\left(-\frac{\pi\gamma}{2\hbar\upsilon}\right) \tag{4.12}$$

In this case, υ is the velocity along the reaction coordinate at the transition state and $\gamma = \Delta^2 / |F_1 - F_n|$, where Δ is the splitting between the two energy surfaces at the avoided crossing, and F_1 and F_n are the slopes of the two curves intersecting at the avoided crossing.

The reason why the nonadiabatic model of Felker and Zewail was chosen over the adiabatic model of Troe for the analysis of tS *n*-alkane cluster work was simple: although Negri and Orlandi [11] had verified that both the models could predict the microcanonical rate for tS isomerization well with *unbiased* frequencies obtained quantum chemically, a further analysis of the work of Negri and Orlandi revealed that the adiabatic model actually overestimates the microcanonical rate by a factor of 2. The reason for this is that Orlandi and Negri neglected the degeneracy factor $\sigma = 2$, stated in Eq. (4.10). If the appropriate degeneracy factor was included, the adiabatic RRKM rate would be twice as high and would not fit the experimental data well. In contrast, the nonadiabatic model could still predict the experimental rate by varying the probability, P, in Eq. (4.11).

It has been shown in other publications [10,11] that nonadiabatic RRKM theories can account for the microcanonical rates of tS-h_{12} and tS-d_{12} very well. The nonadiabatic

RRKM fitting parameters for the two isotopic molecules obtained in our experiments are shown in Table 1, where E_0 and I_{red} are the barrier height and the reduced moment of inertia of the molecules. Note that the E_0 for tS-d_{12} is fixed to that of tS-h_{12}, with correction for the differences in zero point energies. Even though a better fit for tS-d_{12} can be obtained with a barrier height of 1200 cm^{-1}, to be consistent with the vibrational frequencies used in the rate calculation, we chose to take into account the theoretical change in the barrier height. I_{red} of tS at the S_1 state was determined based on the structure calculated by Warshel [12], modified to be consistent with the rotational coherence measurements [13]. As can be seen, the γ value resulting from the tS-d_{12} fit with predetermined E_0 and I_{red} is higher than that obtained from the tS-h_{12} fit, consistent with the findings by Negri and Orlandi [11]. However, the value of γ we obtained for both tS-h_{12} and tS-d_{12} are only about half the values determined by Negri and Orlandi, due to our use of $\sigma = 2$ rather than 1.

To test the applicability of nonadiabatic RRKM theory in accounting for the microcanonical rates of tS *n*-alkane clusters, we first performed fittings on the rates of tS-h_{12}-(H-h_{14})$_1$ and tS-h_{12}-(H-d_{14})$_1$ to determine if the rates can be predicted with a common set of fitting variables. Since the two clusters share the same parent molecule and have identical electronic potentials, it is reasonable to expect that their rates could be predicted with the same E_0, γ and I_{red}. Prior to the fit, the vibrational frequencies and I_{red} can be predetermined; the value for E_0 and γ can then be extracted from the fit. The methods for obtaining the frequencies are discussed in chapter 2, Sec. 2.5, and the

value of I_{red} for the clusters was taken to be the same as that of tS-h_{12}. We base this assumption on the fact that isomerization of tS in tS-H_1 is favored in the direction away from the hexane molecule. Therefore, the twisting need not accelerate the solvent molecule and the kinetic energy of motion along the reaction coordinate resides principally in the tS phenyl rings. It was found that by setting I_{red} = 263 amu Å^2 (which is the tS-h_{12} moment of inertia), it was possible to obtain very good fits for tS-h_{12}-(H-h_{14})$_1$ and tS-h_{12}-(H-d_{14})$_1$ with the same E_0 and γ values, which are 630 cm^{-1} and 0.14 cm^{-1} rad respectively. The fittings are shown in Fig. 5-6. To further test the applicability of nonadiabatic RRKM theory in predicting the tS isomerization rate in clusters, the E_0 and γ values extracted from the fits of the tS-h_{12}-(H-h_{14})$_1$ and tS-h_{12}-(H-d_{14})$_1$ measurements were used to predict the microcanonical rates of tS-d_{12}-(H-h_{14})$_1$ and tS-d_{12}-(H-d_{14})$_1$. For the latter two clusters, the barrier height used in the calculation was set 90 cm^{-1} higher at 720 cm^{-1}, taking into account the difference in the barrier height between tS-h_{12} and tS-d_{12}; I_{red} was set at 290 amu Å^2 for the moment of inertia of tS-d_{12}. By keeping γ the same as that in the tS-h_{12}-H_1 clusters, and simply applying the appropriate set of calculated vibrational frequencies, it was found that the nonadiabatic theory predicts the isomerization rates of tS-d_{12}-(H-h_{14})$_1$ and tS-d_{12}-(H-d_{14})$_1$ fairly well. The results are shown in Fig. 7-8.

As mentioned in chapter 3, tS-h_{12}-(H-d_{14})$_1$, tS-d_{12}-(H-h_{14})$_1$ and tS-d_{12}-(H-d_{14})$_1$ were added to our studies to examine the effects of energy friction on the rate of isomerization. However, RRKM calculations, performed after the experiments were

completed, indicate that the change in the measured rates due to deuteration of the solvent molecules should be minor, falling into the range of uncertainty of our measurements. Since our experimental results do not show much deviation in the rates between tS-h_{12}-(H-h_{14})$_1$ and tS-h_{12}-(H-d_{14})$_1$, and between tS-d_{12}-(H-h_{14})$_1$ and tS-d_{12}-(H-d_{14})$_1$, the only conclusion which can be made thus far regarding the effects of solvent vibrational density of states is that the effects are consistent with RRKM theory.

Note that in Fig. 5-8, the nonadiabatic RRKM rates for the corresponding 1:2 clusters are shown as well. In the case of tS-h_{12}-(H-h_{14})$_2$ and tS-d_{12}-(H-d_{14})$_2$, the nonadiabatic RRKM rates were predicted by simply replacing the vibrational frequencies of the corresponding 1:1 species with that of the 1:2 species, without altering the values of E_0, γ and I_{red}. The rates for tS-h_{12}-(H-d_{14})$_2$ and tS-d_{12}-(H-h_{14})$_2$ were calculated with similar method, except the γ value had to be adjusted slightly to obtain satisfactory fit. The observation that the decrease in the rate of the tS-H_2 species can simply be predicted by replacing the vibrational frequencies of the 1:1 complexes with that of the corresponding 1:2 complexes implies two things. Firstly, the constancy of the barrier height seems most compatible with a tS-H_2 (2:0) structure, since a (1:1) structure would necessarily result in a very different perturbation to the reaction coordinate. This implies that, possibly, tS-A_2 clusters consist of mainly 2+0 (σ = 1) rather than 1+1 (σ = 2) isomer, as suggested by Gershinsky and Pollak. This implication is consistent with the computational results which show that the majority of the lowest energy tS-H_2 conformers have two of the *n*-hexane molecules on the same side of tS. Our finding was supported by other experimental and theoretical cluster studies [14,15] which show that

2+0 isomers can be the dominant species despite a less favorable entropic factor. Secondly, the increase in the microscopic friction of the 1:2 species relative to the corresponding 1:1 species can be entirely attributed to *energy friction*. Nonetheless, we will compare our results in the next section with the *motional friction* model of Marcus, to determine if a different explanation may also be applicable.

(c) Kramers-type Model. In the scenario where the slow down of tS isomerization rate in clusters can be attributed, at least in part, to motional friction, Marcus formulated an expression involving both the standard RRKM and Kramers' theories to account for the rate decrease [18]. In the model, the canonical Kramers' description is modified so as to apply to microcanonical systems. Marcus considered two cases: (a) the slow down of tS isomerization rate in clusters is purely attributed to motional friction, and (b) in addition to motional friction, both energy friction and barrier modification may also contribute to the rate decrease. In both of the above cases, the final expression describing the isomerization rate of tS in clusters is given as follows:

$$k = \left(\frac{1}{\omega'}\right)\left[\sqrt{\left(\frac{1}{2}\zeta\right)^2 + \omega'^2} - \frac{1}{2}\zeta\right] k_{RRKM} \qquad (4.13)$$

where in case (a), k_{RRKM} is equal to the microcanonical rate of the parent molecule, and in case (b), it is equal to the RRKM rate calculated for the cluster. The term ω' is the frequency of the barrier maximum (the harmonic frequency associated with the inverted barrier) and ζ is the frictional coefficient. ζ can be estimated to be:

$$\zeta \approx \gamma v_c n_c \qquad (4.14)$$

where ν_c (= $1/\tau_c$) is the "frequency" of the impacts between the solute and a single solvent molecule in the coordination shell, n_c is the number of solvent molecules in the shell and α is a variable which satisfies $0 < \alpha \leq 1$. The above expression for ζ assumes each solvent molecule in the inner shell to have the same frictional effect regardless of its position with respect to the solute molecule. Eq. (4.13) reduces to the standard RRKM rate equation if ζ is much smaller than $2\omega'$. In this limit, the time between solute-solvent impacts is much longer than the time of "free motion" through the barrier region and the frictional forces are considered to be a small perturbation on the motion along the reaction coordinate. On the other hand, if $\zeta / 2\omega' >> 1$, Eq. (4.13) becomes

$$k = \left(\frac{\omega'}{\zeta}\right) k_{RRKM} \tag{4.15}$$

In this case of strong friction, τ_c is short compared with the characteristic time scale of the free motion along the reaction coordinate.

One problem that is encountered, however, when Eq. (4.13) and (4.15) are to be applied to model tS isomerization rate in clusters according to case (a) is that the standard RRKM rate on the right-hand-side (RHS) of the equations, k_{RRKM}, does not predict the isomerization rate of the bare tS molecule. Since (as discussed earlier) the nonadiabatic model is the most successful at fitting the isomerization rate of bare tS when the reaction degeneracy (σ) is taken into account, we replaced k_{RRKM} in the equations with the nonadiabatic rate, $k_{NADRRKM}$. To be consistent, we do the same in case (b). After substitution and rearrangement, Eq. (4.13) can be written as follows:

$$k = \left[\sqrt{\left(\frac{1}{2} \frac{\zeta}{\omega'} \right)^2 + 1} - \frac{1}{2} \frac{\zeta}{\omega'} \right] k_{NADRRKM} \qquad (4.16).$$

As can be seen, once the scaling coefficient on the RHS of Eq. (4.16) is known, we can obtain the ζ / ω' ratio for both case (a) and (b). (Although independent values of ζ and ω' are not determined, ζ could be estimated from translational or rotational friction coefficients in solution [16,17].) In case (b), $k_{NADRRKM}$ for a cluster species was calculated by treating the cluster as a macromolecule whereby all vibrational modes of the cluster are taken into account. The nonadiabatic parameters used for each species are the same as those found in Table 1.

Let us first consider case (a). A relevant outcome of this assumption is that the rate of the clusters scales with the rate of the bare parent molecule, as indicated by Eq. (4.16), since the $k_{NADRRKM}$ term is a fixed function (equal to the rate of bare parent molecule). The case (a) theoretical fits to tS-h_{12}-(H-h_{14})$_n$, tS-d_{12}-(H-h_{14})$_n$ and tS-h_{12}-(O-h_{18})$_n$ experimental results are shown in Fig. 9-11 for illustration. The scaling factors and the ζ / ω' ratios obtained from all the clusters studied are listed in Table 2. Several points can be noted from these results. Firstly, comparison of tS-h_{12}-(H-h_{14})$_1$ and tS-d_{12}-(H-h_{14})$_1$ reveals that the ζ / ω' ratio for the latter (2.2) is almost twice as high as that of the former (1.3). This trend is not what we expected. Since the two clusters share the same solvent molecule, they should have the same ζ, because the *motional friction* exerted on the parent molecules by the solvent should be the same. In addition, ω' should be very similar since the two clusters have identical electronic potentials and only a small

difference in inertial effect in the reaction coordinate, as seen from the reduced moments of inertia given in Table 1. As a result, their ζ/ω' values would not be expected to differ by a factor of almost 2. Similar differences in the ζ/ω' ratio are also observed when comparing values between tS-h_{12}-(H-h_{14})$_2$ and tS-d_{12}-(H-h_{14})$_2$ (6.5 vs. 11). However, the ratios for two other pairs of clusters with identical solvation: tS-h_{12}-(H-d_{14})$_1$ and tS-d_{12}-(H-d_{14})$_1$ (1.8 vs. 2.7), and tS-h_{12}-(H-d_{14})$_2$ and tS-d_{12}-(H-d_{14})$_2$ (7.9 vs. 9.9), do fall closer to our expectation.

The discrepancies in the ζ/ω' ratios for the first two comparable pairs of clusters mentioned above can be explained by the data having large uncertainty. However, there are inconsistencies in Table 2 that are more difficult to reconcile: the ζ/ω' ratios for all the tS hexane 1:2 complexes were found to be ~ 4-5 times higher than those of the corresponding 1:1 complexes, whereas the model prediction is a factor of 2, according to Eq. (4.14). Finally, the ζ/ω' ratio for tS-O_1 was found to be ~ 3 times higher than that of tS-h_{12}-(H-h_{14})$_1$, which again, is difficult to reconcile with the very similar nature of the two solvents. That ζ/ω' of tS-O_2 is ~ 30 times higher than that of tS-O_1 is also in conflict with the theoretical prediction.

The scaling factors and ζ/ω' ratios obtained from case (b) are given in Table 3. Fig. 12-14 illustrate some of the fitting results. As will be discussed, these numbers are more reasonable than those obtained in case (a). For instance, only the ζ/ω' ratios of one pair of comparable clusters, that is, tS-h_{12}-(H-h_{14})$_2$ and tS-d_{12}-(H-h_{14})$_2$ (2.5 vs. 5.4), deviate significantly from the expected equality. The differences in the ζ/ω' ratios for

the remaining three pairs of clusters, tS-h_{12}-(H-h_{14})$_1$ and tS-d_{12}-(H-h_{14})$_1$ (2.5 vs. 3.4), tS-h_{12}-(H-d_{14})$_1$ and tS-d_{12}-(H-d_{14})$_1$ (2.5 vs. 3.4), and tS-h_{12}-(H-d_{14})$_2$ and tS-d_{12}-(H-d_{14})$_2$ (3.4 vs. 3.4), lie within the range of expected variability.

Case (b) treatment provides other more satisfactory results relative to the case (a) treatment. The ζ/ω' ratios obtained from the scaling for all the tS hexane 1:2 complexes were found to be ~ 1-1.6 times higher than that of the corresponding 1:1 complexes, which is closer to the model prediction of 2. Based on case (b) treatment, the discrepancy between the ζ/ω' ratio for tS-O_1 and tS-h_{12}-(H-h_{14})$_1$ was found to be smaller (different by a factor of ~ 1.8 vs. ~ 3.1 for that obtained in case (a)). The ζ/ω' for tS-O_2 is only ~ 7 times higher than that of tS-O_1, closer to the theoretical prediction of 2.

With the present data, it is clear that both of the motional friction treatments, case (a) and (b), can provide reasonably good quantitative fits to the experimental data. However, the fitting parameters obtained from the case (b) treatment are more satisfactory. This result is to be expected, in light of direct evidence of rapid exchange of energy between tS and hexane solvent molecules in the isolated clusters [1].

4.5. References

1. Lienau, Ch.; Heikal, A. A.; Zewail, A. H. *Chem. Phys.* **1993**, *175*, 171.

2. Proch, D.; Rider, D. M.; Zare, R. N. *Chem. Phys. Lett.* **1981**, *81*, 430.

3. Lienau, Ch.; Schroeder, J.; Troe, J.; Wack, K. *Ber. Bunsenges. Phys. Chem.* **1997**, *101*, 614.

4. Marcus, R. A. *J. Chem. Phys.* **1965**, *43*, 1598.

5. Pollak, E.; Pechukas, P. *J. Am. Chem. Soc.* **1978**, *100*, 2984.

6. Baer, T.; Hase W. *Unimolecular Reaction Dynamics: Theory and Experiments*; Oxford University Press: New York, 1996; p 205.

7. Gershinsky, G.; Pollak, E. *J. Chem. Phys.* **1997**, *107*, 10532.

8. Vachev, V. D.; Frederick J. H.; Grishanin, B. A.; Zadkov, V. N.; Koroteev, N. I. *J. Phys. Chem.* **1995**, *99*, 5247.

9. Dillen, J. L. *J. Comput. Chem.* **1995**, *16*, 595.

10. Felker, P. M.; Zewail, A. H. *J. Phys. Chem.* **1985**, *89*, 5402.

11. Negri, F.; Orlandi, G. *J. Phys. Chem.* **1991**, *95*, 748.

12. Warshel, A. *J. Chem. Phys.* **1975**, *62*, 214.

13. Baskin, J. S.; Zewail, A. H. *J. Phys. Chem.* **1989**, *93*, 5701.

14. Löhmannsröben, H.-G.; Bahatt, D.; Even, U. *J. Phys. Chem.* **1990**, *94*, 6286.

15. Ohline, S. M.; Romascan, J.; Felker, P. M. *J. Phys. Chem.* **1995**, *99*, 7311.

16. Sun, Y.-P.; Saltiel J. *J. Phys. Chem.* **1989**, *93*, 8310.

17. Bowman, R. M.; Eisenthal, K. B. *Chem. Phys. Lett.* **1989**, *155*, 99.

18. Marcus, R. A. *Chem. Phys. Lett.* **1995**, *244*, 10.

4.6. Figure Captions

Figure 1. A kinetic scheme which shows the three possible sources for A-B_n^+ ions. The rate constants for radiative decay, isomerization and vibrational predissociation (vp) at the S_1 state are represented by k_r, k_{iso} and k_{vp}, while $k_{vp,ion}$ denotes vp at the ion state. E_{ex} and $E_{ex,ion}$ represent the excess vibrational energy above the vibrationless state of the S_1 and the ion state. D_0 and $D_{0,ion}$ signify the first dissociation energy between the cluster and B at the S_1 and the ion state. The superscript of each symbol denotes the size of the cluster. $\Delta E_{ex}^n = E_{ex}^n - (E_{ex}^{n+1} - D_0^{n+1})$ represents the energy difference between two possible A-B_n^* species: one from direct excitation of A-B_n and the other from vp of A-B_{n+1}^* at the S_1 state.

Figure 2. Result for simulation of the time distribution of the nascent tS-H_1, produced via vp of tS-H_2, based on the design of our TOF assembly. In the simulation, we assumed that the vp lifetime of tS-H_2 in the ion state is equal to the flight time of the tS-H_2^+ ion in the potential field region (1.28 μs), and that no tS-H_1 was present initially.

Figure 3. Potential energy diagram illustrating the relations between the S_0, S_1 and S_{ion} vibrationless levels of tS and tS-H_1 (not to scale). The pump energy depicted is that corresponding to the observed break in the tS-H_1 $k_{nr}(E_{ex})$ vs. E_{ex} curve.

Figure 4. The theoretical microcanonical rates for tS-h_{12}-(H-h_{14})$_n$ (n = 0-3) isomerization, calculated with Gershinsky and Pollak harmonic RRKM model, plotted against our experimental data.

Figure 5. Experimental and theoretical microcanonical rates for tS-h_{12}-(H-h_{14})$_n$ (n = 1,2) isomerization based on nonadiabatic RRKM model.

Figure 6. Experimental and theoretical microcanonical rates for tS-h_{12}-(H-d_{14})$_n$ (n = 1,2) isomerization based on nonadiabatic RRKM model.

Figure 7. Experimental and theoretical microcanonical rates for tS-d_{12}-(H-h_{14})$_n$ (n = 1,2) isomerization based on nonadiabatic RRKM model.

Figure 8. Experimental and theoretical microcanonical rates for tS-d_{12}-(H-d_{14})$_n$ (n = 1,2) isomerization based on nonadiabatic RRKM model.

Figure 9. The tS-h_{12}-(H-h_{14})$_n$ (n = 0-3) experimental results and the theoretical fits based on the case (a) treatment of the Kramers-type model.

Figure 10. The tS-d_{12}-(H-h_{14})$_n$ (n = 0-2) experimental results and the theoretical fits based on the case (a) treatment of the Kramers-type model.

Figure 11. The tS-h_{12}-(O-h_{18})$_n$ (n = 0-2) experimental results and the theoretical fits based on the case (a) treatment of the Kramers-type model.

Figure 12. The tS-h_{12}-(H-h_{14})$_n$ (n = 1,2) experimental results and the theoretical fits based on the case (b) treatment of the Kramers-type model.

Figure 13. The tS-h_{12}-(H-d_{14})$_n$ (n = 1,2) experimental results and the theoretical fits based on the case (b) treatment of the Kramers-type model.

Figure 14. The tS-h_{12}-(O-h_{18})$_n$ (n = 1,2) experimental results and the theoretical fits based on the case (b) treatment of the Kramers-type model.

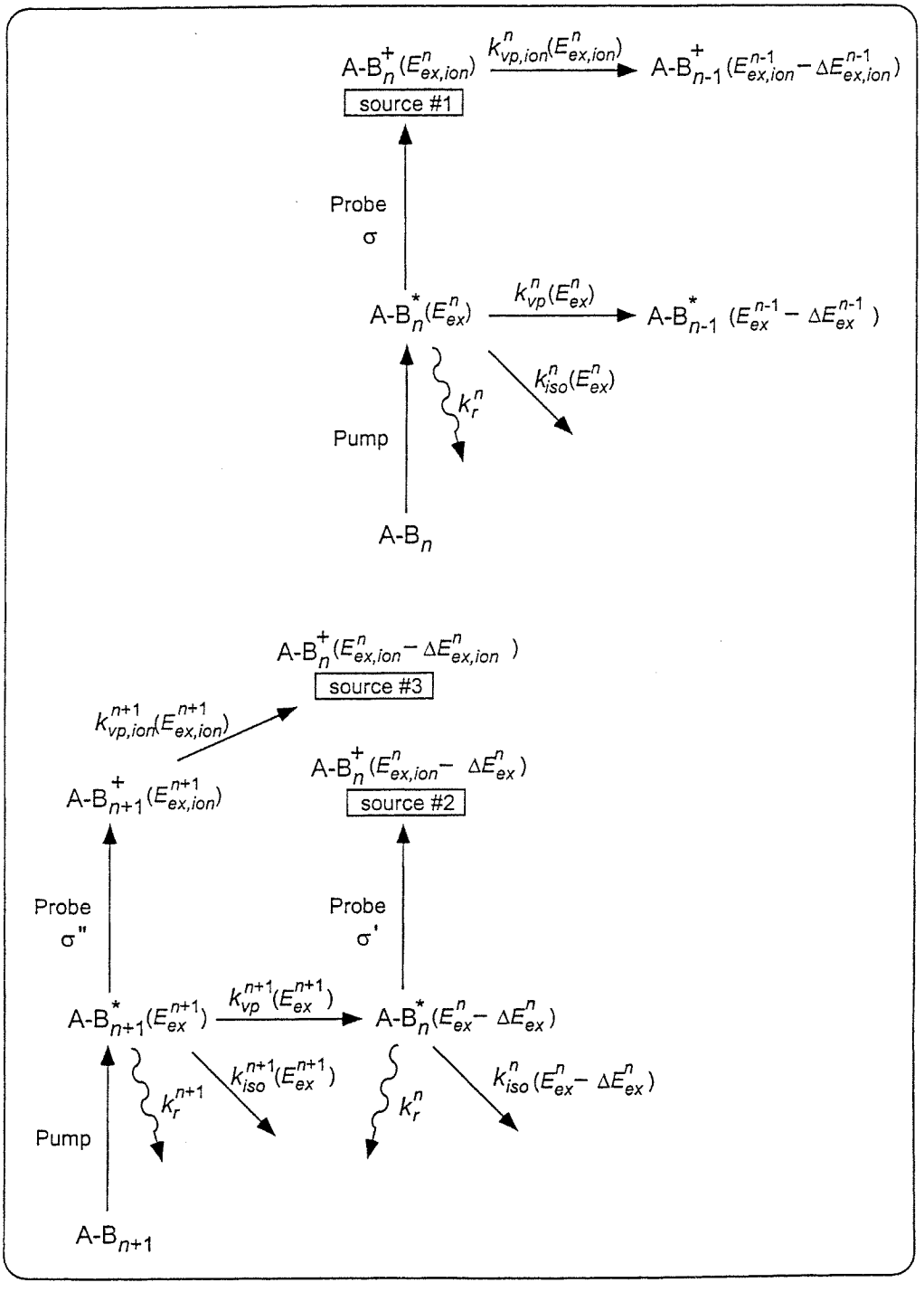
A-B$_n^+$($E_{ex,ion}^n$)
source #1
$k_{vp,ion}^n(E_{ex,ion}^n)$
A-B$_{n-1}^+$($E_{ex,ion}^{n-1} - \Delta E_{ex,ion}^{n-1}$)
Probe
σ
A-B$_n^*$(E_{ex}^n)
$k_{vp}^n(E_{ex}^n)$
A-B$_{n-1}^*$ ($E_{ex}^{n-1} - \Delta E_{ex}^{n-1}$)
$k_{iso}^n(E_{ex}^n)$
k_r^n
Pump
A-B$_n$
A-B$_n^+$($E_{ex,ion}^n - \Delta E_{ex,ion}^n$)
source #3
$k_{vp,ion}^{n+1}(E_{ex,ion}^{n+1})$
A-B$_n^+$($E_{ex,ion}^n - \Delta E_{ex}^n$)
source #2
A-B$_{n+1}^+$($E_{ex,ion}^{n+1}$)
Probe
σ"
Probe
σ'
A-B$_{n+1}^*$(E_{ex}^{n+1})
$k_{vp}^{n+1}(E_{ex}^{n+1})$
A-B$_n^*$($E_{ex}^n - \Delta E_{ex}^n$)
$k_{iso}^{n+1}(E_{ex}^{n+1})$
k_r^{n+1}
k_r^n
$k_{iso}^n(E_{ex}^n - \Delta E_{ex}^n)$
Pump
A-B$_{n+1}$

Figure 1

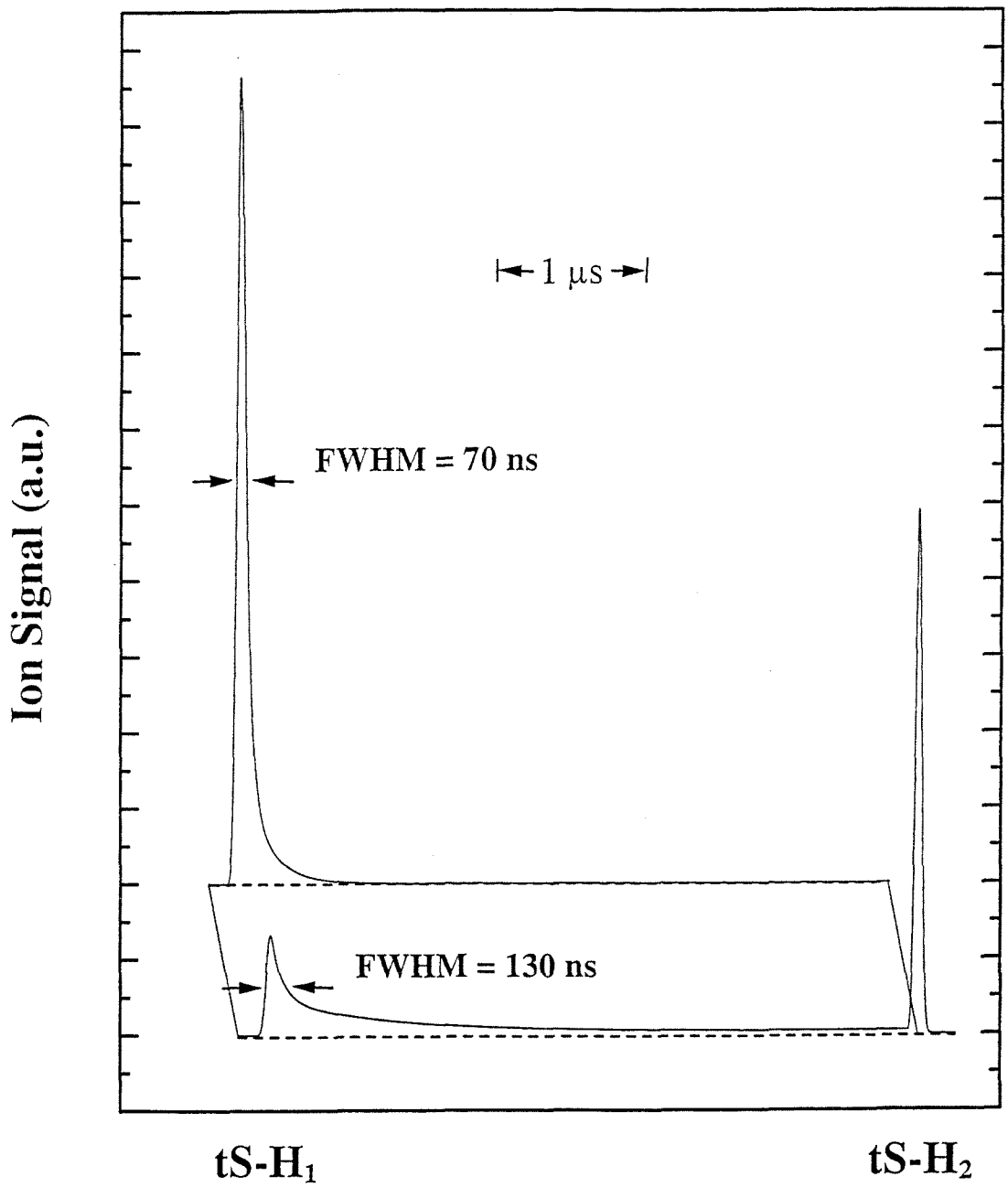
Ion Signal (a.u.)
1 μs
FWHM = 70 ns
FWHM = 130 ns
tS-H1
tS-H2
Relative TOF Position

Figure 2

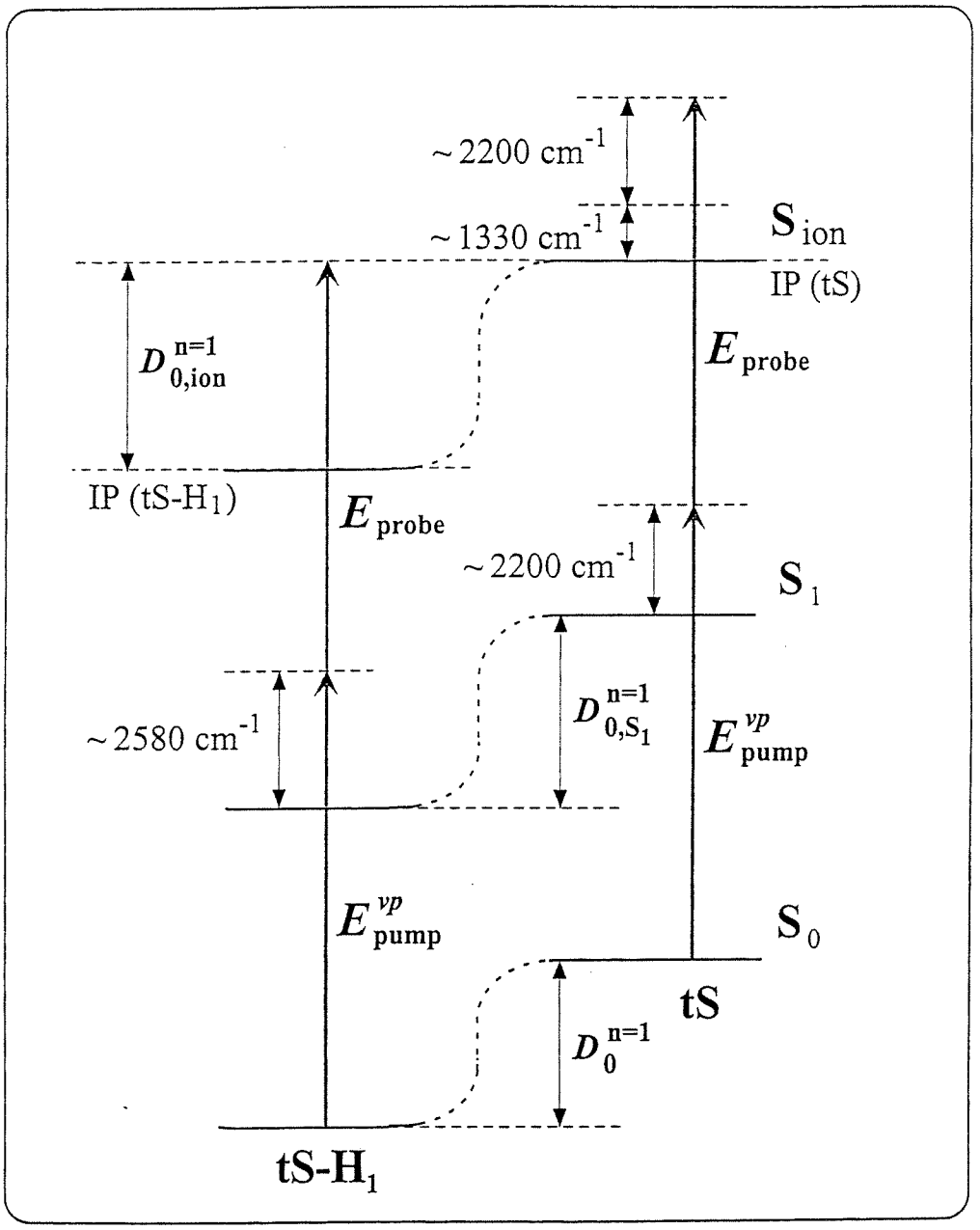
~2200 cm-1
~1330 cm-1
S ion
IP (tS)
D n=1 0,ion
E probe
IP (tS-H1)
E probe
~2200 cm-1
S 1
~2580 cm-1
D n=1 0,S1
E vp pump
E vp pump
S 0
tS
D n=1 0
tS-H1

Figure 3

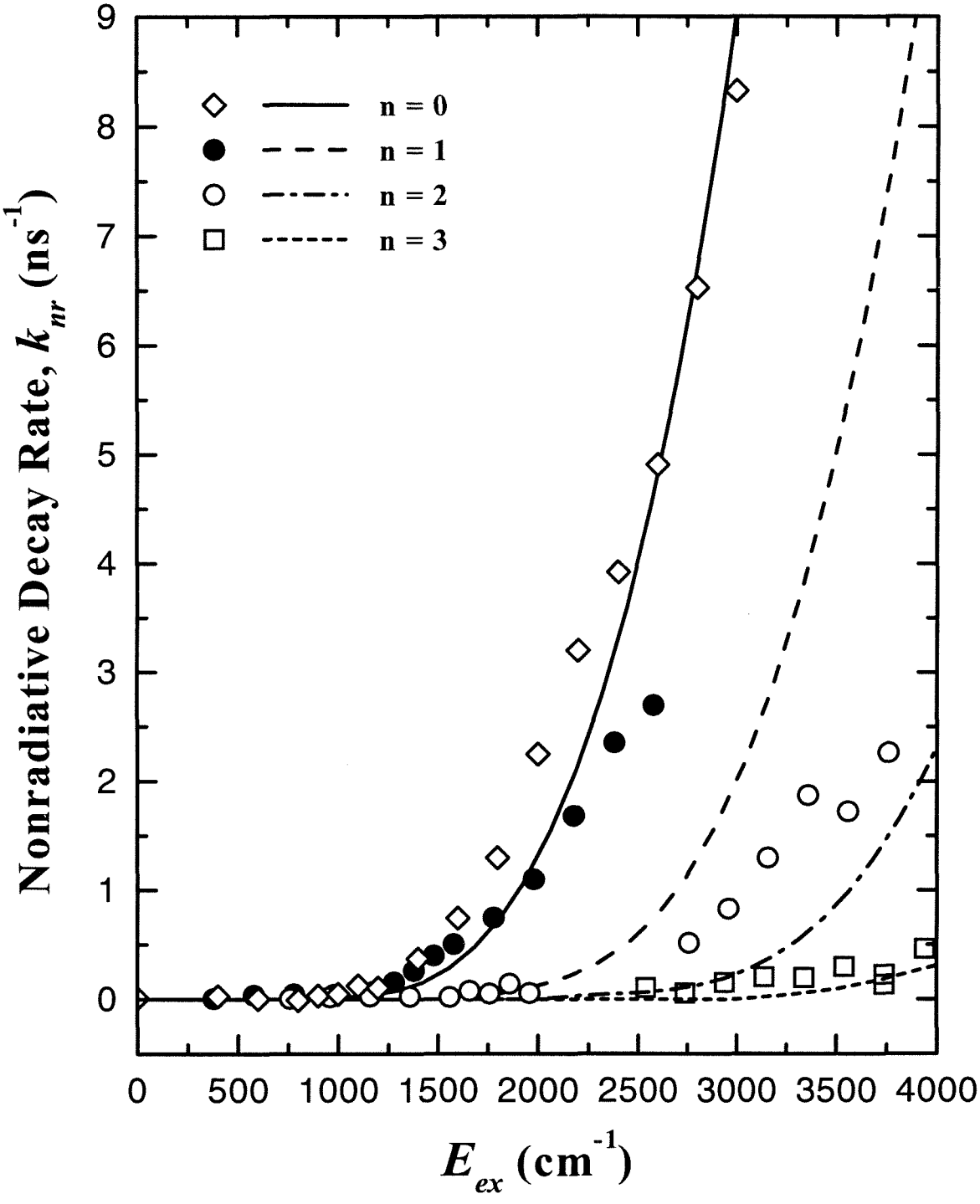
n = 0
n = 1
n = 2
n = 3
Nonradiative Decay Rate, k_{nr} (ns^{-1})
E_{ex} (cm^{-1})
0
1
2
3
4
5
6
7
8
9
0
500
1000
1500
2000
2500
3000
3500
4000

Figure 4

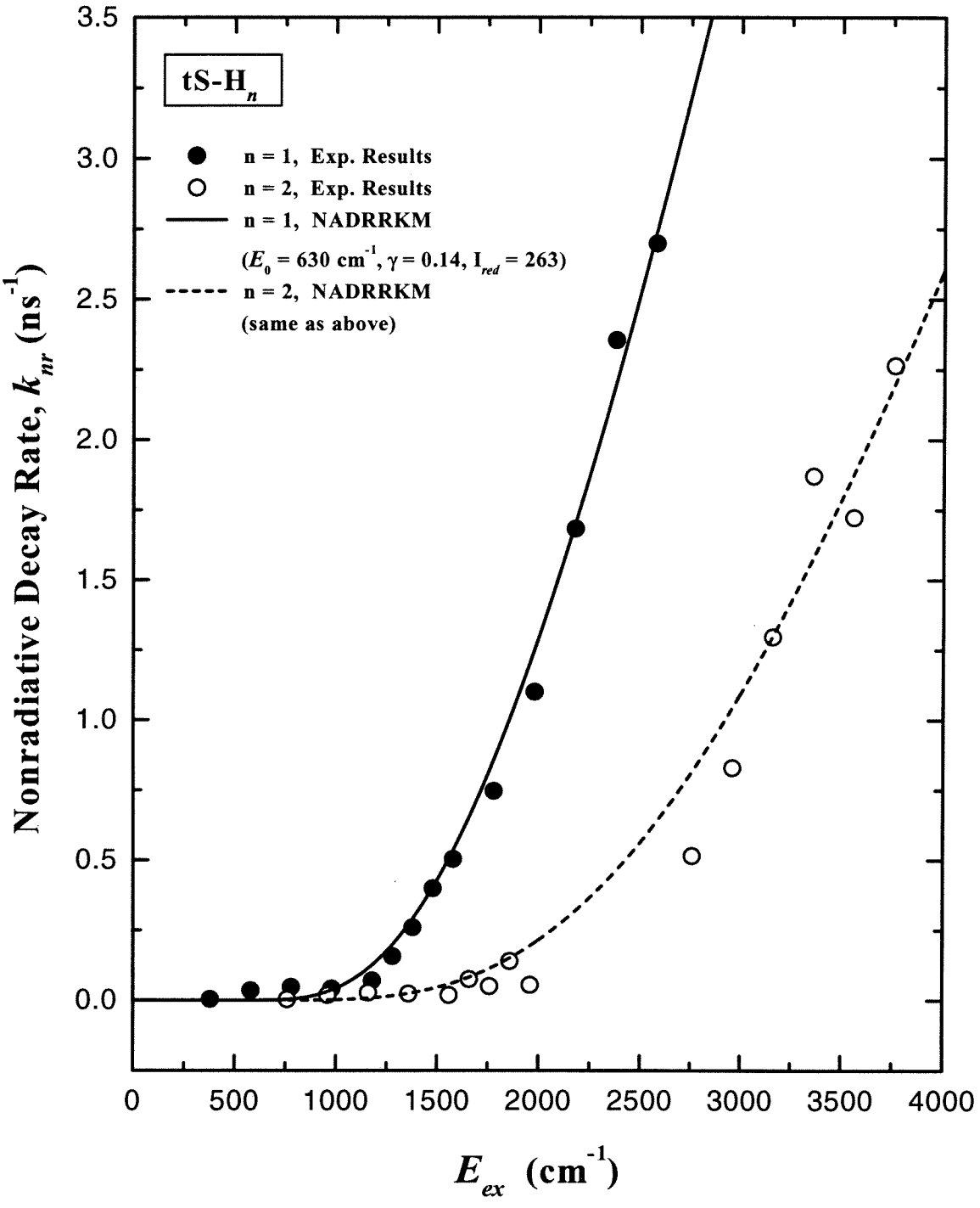
tS-H$_n$
n = 1, Exp. Results
n = 2, Exp. Results
n = 1, NADRRKM
(E_0 = 630 cm^{-1}, γ = 0.14, I$_{red}$ = 263)
n = 2, NADRRKM
(same as above)
Nonradiative Decay Rate, k_{nr} (ns^{-1})
E_{ex} (cm^{-1})
0.0
0.5
1.0
1.5
2.0
2.5
3.0
3.5
0
500
1000
1500
2000
2500
3000
3500
4000

Figure 5

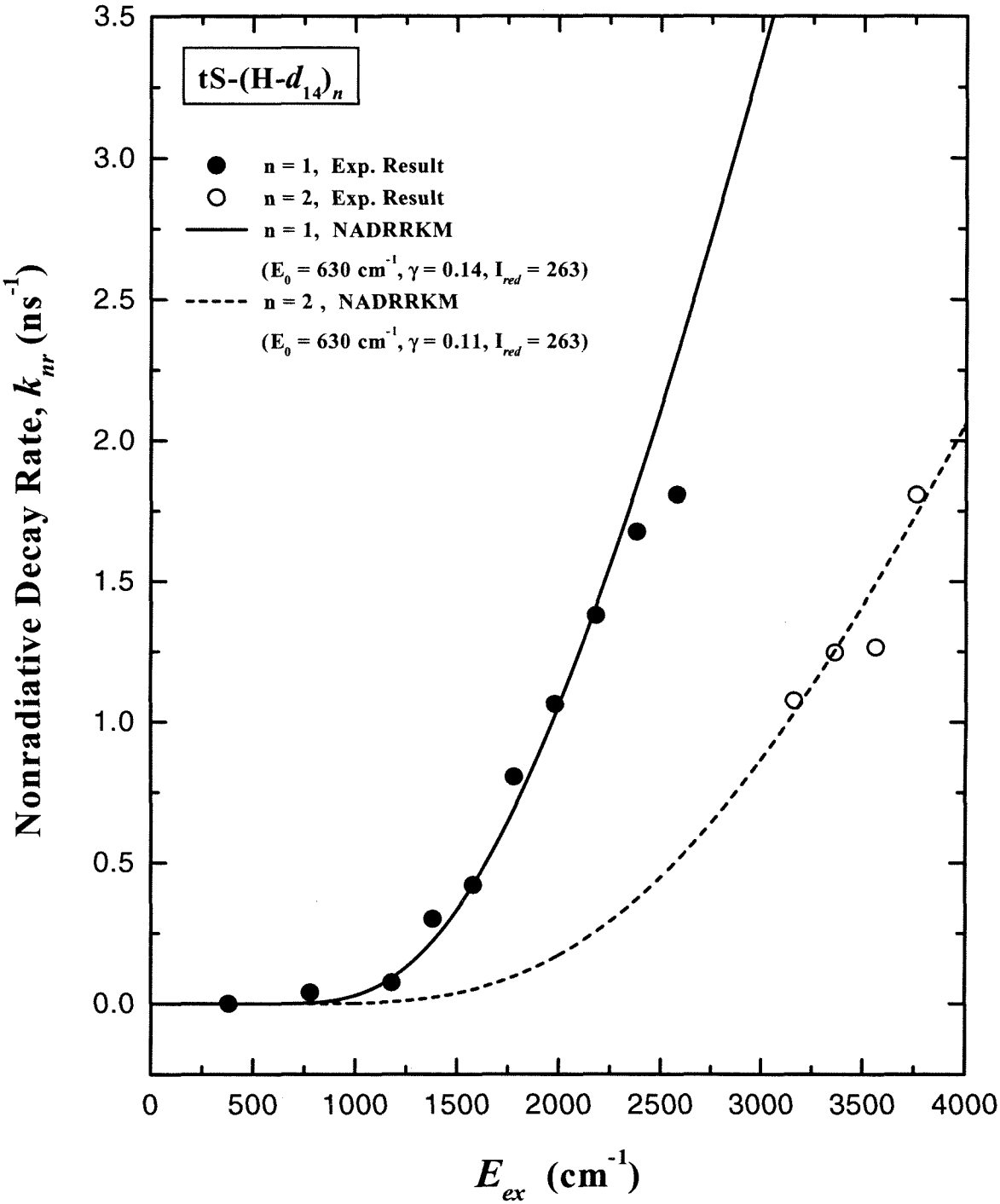
tS-(H-d_{14})$_n$
n = 1, Exp. Result
n = 2, Exp. Result
n = 1, NADRRKM
(E_0 = 630 cm^{-1}, γ = 0.14, I_{red} = 263)
n = 2 , NADRRKM
(E_0 = 630 cm^{-1}, γ = 0.11, I_{red} = 263)
Nonradiative Decay Rate, k_{nr} (ns^{-1})
E_{ex} (cm^{-1})
0.0
0.5
1.0
1.5
2.0
2.5
3.0
3.5
0
500
1000
1500
2000
2500
3000
3500
4000

Figure 6

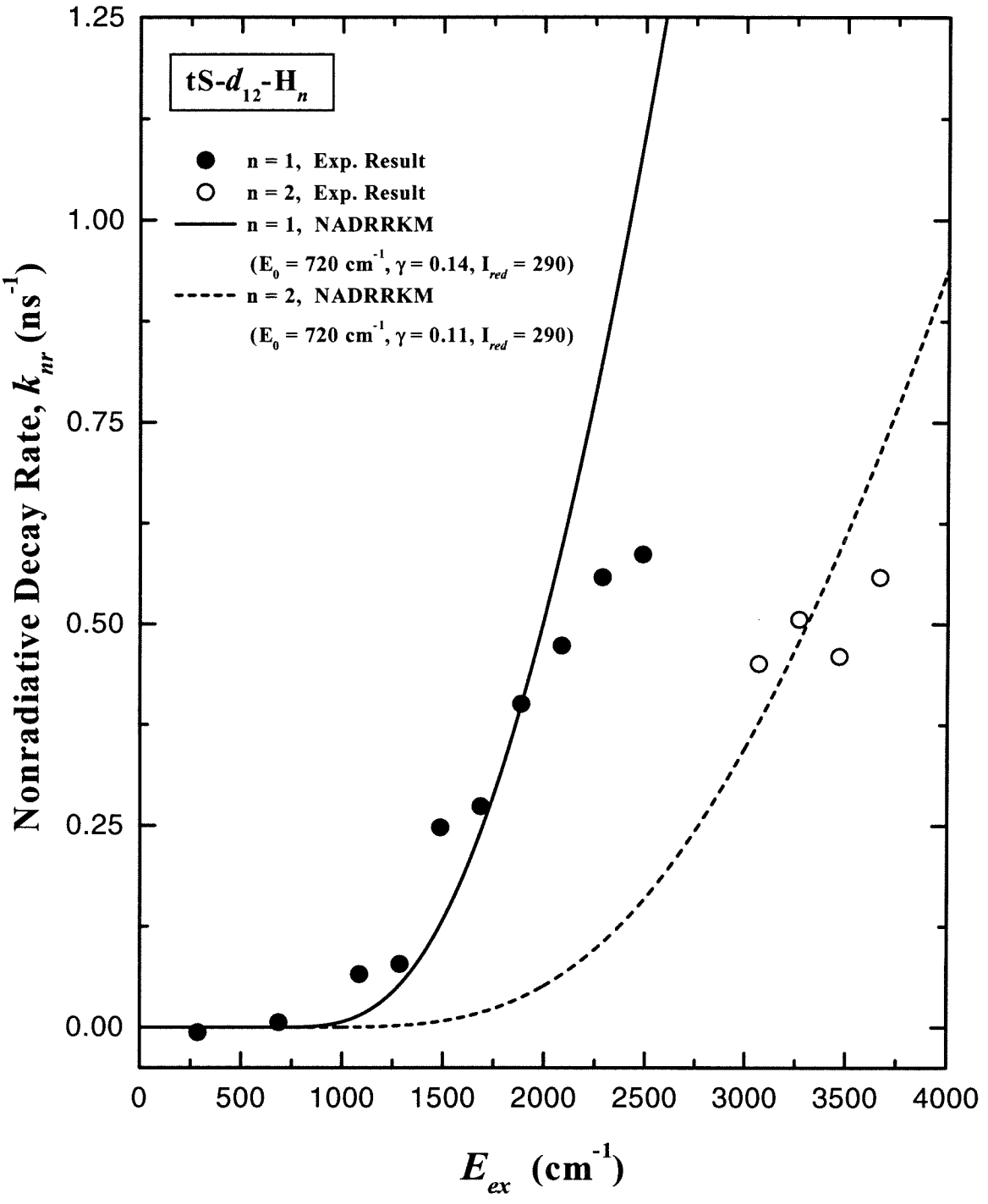
tS-d_{12}-H_n
n = 1, Exp. Result
n = 2, Exp. Result
n = 1, NADRRKM
(E_0 = 720 cm^{-1}, γ = 0.14, I_{red} = 290)
n = 2, NADRRKM
(E_0 = 720 cm^{-1}, γ = 0.11, I_{red} = 290)
Nonradiative Decay Rate, k_{nr} (ns^{-1})
E_{ex} (cm^{-1})
0.00
0.25
0.50
0.75
1.00
1.25
0
500
1000
1500
2000
2500
3000
3500
4000

Figure 7

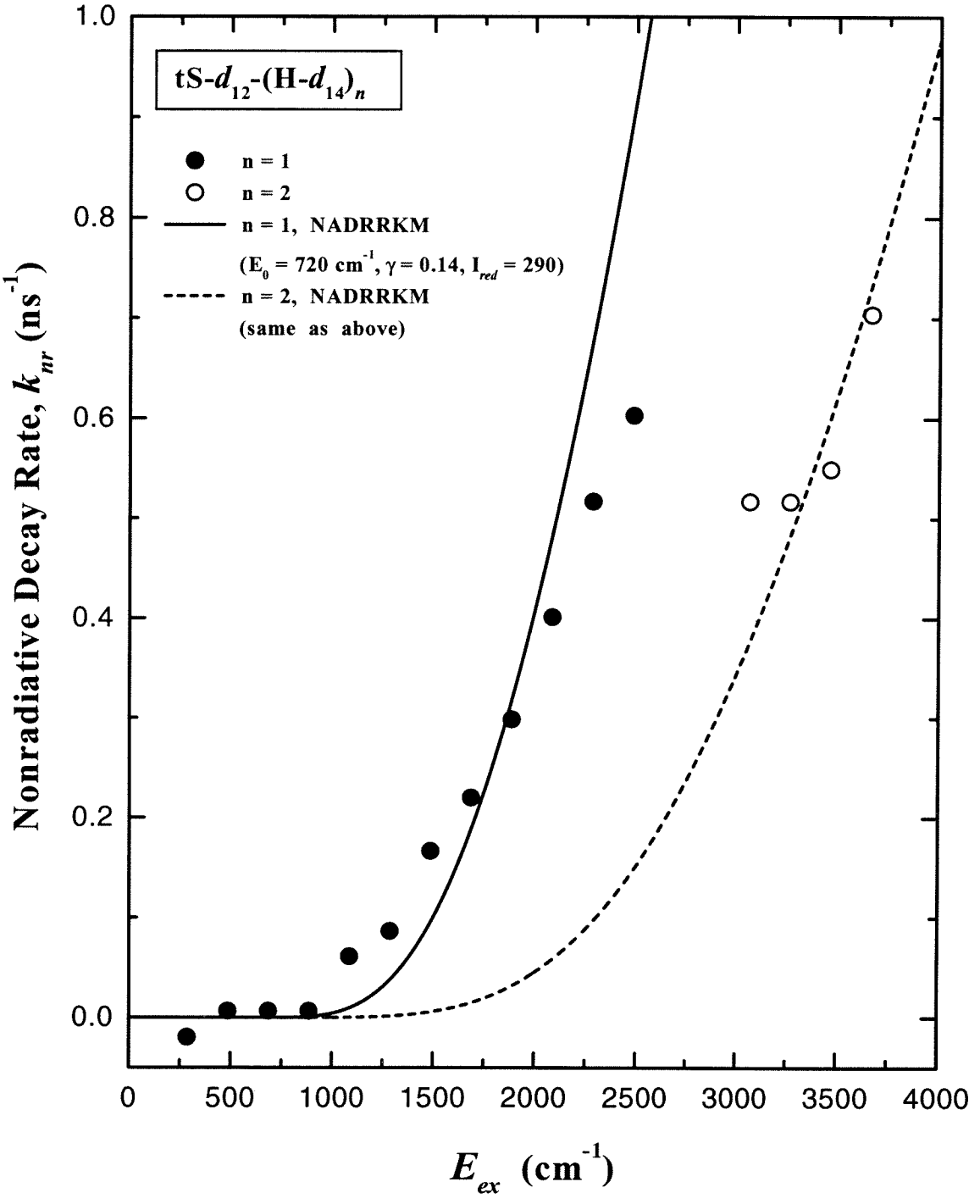
tS-d_{12}-(H-d_{14})$_n$
n = 1
n = 2
n = 1, NADRRKM
(E_0 = 720 cm^{-1}, γ = 0.14, I_{red} = 290)
n = 2, NADRRKM
(same as above)
Nonradiative Decay Rate, k_{nr} (ns^{-1})
E_{ex} (cm^{-1})
0.0
0.2
0.4
0.6
0.8
1.0
0
500
1000
1500
2000
2500
3000
3500
4000

Figure 8

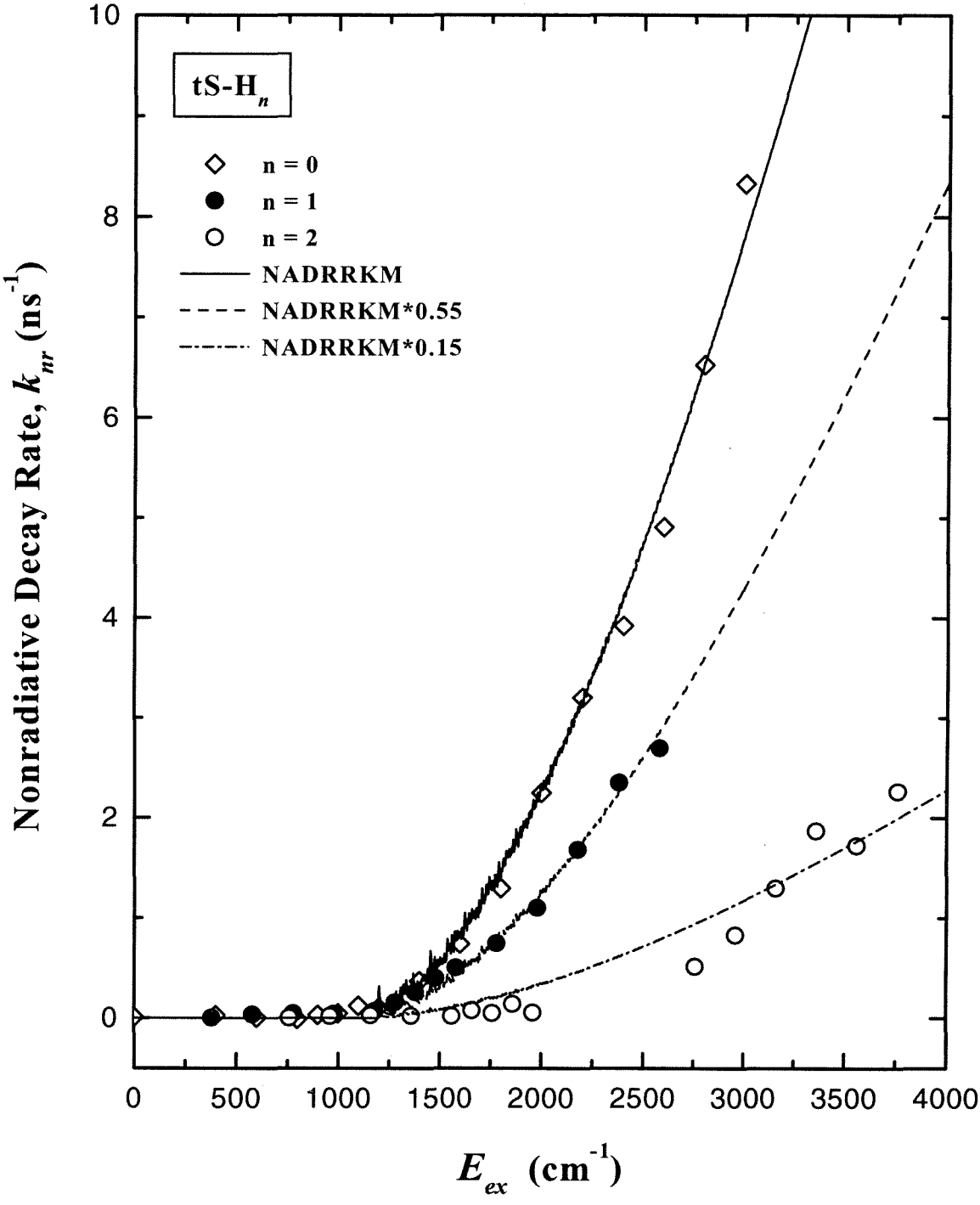
tS-H$_n$
n = 0
n = 1
n = 2
NADRRKM
NADRRKM*0.55
NADRRKM*0.15
Nonradiative Decay Rate, k_{nr} (ns^{-1})
E_{ex} (cm^{-1})
0
2
4
6
8
10
0
500
1000
1500
2000
2500
3000
3500
4000

Figure 9

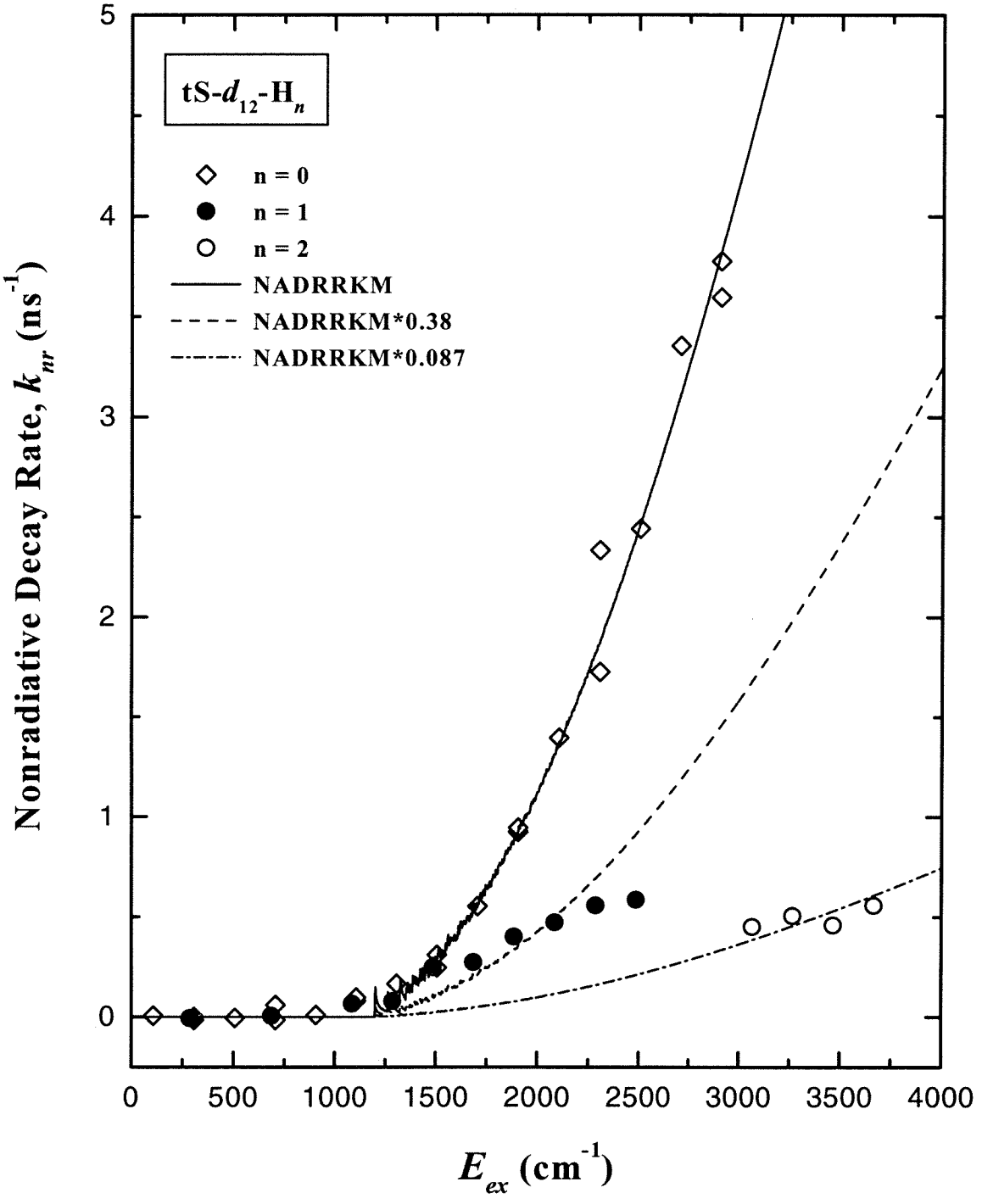
tS-d_{12}-H$_n$
n = 0
n = 1
n = 2
NADRRKM
NADRRKM*0.38
NADRRKM*0.087
Nonradiative Decay Rate, k_{nr} (ns^{-1})
E_{ex} (cm^{-1})
0
1
2
3
4
5
0
500
1000
1500
2000
2500
3000
3500
4000

Figure 10

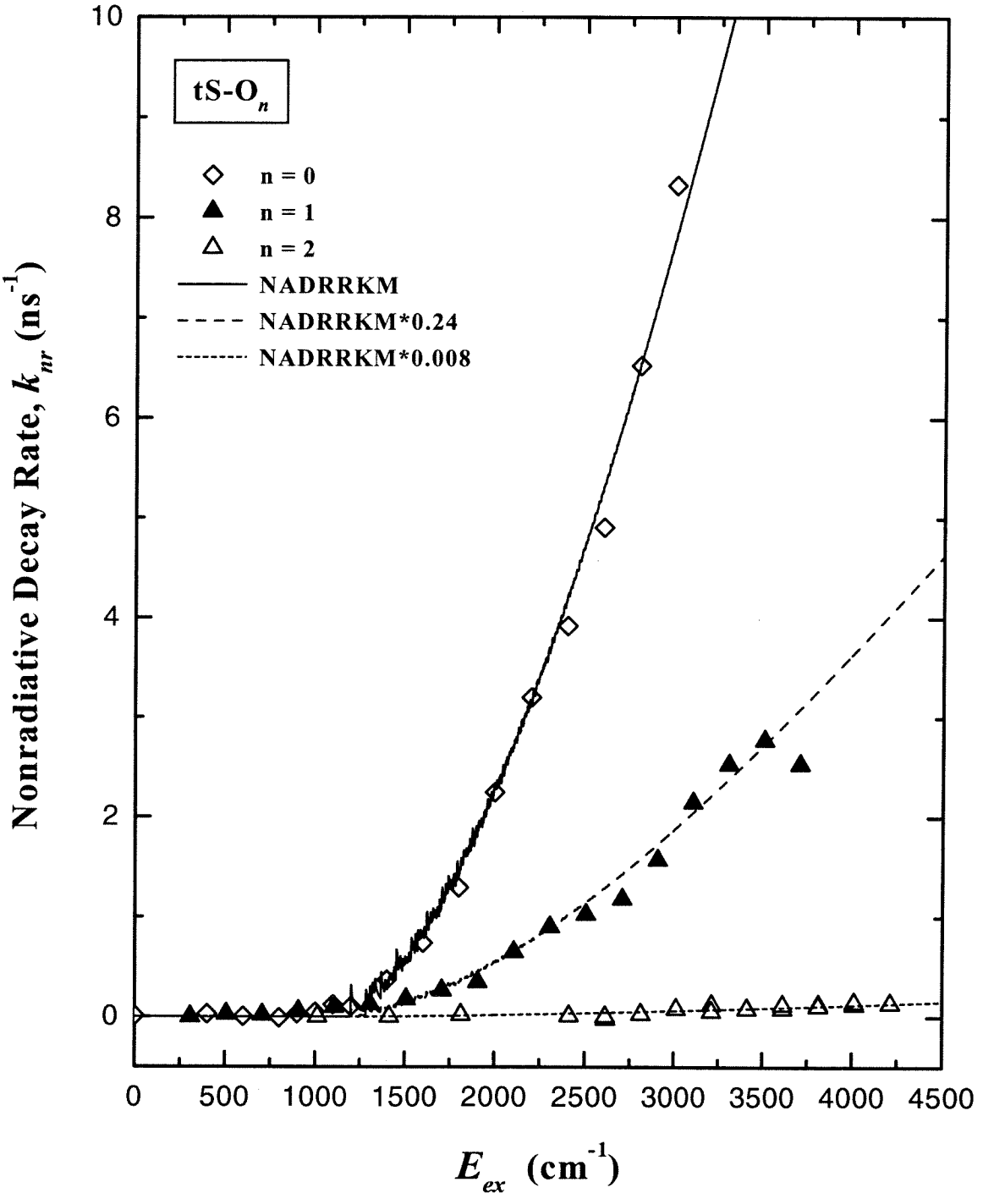
tS-O$_n$
n = 0
n = 1
n = 2
NADRRKM
NADRRKM*0.24
NADRRKM*0.008
Nonradiative Decay Rate, k_{nr} (ns^{-1})
E_{ex} (cm^{-1})
0
2
4
6
8
10
0
500
1000
1500
2000
2500
3000
3500
4000
4500

Figure 11

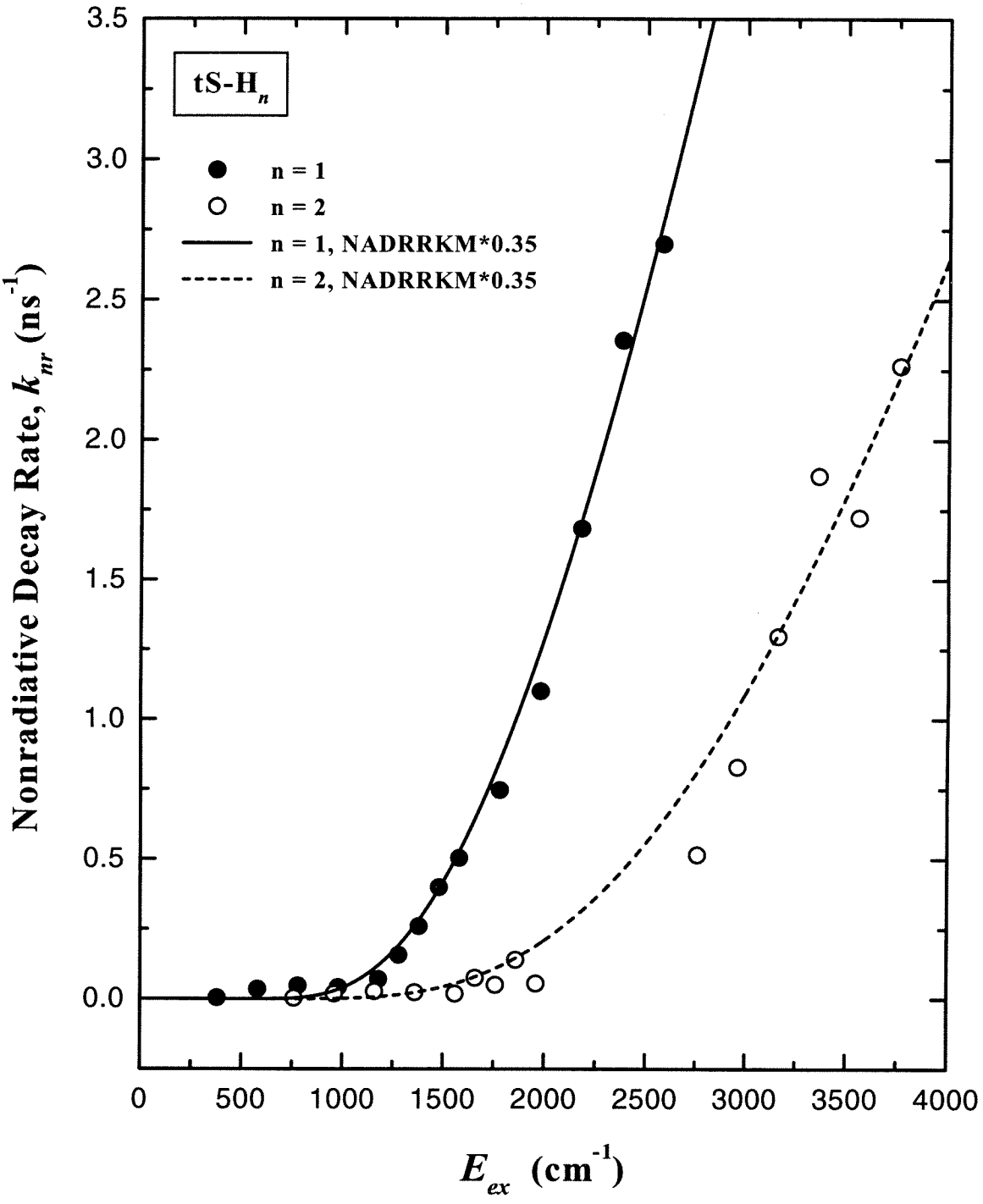
tS-H$_n$
n = 1
n = 2
n = 1, NADRRKM*0.35
n = 2, NADRRKM*0.35
Nonradiative Decay Rate, k_{nr} (ns^{-1})
E_{ex} (cm^{-1})
0.0
0.5
1.0
1.5
2.0
2.5
3.0
3.5
0
500
1000
1500
2000
2500
3000
3500
4000

Figure 12

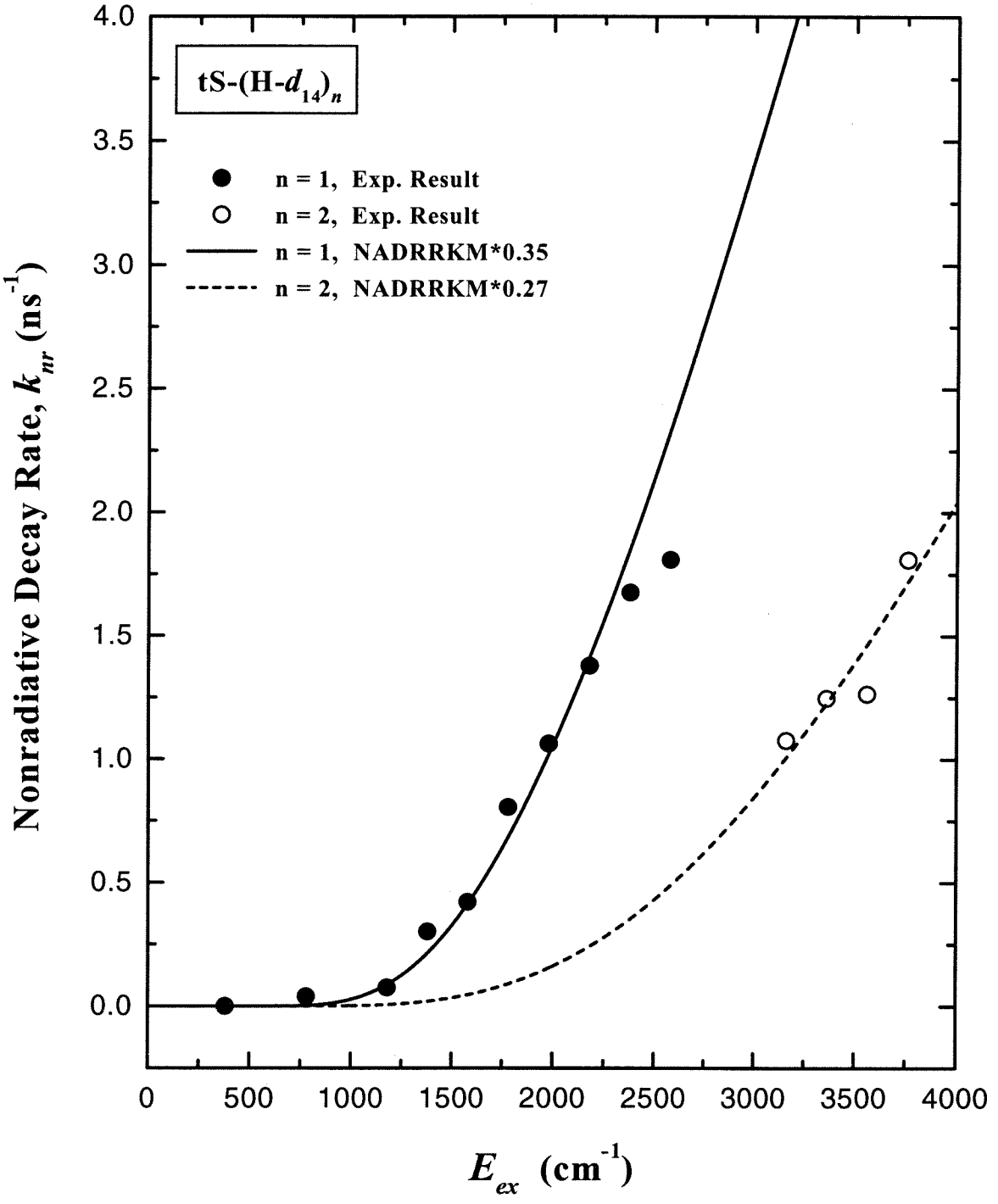
tS-(H-d_{14})$_n$
n = 1, Exp. Result
n = 2, Exp. Result
n = 1, NADRRKM*0.35
n = 2, NADRRKM*0.27
Nonradiative Decay Rate, k_{nr} (ns^{-1})
E_{ex} (cm^{-1})
0.0
0.5
1.0
1.5
2.0
2.5
3.0
3.5
4.0
0
500
1000
1500
2000
2500
3000
3500
4000

Figure 13

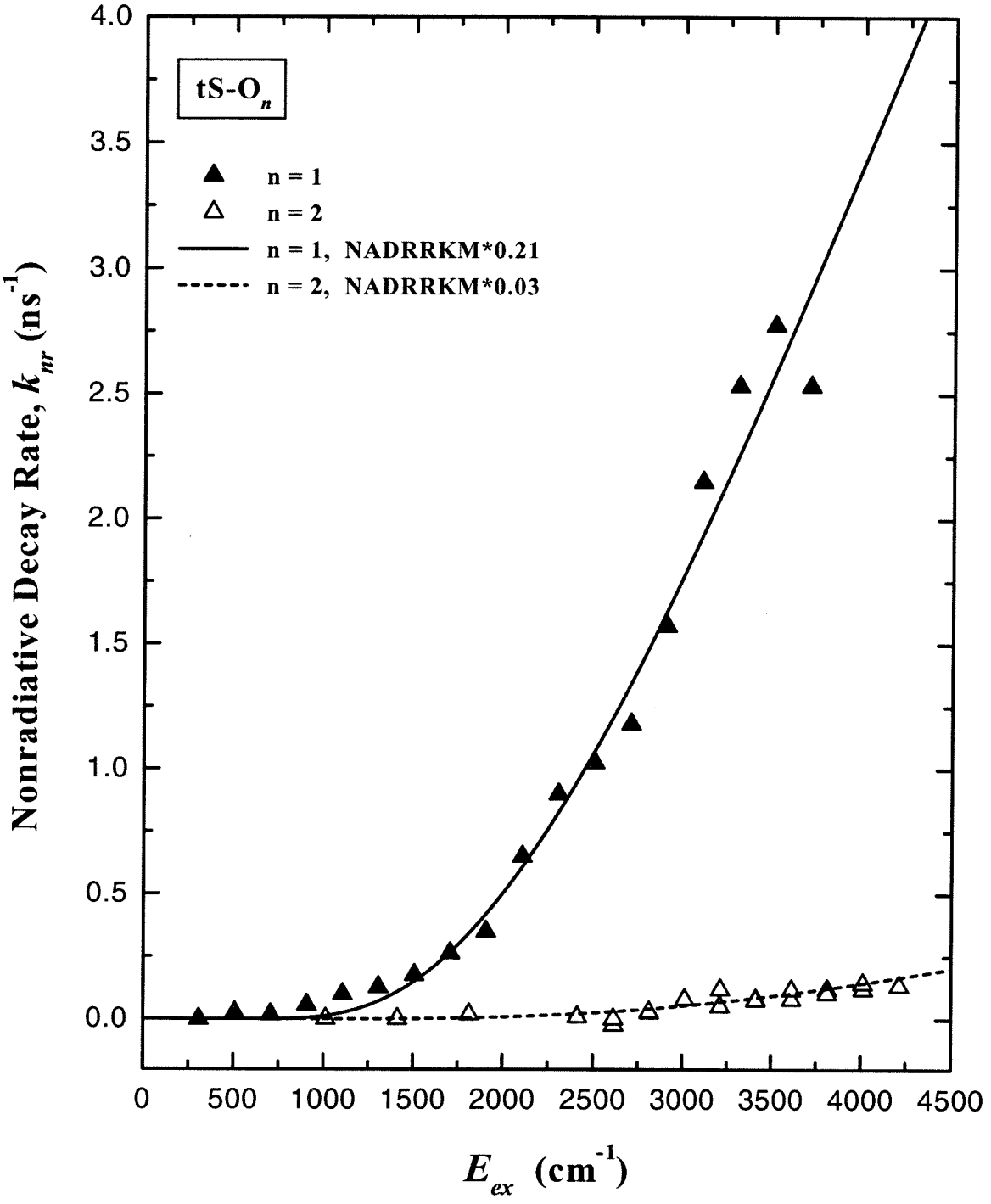
tS-O$_n$
n = 1
n = 2
n = 1, NADRRKM*0.21
n = 2, NADRRKM*0.03
Nonradiative Decay Rate, k_{nr} (ns^{-1})
E_{ex} (cm^{-1})
0.0
0.5
1.0
1.5
2.0
2.5
3.0
3.5
4.0
0
500
1000
1500
2000
2500
3000
3500
4000
4500

Figure 14

Table 1: Nonadiabatic RRKM Fitting Variables for all the tS *n*-alkane Cluster Species

Cluster Species	E_0 (cm^{-1})	γ (cm^{-1} rad)	I_{red} (amu Å^2)
tS-h_{12}	1200	0.49	263
tS-h_{12}-(H-h_{14})$_1$	630	0.14	263
tS-h_{12}-(H-h_{14})$_2$ (2+0)	630	0.14	263
tS-h_{12}-(H-d_{14})$_1$	630	0.14	263
tS-h_{12}-(H-d_{14})$_2$ (2+0)	630	0.11	263
tS-d_{12}	1290 *	0.70	290
tS-d_{12}-(H-h_{14})$_1$	720 *	0.14	290
tS-d_{12}-(H-h_{14})$_2$ (2+0)	720 *	0.11	290
tS-d_{12}-(H-d_{14})$_1$	720 *	0.14	290
tS-d_{12}-(H-d_{14})$_2$ (2+0)	720 *	0.14	290
tS-h_{12}-(O-h_{18})$_1$	630	0.09	263
tS-h_{12}-(O-h_{18})$_2$ (2+0)	900	0.10	263

* Barrier height for tS-d_{12} should be 87.5 cm^{-1} higher relative to that of tS-h_{12}, due to the zero-point energy correction, based on the vibrational frequencies computed by Negri and Orlandi [11].

Table 1

Table 2: Scaling and ζ / ω' Ratios for the tS *n*-alkane Cluster Species

Cluster Species	Scaling Ratio	ζ / ω'
tS-h_{12}-(H-h_{14})$_1$	0.55	1.27
tS-h_{12}-(H-h_{14})$_2$	0.15	6.52
tS-d_{12}-(H-h_{14})$_1$	0.38	2.25
tS-d_{12}-(H-h_{14})$_2$	0.087	11.41
tS-h_{12}-(O-h_{18})$_1$	0.24	3.93
tS-h_{12}-(O-h_{18})$_2$	0.08	125

Table 2

Chapter 5

Conclusions

The photoisomerization dynamics of tS in finite-size *n*-alkane clusters had been studied with the picosecond pump-probe TOF mass spectrometry and transient technique. The effects of vibrational predissociation at the S_1 and the ion state on the transients measured were first investigated to ensure that the rates obtained were attributed to the correct cluster species. From the drop-offs observed in the excess energy dependence studies, the shape of the TOF mass spectra, and analysis of the kinetic scheme, it was deduced that the vp lifetime of tS-A_1 at the ion state is less than 75 ns at energies where vp is significant. In addition, from examining various possible scenarios regarding vp and isomerization in light of our $k_{nr}(E_{ex})$ vs. E_{ex} results, it was concluded that isomerization has to be much faster than vp at the S_1 state in the E_{ex} range we investigated. The excess energy dependence of the rates measured at the mass of tS-H_1 provided the information necessary to derive an experimental value for the binding energy between tS and hexane of ~ 3910 cm^{-1} at the S_1 state. Similarly, the binding energy between tS and octane in tS-O_1 cluster at the S_1 state was determined to be ~ 4840 cm^{-1}.

The observed excess energy dependence of the isomerization rate for all the cases we studied can be very well accounted for by the nonadiabatic RRKM theory utilized previously by this group. Standard RRKM theories, such as that proposed by Gershinsky and Pollak, were less satisfactory in predicting the $k_{nr}(E_{ex})$ vs. E_{ex} results for tS-H_n. Based on the nonadiabatic RRKM fits, the barriers to isomerization for tS-h_{12}, tS-h_{12}-(H-h_{14})$_1$ and tS-h_{12}-(H-d_{14})$_1$ were found to be ~ 1200 cm^{-1}, ~ 630 cm^{-1} and ~ 630 cm^{-1}

respectively. This observation can be attributed to the fact that in the clusters, the phantom state, which is zwitterionic, was stabilized more than the S_1 state as a result of *n*-hexane solvation. The extent of the barrier height reduction was similar to that derived from solution phase studies [1,2]. Prediction of the microcanonical rates of tS-d_{12}, tS-d_{12}-(H-h_{14})$_1$ and tS-d_{12}-(H-d_{14})$_1$ were subsequently made with the nonadiabatic parameters obtained from RRKM fits mentioned above. The theoretical rates were found to agree very well with the experimental data.

In addition to the 1:1 complexes, the nonadiabatic RRKM theory was also able to predict the microcanonical rates of the tS-hexane 1:2 complexes very well. The microcanonical rates for the 1:2 complexes can be predicted by simply substituting the vibrational frequencies of the 1:1 complexes with that of the corresponding 1:2, without having to alter the nonadiabatic parameters, except in the case of tS-h_{12}-(H-d_{14})$_2$ and tS-d_{12}-(H-h_{14})$_2$, where minor adjustment of the γ value was needed. This was not the case for tS-O_2, but the poor vibrational cooling that is evident in that case raises the possibility of complications from higher cluster dissociation, so the result is not conclusive. From the above observations, it was concluded that the tS-H_2 produced were primarily (2+0) rather than (1+1) isomers, and the reduction in the isomerization rate of the 1:2 relative to the 1:1 complex is simply due to *energy friction*. The argument that the (2+0) isomer is the dominant species is consistent with the results of the minimum energy calculation.

The applicability of the Kramers-type friction model in microcanonical systems was examined in this thesis. It was found that more satisfactory results are produced by

taking into account both energy and motional friction, along with barrier modification, than by consideration of motional friction only. The Kramers-type model does not give conclusive indication as to which type of friction is more dominant. However, it does suggest that motional friction alone cannot account for the rate reduction in tS *n*-alkane clusters.

5.1. References

1. Schroeder, J.; Schwarzer, D.; Troe, J.; Voss, F. *J. Chem. Phys.* **1990**, *93*, 2393.

2. Schroeder, J.; Troe, J. *Chem. Phys. Lett.* **1985**, *116*, 453.

Appendix I

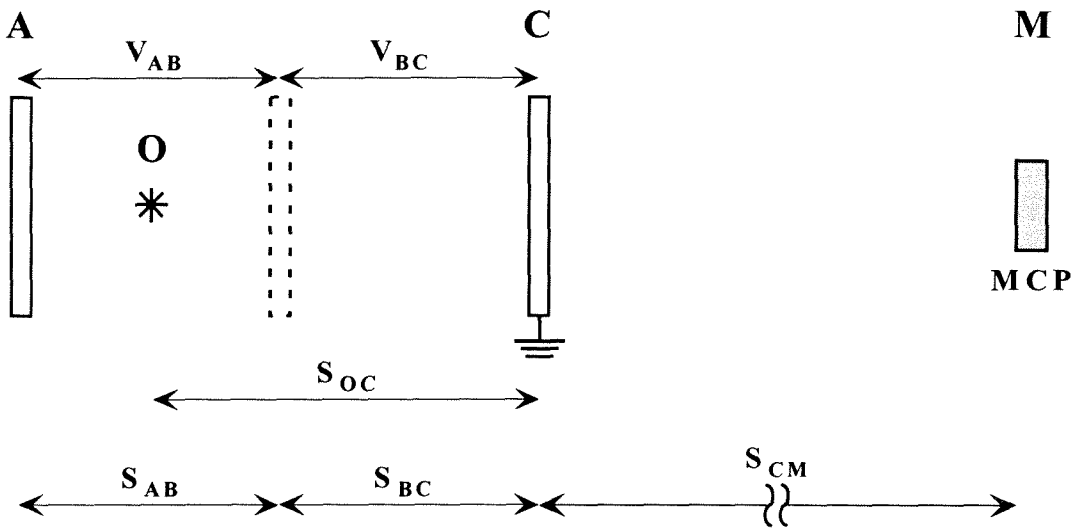

Figure 1

In this appendix, the derivation of the equation describing Δt, the time-of-flight difference between an intact A-B_n^+ cluster and a trailing nascent A-B_n^+ cluster, which is produced from vibrational predissociation of A-B_{n+1}^+, will be shown. Fig. 1 above depicts the three potential grids, A (repeller grid), B (extractor grid) and C (ground grid) found in the TOF assembly. Point O is where the clusters are ionized, and the ions are than directed by the grids to the MCP. V_{AB} and V_{BC} are the potentials between grid A and B, and between grid B and C, respectively. S_{AB} and S_{BC} represent the distances between grid A and B, and grid B and C. S_{OC} is the distance between the point of ionization and grid C, while S_{CM} is the distance between grid C and the MCP. Since S_{AB} and S_{BC} are the same, and $V_{BC} \sim 0.75\ V_{AB}$ in our experimental setup, for simplicity, during the derivation of Δt, the dual-stage potential field will be treated as a single stage

potential field, whereby the potential drop between the point of ionization, O, and grid C, is assumed linear.

(a) General Description

Let W_{12} be the work done on a cluster with charge q. If the cluster travels from point 1 and 2, and the potential difference between the two points equals to V_{12}, then the work done on the clusters can be written as

$$W_{12} = q \cdot V_{12} = F \cdot S_{12} \qquad \text{(AI-1)}$$

where F is the force exerted on the cluster and S_{12} is the distance between point 1 and 2. Therefore,

$$q \cdot V_{12} = M \cdot a_{12} \cdot S_{12} \qquad \text{(AI-2)}$$

and

$$a_{12} = \frac{q \cdot V_{12}}{M \cdot S_{12}} \qquad \text{(AI-3).}$$

Here, a_{12} is the acceleration and M is the mass of the cluster.

From Newtonian equations of motion, we have

$$S_{12} = u_1 \cdot t_{12} + \frac{1}{2} \cdot a_{12} \cdot t_{12}^{\,2} \qquad \text{(AI-4)}$$

where u_1 is the initial velocity of the clusters at point 1, and t_{12} is the time of travel between point 1 and 2. Since $u_1 = 0$ in our case, the above equation can be rearranged as follows:

$$t_{12} = \left(\frac{2 \cdot S_{12}}{a_{12}} \right)^{\frac{1}{2}} = \left(\frac{2 \cdot M \cdot S_{12}{}^2}{q \cdot V_{12}} \right)^{\frac{1}{2}} \qquad \text{(AI-5).}$$

The velocity of the cluster at point 2, v_2, can be expressed as

$$v_2 = a_{12} \cdot t_{12} = \left(\frac{q \cdot V_{12}}{M \cdot S_{12}} \right) \cdot \left(\frac{2 \cdot M \cdot S_{12}{}^2}{q \cdot V_{12}} \right)^{\frac{1}{2}} \qquad \text{(AI-6)}$$

$$v_2 = \left(\frac{2 \cdot q \cdot V_{12}}{M} \right)^{\frac{1}{2}} \qquad \text{(AI-7).}$$

(b) The Time-of-Flight (TOF) of an Intact A-B_n^+ Cluster

Let M_1 be the mass of an intact A-B_n Cluster, and t_{Total1} be the total TOF of the cluster. Then, t_{Total1} can be expressed as

$$t_{Total1} = t_{1,OC} + t_{1,CM} \qquad \text{(AI-8)}$$

where $t_{1,OC}$ and $t_{1,CM}$ are the time it takes the intact cluster to travel from point O to grid C, and from grid C to the MCP, respectively. Since it is assumed that the potential field in our TOF assembly is single stage and uniform, the expression for $t_{1,OC}$ can be readily obtained from Eq. (AI-5). The expression for $t_{1,CM}$ is simply $S_{CM}/v_{1,C}$, where $v_{1,C}$ is the

velocity of the intact cluster at grid C, which is described by Eq. (AI-7). Hence, the equation for t_{Total1} can be written as

$$t_{Total\,1} = \left(\frac{2 \cdot M_1 \cdot {S_{OC}}^2}{q \cdot V_{OC}} \right)^{\frac{1}{2}} + \left(\frac{M_1 \cdot {S_{CM}}^2}{2 \cdot q \cdot V_{OC}} \right)^{\frac{1}{2}} \qquad \text{(AI-9)}$$

$$= \left(\frac{M_1}{2 \cdot q \cdot V_{OC}} \right)^{\frac{1}{2}} \cdot \left[2 \cdot S_{OC} + S_{CM} \right] \qquad \text{(AI-10).}$$

(c) The Time-of-Flight (TOF) of a Nascent A-B_n^+ Cluster

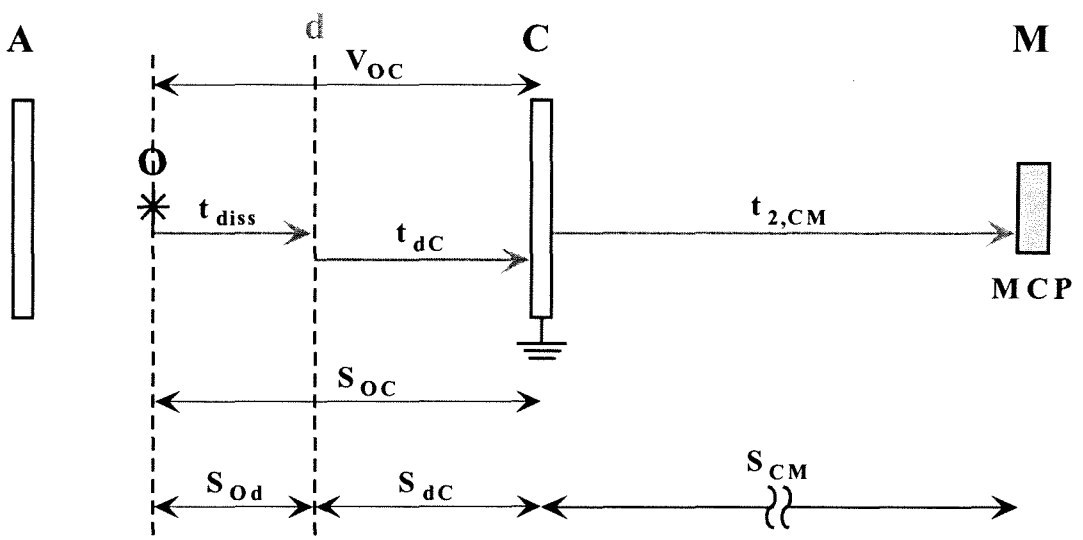

Figure 2

A nascent A-B_n^+ cluster is an A-B_n^+ cluster which is produced by the vibrational predissociation (vp) of A-B_{n+1}^+: A-$B_{n+1}^+ \xrightarrow{vp}$ A-B_n^+ + B. Although when acquired

enough energy to undergo vp, the A-B_{n+1}^+ population as a whole will have a decay lifetime, each individual A-B_{n+1}^+ cluster actually vibrational predissociates at a discrete time, t_{diss}, after being ionized. The equation for the TOF of a nascent A-B_n^+ cluster produced at t_{diss} is given as follows, and the relevant terms are shown in Fig. 2.

$$t_{Total2} = t_{diss} + t_{dC} + t_{2,CM} \qquad \text{(AI-11).}$$

To calculate t_{dC}, one must first find out the velocity of A-B_{n+1}^+ at the point of dissociation, d, and the distance from d to grid C. The velocity at point d is given by the following equation:

$$v_d = a_{Od} \cdot t_{diss} = \left(\frac{q \cdot V_{OC}}{M_2 \cdot S_{OC}} \right) \cdot t_{diss} \qquad \text{(AI-12)}$$

where a_{Od} is the acceleration of A-B_{n+1}^+ between point O and d, and M_2 is the mass of A-B_{n+1}^+. The distance traveled by A-B_{n+1}^+ before vp is given by

$$S_{Od} = \frac{1}{2} \cdot a_{Od} \cdot t_{diss}^{\ 2} = \frac{1}{2} \cdot \left(\frac{q \cdot V_{OC}}{M_2 \cdot S_{OC}} \right) \cdot t_{diss}^{\ 2} \qquad \text{(AI-13).}$$

The distance traveled by the nascent A-B_n^+ from d to C is

$$S_{dC} = S_{OC} - S_{Od} = S_{OC} - \frac{1}{2} \cdot \left(\frac{q \cdot V_{OC}}{M_2 \cdot S_{OC}} \right) \cdot t_{diss}^{\ 2} \qquad \text{(AI-14).}$$

Since $$S_{dC} = v_d \cdot t_{dC} + \frac{1}{2} \cdot a_{dC} \cdot t_{dC}^{\ 2} \qquad \text{(AI-15)}$$

and $$a_{dC} = \left(\frac{q \cdot V_{dC}}{M_1 \cdot S_{dC}}\right) = \left(\frac{q \cdot V_{OC}}{M_1 \cdot S_{OC}}\right) \quad \text{(AI-16)},$$

therefore, $$S_{dC} = \left(\frac{q \cdot V_{OC}}{M_2 \cdot S_{OC}}\right) \cdot t_{diss} \cdot t_{dC} + \frac{1}{2} \cdot \left(\frac{q \cdot V_{OC}}{M_1 \cdot S_{OC}}\right) \cdot t_{dC}^{\,2} \quad \text{(AI-17)}.$$

By equating Eq. (AI-14) with Eq. (AI-17), we have

$$S_{OC} - \frac{1}{2} \cdot \left(\frac{q \cdot V_{OC}}{M_2 \cdot S_{OC}}\right) \cdot t_{diss}^{\,2} = \left(\frac{q \cdot V_{OC}}{M_2 \cdot S_{OC}}\right) \cdot t_{diss} \cdot t_{dC} + \frac{1}{2} \cdot \left(\frac{q \cdot V_{OC}}{M_1 \cdot S_{OC}}\right) \cdot t_{dC}^{\,2} \quad \text{(AI-18)}.$$

Multiplying each term in the above equation by $(S_{OC} / q \cdot V_{OC})$ yields

$$\frac{S_{OC}^{\,2}}{q \cdot V_{OC}} - \frac{1}{2} \cdot \left(\frac{t_{diss}^{\,2}}{M_2}\right) = \left(\frac{t_{diss}}{M_2}\right) \cdot t_{dC} + \frac{1}{2} \cdot \left(\frac{1}{M_1}\right) \cdot t_{dC}^{\,2} \quad \text{(AI-19)},$$

$$\therefore \quad \left(\frac{1}{2 \cdot M_1}\right) \cdot t_{dC}^{\,2} + \left(\frac{t_{diss}}{M_2}\right) \cdot t_{dC} + \left[\left(\frac{t_{diss}^{\,2}}{2 \cdot M_2}\right) - \frac{S_{OC}^{\,2}}{q \cdot V_{OC}}\right] = 0 \quad \text{(AI-20)}.$$

To solve for t_{dC} from the above quadratic equation,

Let $A = \left(\frac{1}{2 \cdot M_1}\right)$; $B = \left(\frac{t_{diss}}{M_2}\right)$; and $C = \left[\left(\frac{t_{diss}^{\,2}}{2 \cdot M_2}\right) - \frac{S_{OC}^{\,2}}{q \cdot V_{OC}}\right]$

Therefore,

$$t_{dC} = \frac{-B \pm \sqrt{B^2 - 4AC}}{2A} \quad \text{(AI-21)}$$

$$t_{dC} = \frac{-\left(\frac{t_{diss}}{M_2}\right) \pm \sqrt{\left(\frac{t_{diss}}{M_2}\right)^2 - \left(\frac{2}{M_1}\right)\cdot\left[\left(\frac{t_{diss}^{\ 2}}{2\cdot M_2}\right) - \frac{S_{OC}^{\ 2}}{q\cdot V_{OC}}\right]}}{\left(\frac{1}{M_1}\right)} \qquad \text{(AI-22)}$$

$$= -\left(\frac{M_1}{M_2}\right)\cdot t_{diss} \pm \sqrt{\left(\frac{M_1}{M_2}\right)^2 \cdot t_{diss}^{\ 2} - \left(\frac{M_1}{M_2}\right)\cdot t_{diss}^{\ 2} + \frac{2\cdot M_1 \cdot S_{OC}^{\ 2}}{q\cdot V_{OC}}} \qquad \text{(AI-23).}$$

Since t_{dC} must be a positive number, only one of the above two solutions are acceptable.

Therefore,

$$t_{dC} = \sqrt{\left(\frac{M_1^{\ 2} - M_1\cdot M_2}{M_2^{\ 2}}\right)\cdot t_{diss}^{\ 2} + \frac{2\cdot M_1\cdot S_{OC}^{\ 2}}{q\cdot V_{OC}}} - \left(\frac{M_1}{M_2}\right)\cdot t_{diss} \qquad \text{(AI-24).}$$

Now that t_{dC} is determined, $t_{2,CM}$ is the remaining term to be solved in order for us to obtain a complete expression for t_{Total2} in Eq. (AI-11). To solve $t_{2,CM}$, however, we will need to first find the velocity of the nascent A-B_n^+ cluster at grid C, $v_{2,C}$, right before it enters the field free region.

$$v_{2,C} = v_d + a_{dC}\cdot t_{dC} \qquad \text{(AI-25)}$$

$$= \left(\frac{q\cdot V_{OC}}{M_2\cdot S_{OC}}\right)\cdot t_{diss}$$

$$+ \left(\frac{q\cdot V_{OC}}{M_1\cdot S_{OC}}\right)\cdot\left\{\sqrt{\left(\frac{M_1^{\ 2} - M_1\cdot M_2}{M_2^{\ 2}}\right)\cdot t_{diss}^{\ 2} + \frac{2\cdot M_1\cdot S_{OC}^{\ 2}}{q\cdot V_{OC}}} - \left(\frac{M_1}{M_2}\right)\cdot t_{diss}\right\}$$

(AI-26)

$$= \left(\frac{q \cdot V_{OC}}{M_1 \cdot S_{OC}}\right) \cdot \left\{ \sqrt{\left(\frac{M_1^{\,2} - M_1 \cdot M_2}{M_2^{\,2}}\right) \cdot t_{diss}^{\,2} + \frac{2 \cdot M_1 \cdot S_{OC}^{\,2}}{q \cdot V_{OC}}} \right\} \qquad \text{(AI-27).}$$

The flight time of the nascent A-B_n^+ cluster from grid C to the MCP is simply

$$t_{2,CM} = \frac{S_{CM}}{v_{2,C}} \qquad \text{(AI-28)}$$

$$t_{2,CM} = \frac{S_{CM}}{\left(\frac{q \cdot V_{OC}}{M_1 \cdot S_{OC}}\right) \cdot \left\{ \sqrt{\left(\frac{M_1^{\,2} - M_1 \cdot M_2}{M_2^{\,2}}\right) \cdot t_{diss}^{\,2} + \frac{2 \cdot M_1 \cdot S_{OC}^{\,2}}{q \cdot V_{OC}}} \right\}} \qquad \text{(AI-29)}$$

$$= \left(\frac{M_1 \cdot S_{OC} \cdot S_{CM}}{q \cdot V_{OC}}\right) \cdot \left\{ \left(\frac{M_1^{\,2} - M_1 \cdot M_2}{M_2^{\,2}}\right) \cdot t_{diss}^{\,2} + \frac{2 \cdot M_1 \cdot S_{OC}^{\,2}}{q \cdot V_{OC}} \right\}^{-\frac{1}{2}} \qquad \text{(AI-30).}$$

Hence, the equation for t_{Total2} can be written as

$$t_{Total2} = t_{diss} + \left\{ \left(\frac{M_1^{\,2} - M_1 \cdot M_2}{M_2^{\,2}}\right) \cdot t_{diss}^{\,2} + \frac{2 \cdot M_1 \cdot S_{OC}^{\,2}}{q \cdot V_{OC}} \right\}^{\frac{1}{2}} - \left(\frac{M_1}{M_2}\right) \cdot t_{diss}$$

$$+ \left(\frac{M_1 \cdot S_{OC} \cdot S_{CM}}{q \cdot V_{OC}}\right) \cdot \left\{ \left(\frac{M_1^{\,2} - M_1 \cdot M_2}{M_2^{\,2}}\right) \cdot t_{diss}^{\,2} + \frac{2 \cdot M_1 \cdot S_{OC}^{\,2}}{q \cdot V_{OC}} \right\}^{-\frac{1}{2}} \qquad \text{(AI-31).}$$

(d) The TOF Difference between an Intact and a Trailing Nascent A-B_n^+ Cluster

The time-of-flight difference between an intact A-B_n^+ cluster and a trailing nascent A-B_n^+ cluster, Δt, is as follows:

$$\Delta t = t_{Total2} - t_{Total1} \qquad \text{(AI-30)}.$$

Substituting Eqs. (AI-10) and (AI-31) into the above equation yields

$$\Delta t = \left[1 - \left(\frac{M_1}{M_2}\right)\right] \cdot t_{diss} + \left\{\left(\frac{M_1^{\,2} - M_1 \cdot M_2}{M_2^{\,2}}\right) \cdot t_{diss}^{\,2} + \frac{2 \cdot M_1 \cdot S_{OC}^{\,2}}{q \cdot V_{OC}}\right\}^{\frac{1}{2}} + \left(\frac{M_1 \cdot S_{OC} \cdot S_{CM}}{q \cdot V_{OC}}\right) \cdot \left\{\left(\frac{M_1^{\,2} - M_1 \cdot M_2}{M_2^{\,2}}\right) \cdot t_{diss}^{\,2} + \frac{2 \cdot M_1 \cdot S_{OC}^{\,2}}{q \cdot V_{OC}}\right\}^{-\frac{1}{2}} - \left(\frac{M_1}{2 \cdot q \cdot V_{OC}}\right)^{\frac{1}{2}} \cdot \left[2 \cdot S_{OC} + S_{CM}\right] \qquad \text{(AI-31)}.$$

(e) Simplify Δt for Small t_{diss}

Let $X1 = \left[1 - \left(\frac{M_1}{M_2}\right)\right]$; $X2 = \left(\frac{M_1^{\,2} - M_1 \cdot M_2}{M_2^{\,2}}\right)$;

$X3 = \frac{2 \cdot M_1 \cdot S_{OC}^{\,2}}{q \cdot V_{OC}}$; $X4 = \left(\frac{M_1 \cdot S_{OC} \cdot S_{CM}}{q \cdot V_{OC}}\right)$; and

$X5 = \left(\frac{M_1}{2 \cdot q \cdot V_{OC}}\right)^{\frac{1}{2}} \cdot \left[2 \cdot S_{OC} + S_{CM}\right]$

As a result,

$$\Delta t = X1 \cdot t_{diss} + \left[X2 \cdot t_{diss}^{\,2} + X3\right]^{\frac{1}{2}}$$

$$+ X4 \cdot \left[X2 \cdot t_{diss}^{\,2} + X3\right]^{-\frac{1}{2}} - X5 \qquad \text{(AI-32).}$$

The second term on the RHS of Eq. (AI-32) can be written as

$$\left[X2 \cdot t_{diss}^{\,2} + X3\right]^{\frac{1}{2}} = X3^{\frac{1}{2}} \cdot \left[\frac{X2}{X3} \cdot t_{diss}^{\,2} + 1\right]^{\frac{1}{2}} \qquad \text{(AI-33).}$$

The third term on the RHS of Eq. (AI-32) can be written as

$$X4 \cdot \left[X2 \cdot t_{diss}^{\,2} + X3\right]^{-\frac{1}{2}} = X4 \cdot X3^{-\frac{1}{2}} \cdot \left[\frac{X2}{X3} \cdot t_{diss}^{\,2} + 1\right]^{-\frac{1}{2}} \qquad \text{(AI-34).}$$

Since $(1 \pm x)^n = 1 \pm nx + \dfrac{n(n-1)x^2}{2!} \pm \dfrac{n(n-1)(n-2)x^3}{3!} + \cdots$ for $x^2 < 1$

(AI-33),

therefore, for small t_{diss} (how small t_{diss} should be will be calculated later),

$$\left[X2 \cdot t_{diss}^{\,2} + X3\right]^{\frac{1}{2}} \cong X3^{\frac{1}{2}} \cdot \left[1 + \frac{1}{2} \cdot \frac{X2}{X3} \cdot t_{diss}^{\,2}\right]$$

$$= X3^{\frac{1}{2}} + \frac{1}{2} \cdot X2 \cdot X3^{-\frac{1}{2}} \cdot t_{diss}^{\,2} \qquad \text{(AI-34)}$$

$$X4 \cdot \left[X2 \cdot t_{diss}^{\,2} + X3\right]^{-\frac{1}{2}} \cong X4 \cdot X3^{-\frac{1}{2}} \cdot \left[1 - \frac{1}{2} \cdot \frac{X2}{X3} \cdot t_{diss}^{\,2}\right]$$

$$= X4 \cdot X3^{-\frac{1}{2}} - \frac{1}{2} \cdot X2 \cdot X3^{-\frac{3}{2}} \cdot X4 \cdot t_{diss}{}^{2} \qquad \text{(AI-35).}$$

Hence, for small t_{diss}, Δt can be rewritten as follows:

$$\Delta t \cong X1 \cdot t_{diss} + X3^{\frac{1}{2}} + \frac{1}{2} \cdot X2 \cdot X3^{-\frac{1}{2}} \cdot t_{diss}{}^{2}$$

$$+ X4 \cdot X3^{-\frac{1}{2}} - \frac{1}{2} \cdot X2 \cdot X3^{-\frac{3}{2}} \cdot X4 \cdot t_{diss}{}^{2} - X5 \qquad \text{(AI-36).}$$

Substituting the expressions for $X1$, $X2$, $X3$, $X4$ and $X5$ into Δt, we get

$$\Delta t \cong \left[1 - \left(\frac{M_1}{M_2}\right)\right] \cdot t_{diss} + \left(\frac{2 \cdot M_1 \cdot S_{OC}{}^{2}}{q \cdot V_{OC}}\right)^{\frac{1}{2}}$$

$$+ \frac{1}{2} \cdot \left(\frac{M_1{}^{2} - M_1 \cdot M_2}{M_2{}^{2}}\right) \cdot \left(\frac{2 \cdot M_1 \cdot S_{OC}{}^{2}}{q \cdot V_{OC}}\right)^{-\frac{1}{2}} \cdot t_{diss}{}^{2}$$

$$+ \left(\frac{M_1 \cdot S_{OC} \cdot S_{CM}}{q \cdot V_{OC}}\right) \cdot \left(\frac{2 \cdot M_1 \cdot S_{OC}{}^{2}}{q \cdot V_{OC}}\right)^{-\frac{1}{2}}$$

$$- \frac{1}{2} \cdot \left(\frac{M_1{}^{2} - M_1 \cdot M_2}{M_2{}^{2}}\right) \cdot \left(\frac{2 \cdot M_1 \cdot S_{OC}{}^{2}}{q \cdot V_{OC}}\right)^{-\frac{3}{2}} \cdot \left(\frac{M_1 \cdot S_{OC} \cdot S_{CM}}{q \cdot V_{OC}}\right) \cdot t_{diss}{}^{2}$$

$$- \left(\frac{M_1}{2 \cdot q \cdot V_{OC}}\right)^{\frac{1}{2}} \cdot \left[2 \cdot S_{OC} + S_{CM}\right] \qquad \text{(AI-37).}$$

Since $$\left(\frac{2\cdot M_1\cdot {S_{OC}}^2}{q\cdot V_{OC}}\right)^{\frac{1}{2}} = \left(\frac{M_1}{2\cdot q\cdot V_{OC}}\right)^{\frac{1}{2}}\cdot 2\cdot S_{OC} \qquad \text{(AI-38)}$$

and $$\left(\frac{M_1\cdot S_{OC}\cdot S_{CM}}{q\cdot V_{OC}}\right)\cdot\left(\frac{2\cdot M_1\cdot {S_{OC}}^2}{q\cdot V_{OC}}\right)^{-\frac{1}{2}} = \left(\frac{{M_1}^2\cdot {S_{OC}}^2\cdot {S_{CM}}^2}{q^2\cdot {V_{OC}}^2}\cdot\frac{q\cdot V_{OC}}{2\cdot M_1\cdot {S_{OC}}^2}\right)^{\frac{1}{2}}$$

$$= \left(\frac{M_1}{2\cdot q\cdot V_{OC}}\right)^{\frac{1}{2}}\cdot S_{CM} \qquad \text{(AI-39),}$$

therefore, the sum of all the terms in Eq. (AI-37) which are independent of t_{diss} can be written as

$$\left(\frac{M_1}{2\cdot q\cdot V_{OC}}\right)^{\frac{1}{2}}\cdot 2\cdot S_{OC} + \left(\frac{M_1}{2\cdot q\cdot V_{OC}}\right)^{\frac{1}{2}}\cdot S_{CM} - \left(\frac{M_1}{2\cdot q\cdot V_{OC}}\right)^{\frac{1}{2}}\cdot\left[2\cdot S_{OC} + S_{CM}\right] = 0.$$

The sum of all the terms in Eq. (AI-37) which are dependent of ${t_{diss}}^2$ can be written as

$$\frac{1}{2}\cdot\left(\frac{{M_1}^2 - M_1\cdot M_2}{{M_2}^2}\right)\cdot\left(\frac{q\cdot V_{OC}}{2\cdot M_1\cdot {S_{OC}}^2}\right)^{\frac{1}{2}}\cdot {t_{diss}}^2$$

$$-\frac{1}{2}\cdot\left(\frac{{M_1}^2 - M_1\cdot M_2}{{M_2}^2}\right)\cdot\left(\frac{q\cdot V_{OC}}{2\cdot M_1\cdot {S_{OC}}^2}\right)^{\frac{3}{2}}\cdot\left(\frac{M_1\cdot S_{OC}\cdot S_{CM}}{q\cdot V_{OC}}\right)\cdot {t_{diss}}^2$$

$$= \frac{1}{2}\cdot\left(\frac{{M_1}^2 - M_1\cdot M_2}{{M_2}^2}\right)\cdot\left(\frac{q\cdot V_{OC}}{2\cdot M_1\cdot {S_{OC}}^2}\right)^{\frac{1}{2}}\cdot$$

$$\left[1 - \left(\frac{q\cdot V_{OC}}{2\cdot M_1\cdot {S_{OC}}^2}\right)\cdot\left(\frac{M_1\cdot S_{OC}\cdot S_{CM}}{q\cdot V_{OC}}\right)\right]\cdot {t_{diss}}^2$$

$$= \frac{1}{2}\cdot\left(\frac{M_1^{\,2} - M_1\cdot M_2}{M_2^{\,2}}\right)\cdot\left(\frac{q\cdot V_{OC}}{2\cdot M_1\cdot S_{OC}^{\,2}}\right)^{\frac{1}{2}}\cdot\left[1-\left(\frac{S_{CM}}{2\cdot S_{OC}}\right)\right]\cdot t_{diss}^{\,2}\ .$$

Hence, for small t_{diss},

$$\Delta t \cong \left[1-\left(\frac{M_1}{M_2}\right)\right]\cdot t_{diss}$$

$$+\frac{1}{2}\cdot\left(\frac{M_1^{\,2} - M_1\cdot M_2}{M_2^{\,2}}\right)\cdot\left(\frac{q\cdot V_{OC}}{2\cdot M_1\cdot S_{OC}^{\,2}}\right)^{\frac{1}{2}}\cdot\left[1-\left(\frac{1}{2}\cdot\frac{S_{CM}}{S_{OC}}\right)\right]\cdot t_{diss}^{\,2} \qquad \text{(AI-40)}.$$

The values for all the parameters and constants shown on the RHS of the above equation are as follows:

V_{OC} = 1570 V ; S_{OC} = 0.0188 m ; S_{CM} = 0.9613 m ; $q = 1.602\times10^{-19}$ C .

For the detection of the intact and the nascent tS-H_1 clusters,

M_1 = mass of tS-H_1 = 4.426×10^{-25} kg ;

M_2 = mass of tS-H_2 = 5.858×10^{-25} kg .

When all the above values were plugged into Eq. (AI-40), we get

$$\Delta t \cong \left[1-\left(\frac{M_1}{M_2}\right)\right]\cdot t_{diss} + (0.0020\ ns^{-1})\cdot t_{diss}^{\,2} \qquad \text{(AI-41)}.$$

(f) Evaluating t_{diss} where Eqs. (AI-34)-(AI-37), and Eqs. (AI-40)-(AI-41) are Valid

For Eqs. (AI-34)-(AI-37) and Eqs. (AI-40)-(AI-41) to be valid,

$$\left[\frac{X2}{X3}\cdot t_{diss}{}^{2}\right]^{2} < 1$$

$$\Rightarrow \quad \left|\frac{X2}{X3}\cdot t_{diss}{}^{2}\right| < 1$$

$$\Rightarrow \quad t_{diss}{}^{2} < \left|\frac{X3}{X2}\right| = \left|\left(\frac{2\cdot M_1\cdot S_{OC}{}^{2}}{q\cdot V_{OC}}\right)\cdot\left(\frac{M_2{}^{2}}{M_1{}^{2} - M_1\cdot M_2}\right)\right|$$

$$= 6.735\times 10^{-12}$$

$$\therefore \quad t_{diss} < 2.595\times 10^{-6}\ \text{s}\,.$$

Appendix II

In this appendix, Eq. (4.6) and (4.8) are derived.

Derivation of Eq. (4.6). From Eq. (4.5),

$$\begin{aligned} I_2(t) &= [\mathrm{A}-\mathrm{B}_n^{+}(E_{ex,ion}^n-\Delta E_{ex}^n)]_{t'=0}\cdot[1-\beta(E_{ex,ion}^n-\Delta E_{ex}^n)] \\ &= \sigma'_{probe}\cdot[\mathrm{A}-\mathrm{B}_n^{*}(E_{ex}^n-\Delta E_{ex}^n)]\cdot[1-\beta(E_{ex,ion}^n-\Delta E_{ex}^n)] \ . \end{aligned}$$

$[\mathrm{A}-\mathrm{B}_n^{*}(E_{ex}^n-\Delta E_{ex}^n)]$ can be derived as follows:

$$\begin{aligned} \frac{d[\mathrm{A}-\mathrm{B}_n^{*}(E_{ex}^n-\Delta E_{ex}^n)]}{dt} &= k_{vp}^{n+1}(E_{ex}^{n+1})[\mathrm{A}-\mathrm{B}_{n+1}^{*}(E_{ex}^{n+1})] \\ &\quad -[k_r^n+k_{iso}^n(E_{ex}^n-\Delta E_{ex}^n)+k_{vp}^n(E_{ex}^n-\Delta E_{ex}^n)]\cdot[\mathrm{A}-\mathrm{B}_n^{*}(E_{ex}^n-\Delta E_{ex}^n)] \end{aligned}$$

and the expression for $[\mathrm{A}-\mathrm{B}_{n+1}^{*}(E_{ex}^{n+1})]$ can be obtained by solving the equation below:

$$\begin{aligned} \frac{d[\mathrm{A}-\mathrm{B}_{n+1}^{*}(E_{ex}^{n+1})]}{dt} &= -[k_r^{n+1}+k_{iso}^{n+1}(E_{ex}^{n+1})+k_{vp}^{n+1}(E_{ex}^{n+1})]\cdot[\mathrm{A}-\mathrm{B}_{n+1}^{*}(E_{ex}^{n+1})] \\ &= -k_{Total}^{n+1}(E_{ex}^{n+1})\cdot[\mathrm{A}-\mathrm{B}_{n+1}^{*}(E_{ex}^{n+1})] \\ [\mathrm{A}-\mathrm{B}_{n+1}^{*}(E_{ex}^{n+1})] &= [\mathrm{A}-\mathrm{B}_{n+1}^{*}(E_{ex}^{n+1})]_0\cdot\exp[-k_{Total}^{n+1}(E_{ex}^{n+1})t] \ . \end{aligned}$$

Therefore,

$$\begin{aligned} \frac{d[\mathrm{A}-\mathrm{B}_n^{*}(E_{ex}^n-\Delta E_{ex}^n)]}{dt} &= k_{vp}^{n+1}(E_{ex}^{n+1})[\mathrm{A}-\mathrm{B}_{n+1}^{*}(E_{ex}^{n+1})]_0\cdot\exp[-k_{Total}^{n+1}(E_{ex}^{n+1})t] \\ &\quad -k_{Total}^n(E_{ex}^n-\Delta E_{ex}^n)\cdot[\mathrm{A}-\mathrm{B}_n^{*}(E_{ex}^n-\Delta E_{ex}^n)] \end{aligned}$$

and

$$\begin{aligned} [\mathrm{A}-\mathrm{B}_n^{*}(E_{ex}^n-\Delta E_{ex}^n)] &= \frac{k_{vp}^{n+1}(E_{ex}^{n+1})[\mathrm{A}-\mathrm{B}_{n+1}^{*}(E_{ex}^{n+1})]_0}{k_{Total}^n(E_{ex}^n-\Delta E_{ex}^n)-k_{Total}^{n+1}(E_{ex}^{n+1})} \\ &\quad \cdot\{\exp[-k_{Total}^{n+1}(E_{ex}^{n+1})]t-\exp[-k_{Total}^n(E_{ex}^n-\Delta E_{ex}^n)\,t]\} . \end{aligned}$$

Finally,

$$I_2(t) = \sigma'_{probe} \cdot \left\{ \frac{k_{vp}^{n+1}(E_{ex}^{n+1})[\mathrm{A}-\mathrm{B}_{n+1}{}^{*}(E_{ex}^{n+1})]_0}{k_{Total}^{n}(E_{ex}^{n}-\Delta E_{ex}^{n}) - k_{Total}^{n+1}(E_{ex}^{n+1})} \right.$$
$$\left. \cdot \{\exp[-k_{Total}^{n+1}(E_{ex}^{n+1})]t - \exp[-k_{Total}^{n}(E_{ex}^{n}-\Delta E_{ex}^{n})\, t]\} \right\}$$
$$\cdot [1-\beta(E_{ex,ion}^{n}-\Delta E_{ex}^{n})] \ .$$

Derivation of Eq. (4.8). For $I_3(t)$, one only need substitute in Eq. (4.7) the time dependence of $[\mathrm{A}-\mathrm{B}_{n+1}{}^{*}(E_{ex}^{n+1})]$ as derived above:

$$[\mathrm{A}-\mathrm{B}_{n+1}{}^{*}(E_{ex}^{n+1})] = [\mathrm{A}-\mathrm{B}_{n+1}{}^{*}(E_{ex}^{n+1})]_0 \cdot \exp[-k_{Total}^{n+1}(E_{ex}^{n+1})\, t] \ .$$

Appendix III

As mentioned in Section 3, some of the transients presented in Fig. 3 to Fig. 6 of that section may appear to have better signal-to-noise ratio than they actually do because they may have been "physically smoothed." In appendix III, the procedure used for physically smoothing transients in this work is described. The term "physically" is applied because the smoothing method used here is different from the smoothing methods commonly adopted in science, such as point-average smoothing.

When a decision was made that the data collected from a given experiment needs to be smoothed, the following steps were performed. At the end of the experiment, the final transient file would be recorded. This transient file would then be reopened, and be fitted with a program to obtain the lifetime. After the lifetime had been calculated, outlaying data points on the transient, such as spikes or other points which seemed like irregular noise, would then be moved closer to their neighboring points so that the transient would appear smoother and have better signal-to-noise level. After the transient file had been physically smoothed as such, the smoothed file would be saved, and the original transient file used would be written over by the smoothed file as a result. For a given experiment, if only one copy of original transient file existed prior to smoothing, then the original transient would be lost after smoothing, and the original data from this experiment would be irrecoverable. However, in an experiment whereby more than one copy of transient files were saved (at various stages of the experiment), original data would not be lost as a result of smoothing. This is because even though the transient recorded at the end of the experiment was modified after smoothing, transient files recorded at earlier stages of the experiment, which were original and unmodified, could

be used in place of the smoothed transient for analysis, if one desires. Hence, if smoothing was performed on experimental data whereby more than one copy of original transient files had been saved, these data are considered recoverable.

Although the smoothing procedure used in this work was a departure from the common data-smoothing practices of the scientific community, the lifetime extracted from the transient, which was the primary objective of the experiment, was not affected. This is because, as mentioned earlier, lifetimes were extracted from the transients prior to the data point adjustments. However, to allow readers to judge objectively whether the decay time of a transient was affected in any way by physical smoothing, the transients for five sets of recoverable data are presented in Fig. 1 to Fig. 5. In each figure, the lifetime extracted from a smoothed transient is compared with that obtained from an original and unmodified transient recorded at an earlier stage of the same experiment. As can be seen, the lifetimes for both the transients for each of the recoverable data are the same.

AIII.1. Figure Captions

Figure 1. Comparison between an original and a "physically smoothed" transient for a given tS (control) experiment. The original transient was recorded after 53 scans, and no adjustment was made to the transient. The smoothed transient was created by adjusting several outlaying points in the final transient (recorded after 62 scans) to make the transient look smoother.

Figure 2. Comparison between an original and a "physically smoothed" transient for a given tS-H_1 experiment. The original transient was recorded after 109 scans, and no adjustment was made to the transient. The smoothed transient was created by adjusting several outlaying points in the final transient (recorded after 117 scans) to make the transient look smoother.

Figure 3. Comparison between an original and a "physically smoothed" transient for a given tS-H_1 experiment. The original transient was recorded after 70 scans, and no adjustment was made to the transient. The smoothed transient was created by adjusting several outlaying points in the final transient (recorded after 90 scans) to make the transient look smoother.

Figure 4. Comparison between an original and a "physically smoothed" transient for a given tS-H_1 experiment. The original transient was recorded after 58 scans, and no adjustment was made to the transient. The smoothed transient was created by adjusting several outlaying points in the final transient (recorded after 98 scans) to make the transient look smoother.

Figure 5. Comparison between an original and a "physically smoothed" transient for a given tS-H_2 experiment. The original transient was recorded after 120 scans, and no adjustment was made to the transient. The smoothed transient was created by adjusting several outlaying points in the final transient (recorded after 177 scans) to make the transient look smoother.

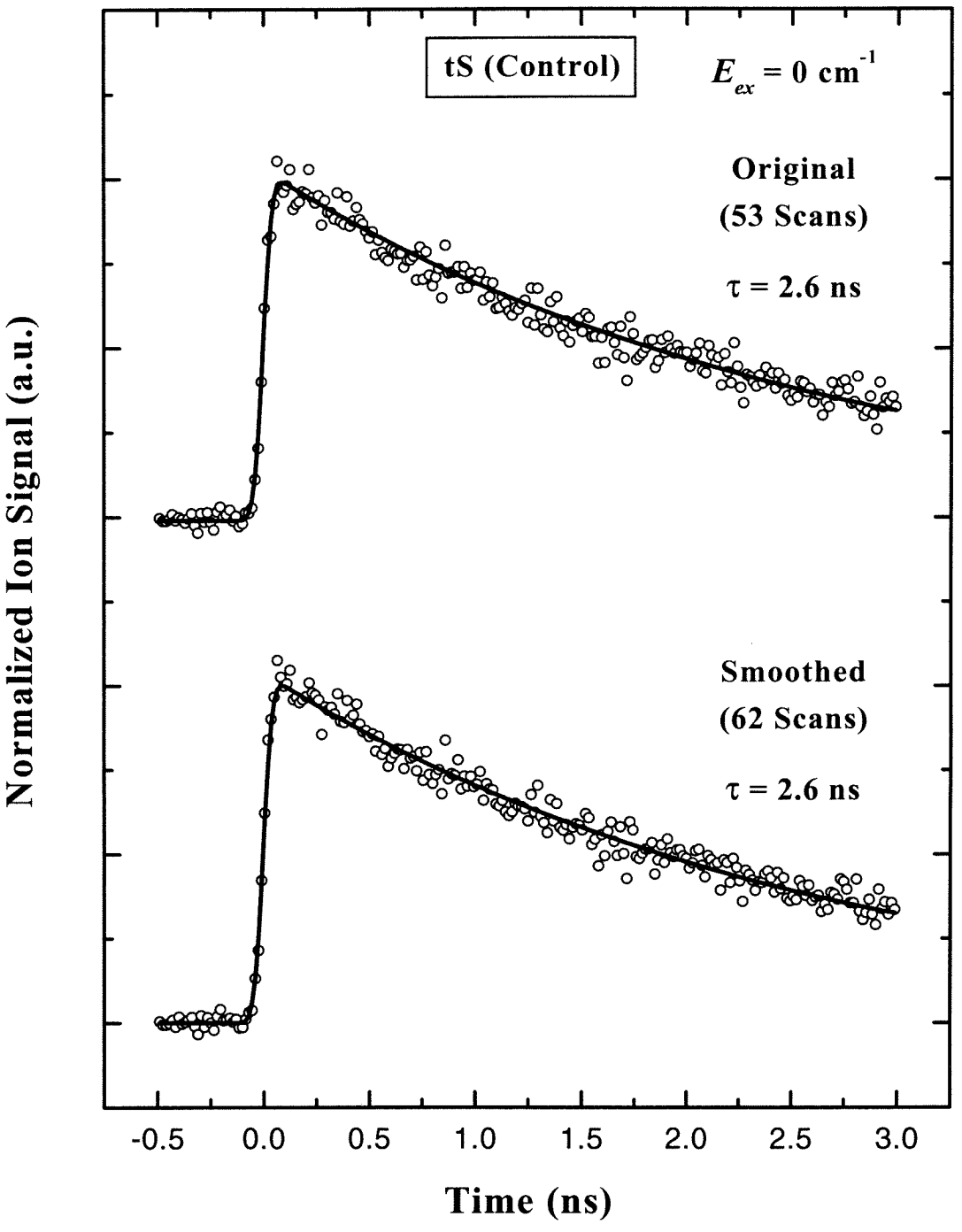
tS (Control)
E_{ex} = 0 cm^{-1}
Original
(53 Scans)
τ = 2.6 ns
Smoothed
(62 Scans)
τ = 2.6 ns
Normalized Ion Signal (a.u.)
-0.5
0.0
0.5
1.0
1.5
2.0
2.5
3.0
Time (ns)

Figure 1

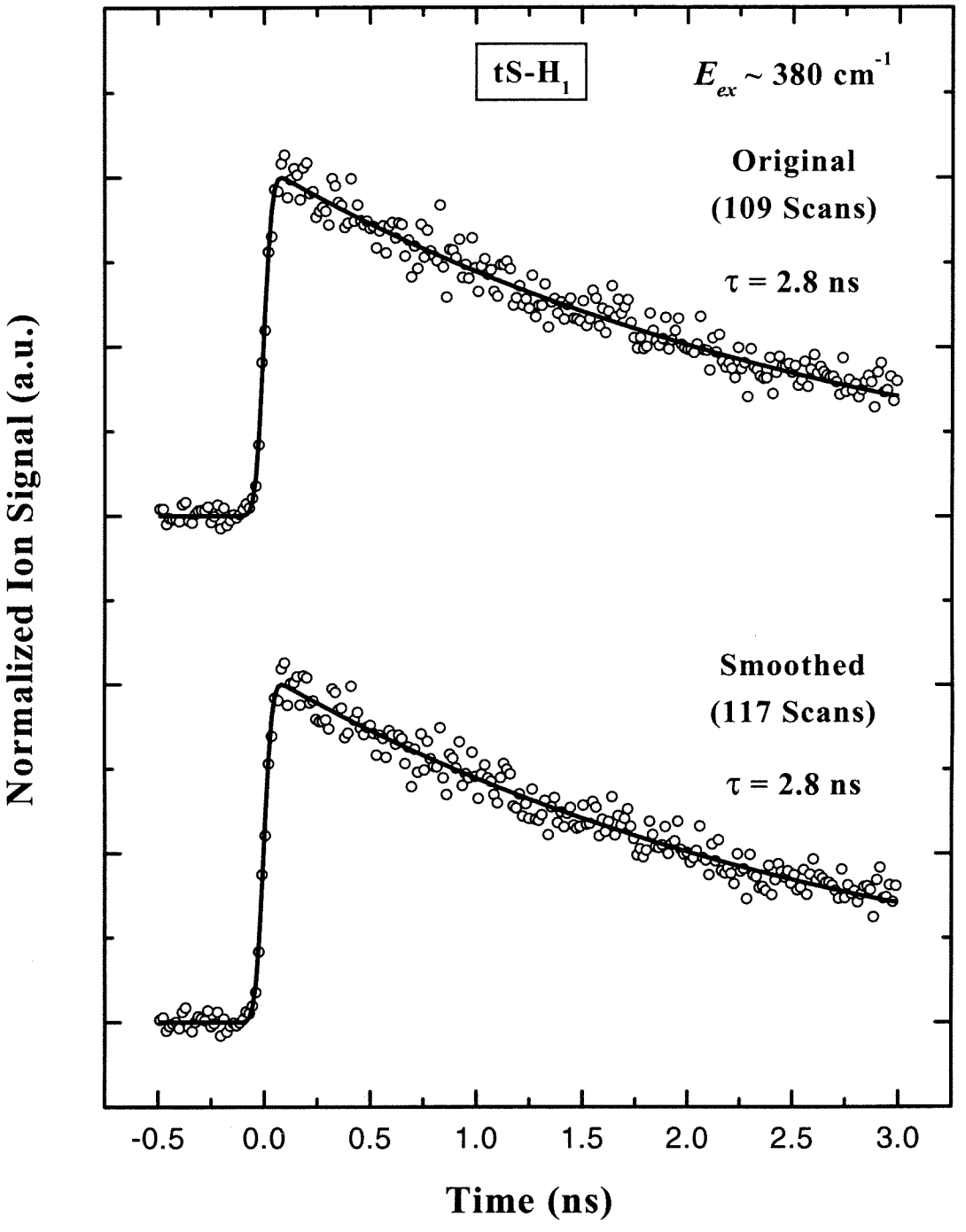
tS-H1
Eex ~ 380 cm-1
Original
(109 Scans)
τ = 2.8 ns
Smoothed
(117 Scans)
τ = 2.8 ns
Normalized Ion Signal (a.u.)
-0.5
0.0
0.5
1.0
1.5
2.0
2.5
3.0
Time (ns)

Figure 2

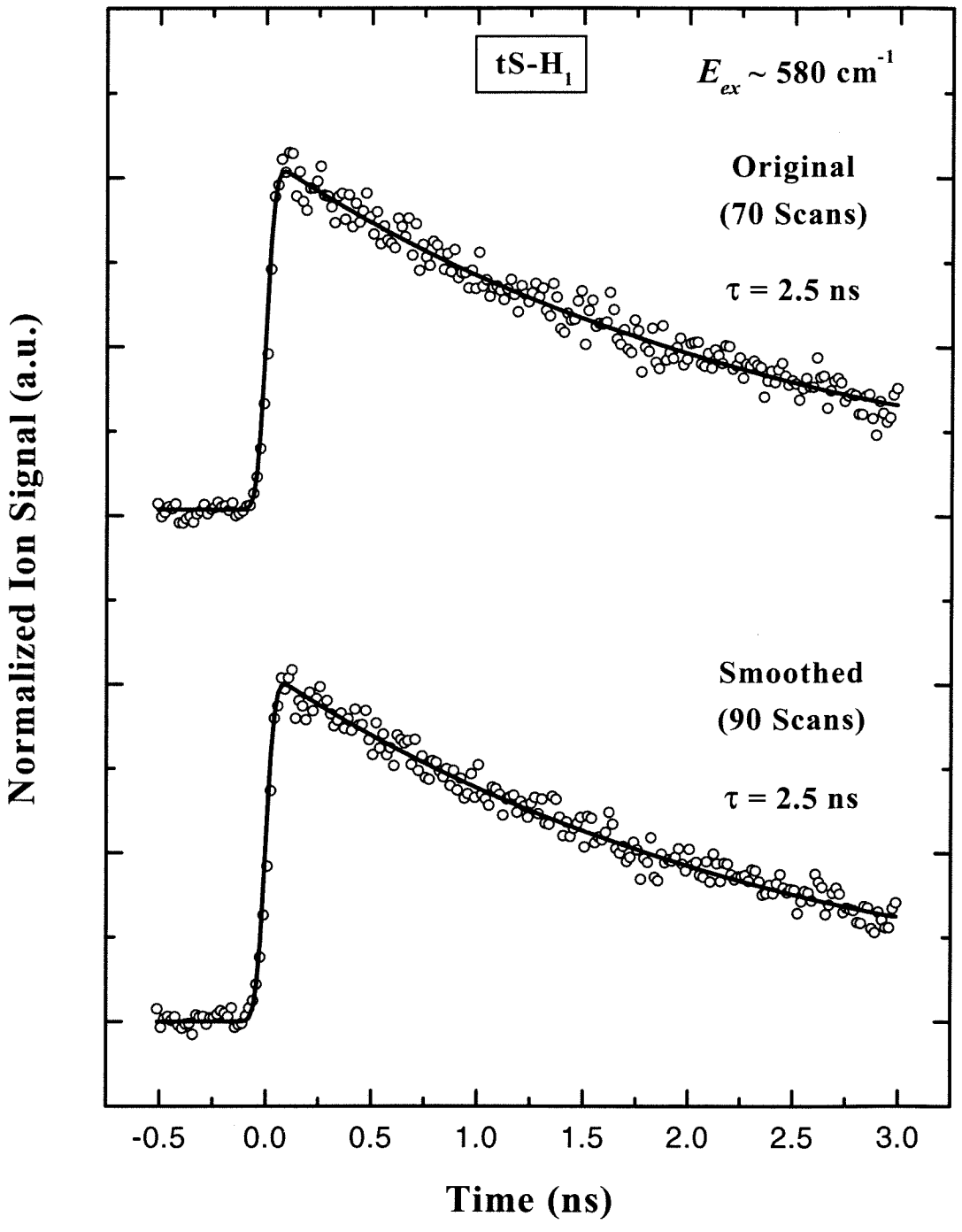
tS-H1
Eex ~ 580 cm-1
Original
(70 Scans)
τ = 2.5 ns
Smoothed
(90 Scans)
τ = 2.5 ns
Normalized Ion Signal (a.u.)
-0.5
0.0
0.5
1.0
1.5
2.0
2.5
3.0
Time (ns)

Figure 3

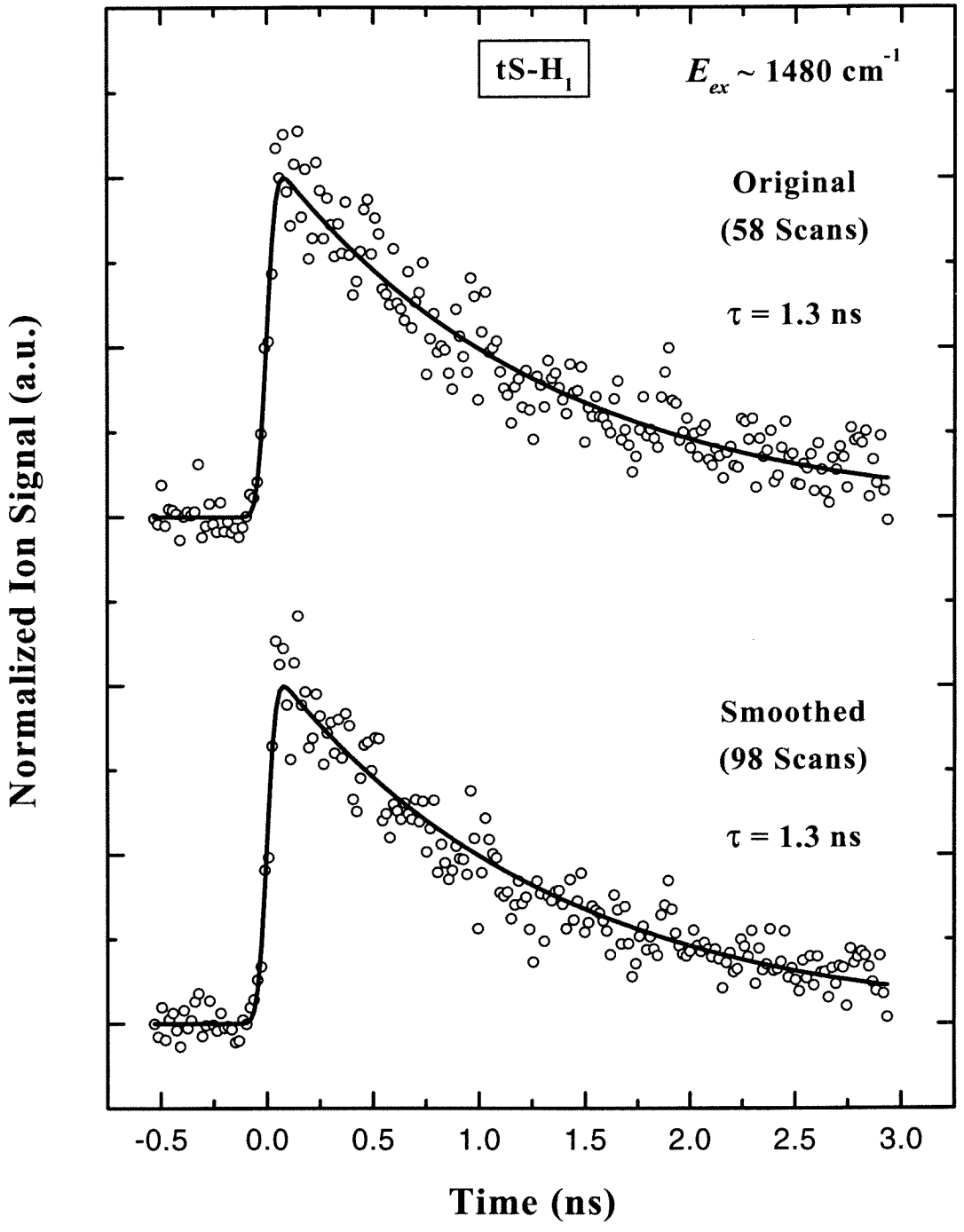
tS-H1
E_{ex} ~ 1480 cm^{-1}
Original
(58 Scans)
τ = 1.3 ns
Smoothed
(98 Scans)
τ = 1.3 ns
Normalized Ion Signal (a.u.)
-0.5
0.0
0.5
1.0
1.5
2.0
2.5
3.0
Time (ns)

Figure 4

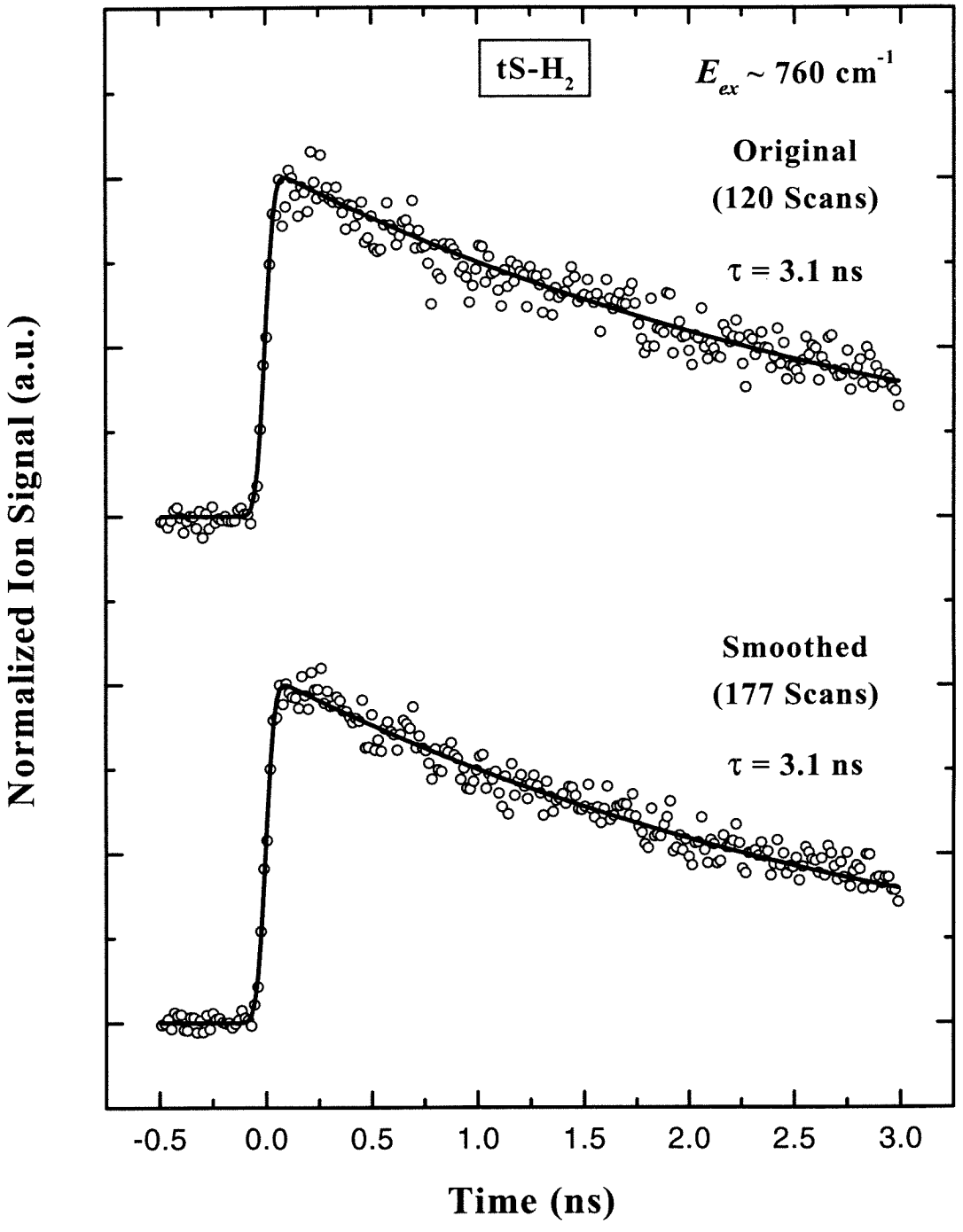
tS-H2
Eex ~ 760 cm-1
Original
(120 Scans)
τ = 3.1 ns
Smoothed
(177 Scans)
τ = 3.1 ns
Normalized Ion Signal (a.u.)
-0.5
0.0
0.5
1.0
1.5
2.0
2.5
3.0
Time (ns)

Figure 5